OBSERVATIONS AND MODELING OF MIXING PROCESSES IN A FRESH WATER RESERVOIR - VALLE DE BRAVO (MEXICO)

A Thesis

by

GAURAV SINGHAL

Submitted to the Office of Graduate Studies of
Texas A&M University
in partial fulfillment of the requirements for the degree of

MASTER OF SCIENCE

December 2005

Major Subject: Oceanography

OBSERVATIONS AND MODELING OF MIXING PROCESSES IN A FRESH WATER RESERVOIR - VALLE DE BRAVO (MEXICO)

A Thesis

by

GAURAV SINGHAL

Submitted to the Office of Graduate Studies of
Texas A&M University
in partial fulfillment of the requirements for the degree of

MASTER OF SCIENCE

Approved by:

Chair of Committee,	Ayal Anis
Committee Members,	Achim Stoessel
	Ping Chang
	Vijay Panchang
Head of Department,	Wilford Gardner

December 2005

Major Subject: Oceanography

ABSTRACT

Observations and Modeling of Mixing Processes in a
Fresh Water Reservoir - Valle de Bravo (Mexico). (December 2005)
Gaurav Singhal, B.S., Indian Institute of Technology
Chair of Advisory Committee: Dr. Ayal Anis

Current understanding of small-scale physical processes, such as mixing, in tropical water bodies is lacking and observations are scarce at best. This study sheds more light on these processes through a combined observational-modeling approach. For this purpose, observations were made in Valle de Bravo's freshwater reservoir, about 100 km west of Mexico City and at an elevation of 1830 m above sea surface. Turbulence kinetic energy dissipation (TKED) rates were estimated by fitting a theoretical Batchelor spectrum to the temperature gradient spectrum. From similarity scaling of dissipation rates, it was found that in the surface layer, winds were the main driving force in generating turbulence during the day, while convective forces were responsible during the night. Bottom boundary layer (BBL) mixing was mainly driven by internal wave (first vertical and first horizontal mode) breaking at the bottom. Lognormality of turbulence dissipation rates is also discussed for surface, intermediate and bottom boundary layers. For our modeling efforts, a state-of-the-art one-dimensional turbulence model was used and forced with the observed surface meteorology to obtain simulated temperature and dissipation rate profiles. The model results were found to be in good agreement with the observations, though minor differences in dissipation rates were found in the vicinity of the thermocline and the BBL.

ACKNOWLEDGMENTS

First of all, I would like to thank my advisor, Dr. Ayal Anis, for invaluable guidance and support throughout this research. It has been a roller-coaster ride since I joined him in the summer of 2003. I must say, I was a novice then, but the stage I am right now makes me feel proud of myself. I was mentored by one of the greatest professors I have worked with during the last 6 years. My special thanks go to his wife, Ruthy, who is so full of life. She is the most entertaining person I have ever talked with, and I must say, she is a great cook. Almost every afternoon over the last couple of years, I could find a plate loaded with delicacy (cakes, pastries, cookies) in our laboratory.

I am lucky to have been blessed with wonderful friends all my life. It was only when I moved to Galveston (after spending a year in College Station) that I made new friends. Since then, they have supported me all along the way including the time when I was writing my thesis. To name some of them - Keith (my colleague, roommate, officemate and a very good friend), Jamie (she is an awesome girl, who has been there for me all the times), Sally, Clif, Federico (we always have bets for some or the other things, in last two bets I won and he cooked me Lasagna), Allison and others. I thank you all for being here for me.

I would like to thank CONACYT (Mexican equivalent of NSF) and Office of the Vice President for Research at Texas A&M University for sponsoring this project. I would also like to thank Dr. Martin Merino and his research team for collaborating with us on this project. They mainly focussed on biogeochemical aspects while we were looking at physical processes.

I would like to thank my committee members - Dr. Vijay Panchang, Dr. Achim Stoessel and Dr. Ping Chang for helpful suggestions in this thesis.

Last but not the least, I would like to thank my parents who helped me at every point in my life mentally, physically as well as financially. I would not have made it to this point without their support.

TABLE OF CONTENTS

CHAPTER Page

LIST OF TABLES

TABLE Page

LIST OF FIGURES

FIGURE Page

FIGURE Page

FIGURE Page

FIGURE Page

CHAPTER I

INTRODUCTION

The interactions between the atmosphere and the ocean have received wide attention by various researchers and it is well known that they are closely inter-related. For example, the physical processes occurring in the upper layers of the ocean have an effect on the weather, climate and gas exchange. In turn, the daily cycle of heating and cooling, wind, rain and other large scale weather features can directly affect the physical processes in the upper layers of the water column [1]. Some of these processes are well explained but physical processes related to turbulence are still not well understood.

Turbulent flows have been investigated for more than a century but no general solution of problems in turbulence exists. Leonardo da Vinci first used the term "turbulence" in reference to fluid flows and studied the phenomenon extensively and since then understanding turbulent flows has been a source of fascination. From the very beginning, turbulence research focussed mainly on two aspects - 1) calculation of practical effects of turbulence, primarily the momentum, heat and mass transfer, associated with the design of devices and their interaction with the environment; and 2) understanding the physics of turbulence phenomena. The initial work of Boussinesq and Reynolds focussed on those two aspects.

It is difficult to give a precise definition of turbulence, however most researchers commonly describe the characteristics of turbulence to include the following :

- **Three Dimensionality** - Turbulent flows are three dimensional. Two dimensional turbulence does exist but is a very different phenomenon, as compared

---

The journal model is *IEEE Transactions on Automatic Control*.

to three dimensional, relevant to the large scales of geophysical flows, but even in those flows, the smallest scales are three-dimensional.

- **Irregular and unpredictable** - Turbulent flows are random, irregular, unsteady and highly unpredictabale. They are characterized by a wide range of time scales on which fluctuations occur.

- **Broad Spectrum** - We already noted that turbulent flows fluctuate on a wide range of time scales, but they also fluctuate on a broad range of length scales (millimeters to centimeters), where the range of scales increases with the Reynolds number (R_e), defined as $R_e = UL/\nu$ where U is the velocity scale, L is the length scale and ν is the kinematic viscosity.

Turbulence results from the non-linear nature of advection, which enables interaction between motions on different spatial scales. Fully turbulent flows consist of a wide range of scales, which are mainly classified as either large or small scales. The large scales are on the order of the flow width; contain most of the energy; and dominate the transport of momentum, mass, and heat. The small scales include the dissipative range responsible for most of the energy dissipation and the inertial range; inertial range scales are large compared to dissipative scales but small compared to large scales.

Kolmogorov [2] fundamentally changed the state of turbulent investigations with his hypotheses which state that the statistical properties of the dissipation scales are determined universally by (a) kinematic viscosity (ν) (m^2/s) and the average energy dissipation rate $< \epsilon >$ (m^2/s^3) and (b) those in the inertial range, if the Reynolds number is high enough for one to exist, are determined by $< \epsilon >$ only. However, Kolmogorov's predictions were contradicted by measurements of small-scale turbulent velocity fluctuations done in the laboratory [3]. Obukhov [4] explained the

contradictions by the influence of the spatial variation of the rate of energy dissipation $\epsilon(x,t)$. He produced a crude quantitative estimate of this influence while Kolmogorov [2], expanding on Obukhov's argument, came out with a third hypotheses taking dissipation fluctuations into account, which was consistent with experimental data for the velocity field.

A large amount of work by Boussinesq, Taylor, Prandtl and von K*árm*á*n* is based on a semi-empirical approach involving calculation of gradient transport and eddy viscosities. Prandtl and von K*árm*á*n* formulated similarity laws for the viscous region and the outer layers of developed wall-bounded flows. They derived a logarithmic law for the fluid velocity profile, *U(y)* (where y is the coordinate normal to the wall), based on semiempirical arguments, which is given as

$$U(y) = u^*[ln(yu^*/\nu)/\kappa + B], \tag{1.1}$$

where u^* is the friction velocity, ν the kinematic viscosity, κ is the von K*árm*á*n* constant and B is a universal constant. The limits of the range of y values is $50(\nu/u^*) < y < 0.15L$, where L is the boundary layer thickness. A similarity approach of the same type was also applied to the parameterization of the atmospheric surface mixed layer above land in terms of the Obukhov length [5]. The semi-empirical approach led to what we now refer to as turbulence parameterization which will be discussed in detail later in this chapter. However, we will first describe observational approaches in measuring turbulence in aquatic environments.

The measurement of turbulence in the ocean has been one of the most difficult technical challenges for oceanographers. The non-linear and random nature of turbulence makes it difficult to distinguish it from instrument noise and in a stratified ocean (or lake) it also needs to be distinguished from the often-coherent internal

waves, which do not contribute directly to mixing, whereas turbulence does. In order to observe the full spectrum of turbulent flows below the surface, it is generally necessary to establish a spatial reference for velocity measurements. Near the seabed, this can be achieved by attaching instruments to tripods extending upward from the bed. But in the interior, finding a fixed reference poses a problem.

The early measurements of turbulence were carried out with towed instruments using hot-film anemometers, cold-film anemometers and other sensors (e.g. [6], [7]). But by early 1970s, an approach based on measuring high-frequency velocity and temperature fluctuations by sensors attached to a free-falling body of sufficient inertia was pursued (e.g. [8]), [9]). This led to the development of fast-response sensors and was culminated in a number of practical profilers which had become available by the late 1980s.

These profilers, with microscale velocity shear and temperature sensors of sufficient temporal and spatial resolution to allow estimation of turbulence kinetic energy dissipation (TKED) rates (TKED is the rate at which TKE is dissipated into heat through viscous friction) and overturning scales, have contributed to our knowledge of turbulence and mixing in the interior of the ocean. These probes have also been attached to towed bodies ([6], [7]), submarines ([7], [10]) and autonomous underwater vehicles in order to measure horizontal profiles of the rate of TKED [11].

An alternative approach to measure turbulence in the water column has been made possible in recent years by developments in acoustic Doppler technology. This approach, though, does not resolve dissipation scales but is able to determine momentum transfer in a range of scales responsible for the turbulent shear stresses, which can be combined with the velocity shear to estimate the rate of turbulence energy production, e.g., [12].

With the aid of physical and numerical modelling, prediction and understanding

of complex processes such as turbulence has advanced even further. The first attempt towards mixed-layer modelling was made by Kraus [13] and since then a large number of turbulence schemes have been developed and used in numerical models. Orszag and Patterson [14] were pioneers in large-scale computing of turbulent flows using direct numerical simulation (DNS). They made significant contributions to the techniques necessary for this approach, progressively increasing accuracy and reducing computing time. DNS is a method in which all scales of motion of a turbulent flow are computed. For any reasonable Reynolds number ($R_e > 2000$), this requires a large number of grid points and is therefore very costly. However, DNS has still proven to be an important tool in investigating the physics of turbulence by taking into account all of the flow variables at a large number of spatial locations and many instances of time. An alternate method, large eddy simulations (LES), in which only the large scales are resolved and the smaller scales are parameterized, was developed by Smagorinsky [15], and used for turbulent flows [16]. Since only the large scales are resolved, the computational time for LES is much less than a DNS of the same flow.

However, both DNS and LES are still expensive and another approach based on turbulence closure models was developed in the late 1970s. These models have proven efficient and reliable for describing many oceanic flows. Even though a large variety of such models exist, only two are extensively used in the ocean modelling community. First, the "classic" model of Mellor and Yamada (hereafter, MY)[17], which solves equations for the turbulent kinetic energy (TKE), k, and the product of k and the turbulence length scale, l. Second, the so-called k-ϵ model in the form presented in [18], which solves equations for k and TKED, ϵ (Eqns. (1.2) and (1.3))

The k equation can be written as:

$$\partial_t k + \partial_z F(k) = P + B - \epsilon. \tag{1.2}$$

And the ϵ equation can be written as:

$$\partial_t \epsilon + \partial_z F(\epsilon) = \frac{\epsilon}{k}(c_{\epsilon 1} P + c_{\epsilon 3} B - c_{\epsilon 2}\epsilon). \tag{1.3}$$

with

$$k = (1/2)\overline{(u'^2 + v'^2 + w'^2)}, \quad \epsilon = -\nu \overline{\frac{\partial u_i'}{\partial x_j}\left(\frac{\partial u_i'}{\partial x_j} + \frac{\partial u_j'}{\partial x_i}\right)} \tag{1.4}$$

where u', v' and w' are the velocity perturbations along x,y and z directions respectively, $c_{\epsilon 1} = 1.44$, $c_{\epsilon 2} = 1.92$ and $c_{\epsilon 3}$ depend on steady state Richardson Number [19], P is the TKE production, B is buoyancy, ϵ is the TKED, and *F(k)* and *F(ϵ)* are diffusive fluxes. More detailed description of the equations involved in the k-ϵ model are provided in chapter IV.

Both MY and k-ϵ have been extensively compared and investigated for various oceanic situations (e.g. [20]; [21]; [22]; [23]). These authors demonstrated that both the models are isomorphic in homogenous turbulence and comparable in wall-bounded shear flows. However, differences were noticed between the models when the turbulent transport terms, modelled according to simple down-gradient formulas in both cases, were not negligible.

In [23], various turbulence closure schemes ranging from simple one-equation models (here k is calculated from a transport equation (Eq. (1.2)), and the macro length scale is treated algebraically) to two-equation models such as k-ϵ (both k and ϵ are calculated from exact transport equations (Eqns. (1.2) and (1.3)) were compared, and it was shown that two-equation models better estimate turbulence than simple one-equation models. In [19], two-equation models were also preferred over simple one-equation models.

In another study in Lake Maggiore, it was shown that two-equation k-ϵ turbulence closure schemes can realistically reproduce convectively driven turbulence [24].

There are several other studies (e.g. [23]; [24]; [25]) explaining the advantage of two-equation k-ϵ closure schemes over other turbulence parameterizations in various oceanic environments. However, all such studies were done in water bodies at higher latitudes with different geometries and no documented study for enclosed tropical fresh water bodies exists till today. This study tries to shed more light on turbulence processes in a complex and enclosed tropical fresh water body using a combined approach of observations and model simulations.

The next section describes the goal of this study and its importance. The objectives are explained briefly and the methods that were used are presented followed by a brief description of the study site.

A. Research Objectives

The significant increase in *eutrophication* (water pollution caused by excessive plant nutrients) in tropical reservoirs during the last few decades accentuates the need for a better understanding of various processes in these water bodies. The *Valle de Bravo* (VB) reservoir is one of such bodies, providing 30% of the fresh water supply to metropolitan area of Mexico City. It also serves as a major source for recreational activities and thus is under heavy ecological stress. Currently, this reservoir is highly polluted and is advancing towards a state of *eutrophication* which may jeopardize its function as a fresh water source. Unfortunately, little is known on the various mixing processes affecting tropical water bodies and their ecology and relevant observations are scarce at best.

1. Objective I

The main goal of this study is to better understand various physical processes affecting tropical water bodies in general. This research addresses the following important questions :

- What is the physical response of the reservoir to external forcing ?
- What is the effect of vertical transport of heat, momentum and mass in the interior of the reservoir ?

For this purpose, a field campaign was carried out in the summer of 2003 in VB. Continuous 24-hour profiling was performed to collect vertical temperature microstructure data using a turbulence profiler (SCAMP - Self Contained Autonomous Micro Profiler, manufactured by Precision Measurement Engineering of Encinitas, California), water-current measurements were obtained using an Acoustic Doppler Current Profiler (ADCP, manufactured by Nortek, Norway) and the surface meteorology was monitored from an on-lake meteorological station.

a. Methods

Estimation of various parameters was carried out using the collected data.

- From SCAMP measurements, TKED was estimated by fitting a theoretical *Batchelor Spectrum* (e.g. [26]; [27]; [28]; [29]) to the raw data. The temperature dissipation rate, χ, was directly calculated from SCAMP measurements [29].
- An attempt to compute salinity for this fresh water reservoir was made using the equation of state for fresh water [30].
- Surface wind stress was computed following [31] using wind speed and direction data from the meteorological station.

- Air-sea heat fluxes (sensible, latent, long and short wave and rain heat fluxes) were estimated following [32] and [33].

2. Objective II

For our modeling approach, we used a state-of-the-art one dimensional ocean turbulence model (GOTM) [34]. The purpose of model experiments was to understand the dynamics of mixing processes under various atmospheric conditions in a better way. In this study, we answered following important questions:

- How well do the model simulations compare to the observations and what are the model limitations ?
- How do TKED and χ relate to wind stress and bouyancy flux ? ϵ and χ were scaled by both wind stress and surface buoyancy flux to understand their possible relationship (e.g. [35]; [36]; [37]) .
- What is the role of the BBL in the overall picture of mixing ?

B. Study Site Description

VB is an enclosed natural tropical fresh water reservoir (Fig. 1) located at $19^o21'30''$N and $100^o11'00''$W about 100 km west of Mexico city and has a water surface level of 1830 m. The average depth of this reservoir is about 20 m and the maximum depth is $\sim$30m at station 8 near the dam (Fig. 1). For the purpose of this study, we established four sampling stations placed at strategic locations in the reservoir as shown in Fig. 1. An on-lake meteorological station was also established to continously monitor the surface meteorological paramters such as air temperature and humidity, solar radiation, air pressure, wind speed and direction, and rainfall.

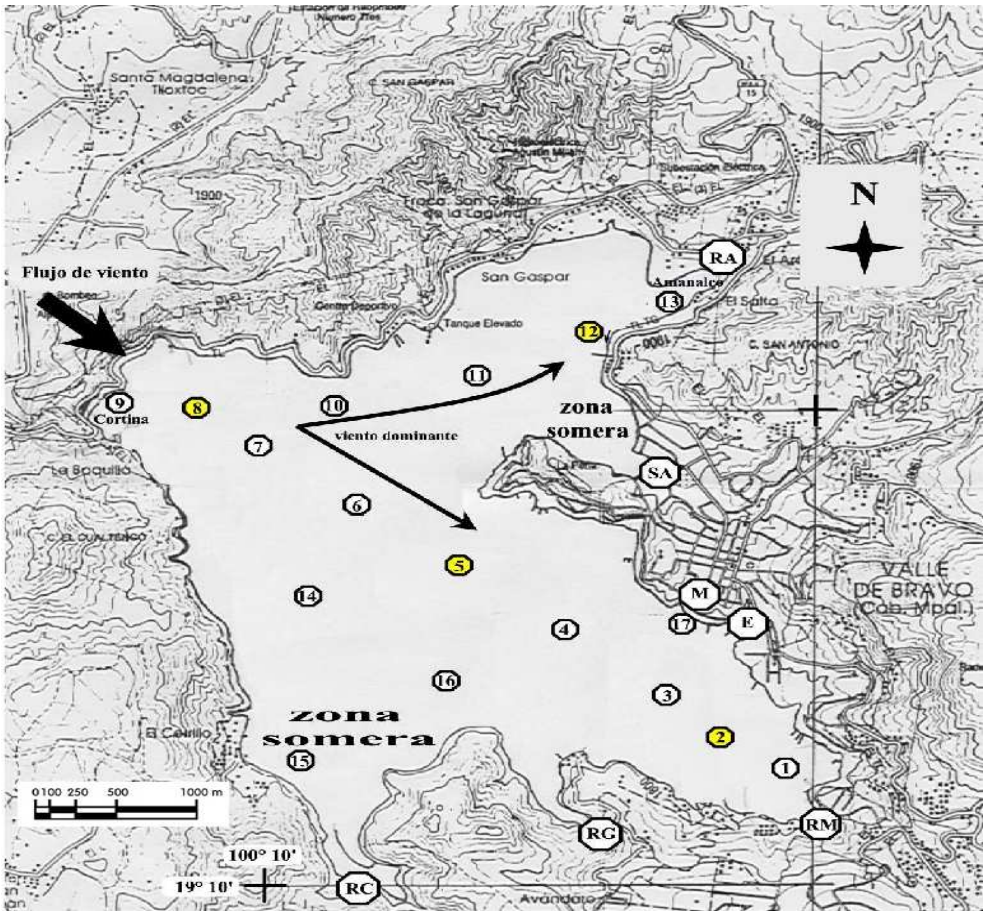

Fig. 1. Geographical setting of VB reservoir. Yellow circles represent the sampling stations established in the reservoir. Black bold arrow marks the location of dam.

CHAPTER II

ANALYSIS METHODS

As a necessary background for the discussion of methods implemented to analyze microstructure measurements, we now review some basic concepts and define the quantities that will be used in the discussion to follow.

When a thermally stratified fluid is stirred, it results in a production of TKE by Reynolds stresses working against the mean shear. Some of this TKE is dissipated by molecular viscosity while the rest is used to increase the potential energy of the system through the buoyancy flux. Turbulence, in the ocean, is described by a simple set of equations viz. TKE equation and an analogous equation for temperature variance (χ) [38]. The TKE equation, in an approximate form is [39]

$$\frac{d}{dt}\left(\overline{\frac{1}{2}k^2}\right) = -\overline{u'w'}\frac{\partial U}{\partial z} - \epsilon - g\frac{\overline{\rho'w'}}{\rho} \tag{2.1}$$

where, the left hand side represents the rate of change of TKE, on the right hand side first term is the production of TKE, the second term is dissipation and the last term represents increase in potential energy of the system, which can either be a source or a sink term. Primed variables are fluctuating quantities while unprimed are mean quantities (see Eq. (1.4) for definitions). All divergence and redistribution terms, from Reynolds decomposition, are ignored in the above equation. For isotropic turbulence, TKED (ϵ) is given in [29] as

$$\epsilon = \frac{15}{2}\nu\overline{\left(\frac{\partial u'}{\partial z}\right)^2} \qquad [Wkg^{-1}] \tag{2.2}$$

where ν is the kinematic viscosity and $\overline{(\partial u'/\partial z)^2}$ is the variance in the vertical gradient of turbulent fluctuations in the x direction (z down).

Similarly, stirring results in the movement of fluid parcels from warm to cold regions and vice versa. This leads to formation of thermal anomalies which soon begin to blend into the background by molecular heat diffusion. An equation for temperature fluctuations, analogous to that for TKE, is given in [29] as

$$\frac{d}{dt}\overline{\left(\frac{1}{2}T'\right)^2} = -\overline{w'T'}\frac{\partial T}{\partial z} - \frac{1}{2}\chi_T \tag{2.3}$$

where, the left hand side is the rate of change of temperature variance with time, the first term on the right-hand side describes the production of thermal anomalies by stirring while the rate of dissipation of thermal variance due to molecular diffusion is represented by the second term on the right-hand side. χ_T is analogous to ϵ and for isotropy is described as [29]

$$\chi_T = 2D\overline{\nabla T'^2} = 6D\overline{\left(\frac{\partial T'}{\partial z}\right)^2} \qquad [^oC^2 s^{-1}] \tag{2.4}$$

where D is the thermal diffusivity and $\overline{(\partial T'/\partial z)^2}$ is the variance of temperature gradient, which can be measured directly from SCAMP. In [9], a relationship based on the assumptions that (1) time rate of change of temperature variance is small and (2) buoyancy flux can be parameterized by a vertical heat flux diffusivity, K_T, was described as follows

$$-\overline{w'T'} = K_T \partial T/\partial z \tag{2.5}$$

Using Eqns. (2.3)- (2.5), the familiar Osborn-Cox relationship can be written as

$$K_T = (2 \pm 1) D C_x \qquad [m^2 s^{-1}] \tag{2.6}$$

where $C_x = \overline{(\partial T'/\partial z)^2}/(\partial \overline{T}/\partial z)^2$ is the Cox number. The factor (2±1) represents isotropy factors which in completely layered structure is equal to 1 and for isotropic

structure is equal to 3 [9]. In [29] and [39], it was further assumed that buoyancy flux can be parameterized by an eddy coefficient (K_ρ) as

$$-\overline{w'\rho'} = K_\rho \frac{\partial \rho}{\partial z} \tag{2.7}$$

If TKE levels remain constant (i.e. $\frac{d}{dt}\overline{k^2/2} = 0$), and defining the ratio of buoyancy flux to the turbulent production as flux Richardson number (R_f), then

$$K_\rho = \frac{R_f}{1 - R_f} \frac{\epsilon}{N^2} = \Gamma \frac{\epsilon}{N^2} \qquad [m^2 s^{-1}] \tag{2.8}$$

where Γ is the mixing efficiency (defined in Eq. (2.9)) and N is the Brunt-V*äisälä* frequency given by $N^2 = (g/\rho_o)\partial\overline{\rho}/\partial z$ where ρ_o is a reference density and ρ is the potential density. In [40], it was shown that if eddy coefficients for different scalar variables are same then K_ρ is equivalent to K_T. Using the definition of χ_T and Eq. (2.3), we can write

$$\Gamma = g\alpha \left(\frac{1}{3} \pm \frac{1}{6}\right) \frac{\chi_T}{\epsilon \partial \overline{T}/\partial z} \tag{2.9}$$

It was shown that it is possible to estimate χ_T directly and ϵ indirectly by fitting observed temperature gradient spectra to the theoretical "Batchelor" spectra (e.g. [26]; [27]; [28]; [29]), whose cutoff wavenumber depends on ϵ and thermal diffusivity.

In the section to follow, a summary of the "Batchelor" method to estimate ϵ is explained followed by a statistical analysis of various fitting parameters.

A. The Batchelor Spectrum

Batchelor [27] argued that turbulent motions of a fluid, arising from some external forcing, generate small-scale variations of passively conserved, diffusive scalars like temperature and salinity. He noted that the flow becomes a randomly straining

motion at scales smaller than the Kolmogorov length scale given by

$$k_s = (\nu^3 \epsilon^{-1})^{1/4} \qquad [m] \tag{2.10}$$

where ϵ is the TKED and ν is the kinematic viscosity. The Batchelor cut-off wavenumber, when the straining motion is balanced by corresponding diffusion, is defined as

$$k_B = \left(\frac{\epsilon}{\nu D^2}\right)^{1/4} \qquad [m^{-1}] \tag{2.11}$$

where D is the thermal diffusivity.

TKED is determined from profile segments of well-resolved temperature-gradient spectra. This spectrum of gradient fluctuations may be represented by the Batchelor form in one dimension as [27]

$$S(\hat{\kappa}) = \left(\frac{q}{2}\right)^{1/2} \frac{\chi_T}{\kappa_B D} g(q, \hat{\kappa}/\kappa_B) \tag{2.12}$$

where κ is the radian wave number, $\hat{\kappa}$ is the cyclic wavenumber $[m^{-1}]$, κ_B is the diffusive Batchelor cutoff wavenumber defined in Eq. (2.11) above, and χ_T is defined in Eq. (2.4).

The universal nondimensional spectral form $g(q, \hat{\kappa}/\kappa_B)$ as given in [27] is

$$g(q, \hat{\kappa}/\kappa_B) = 2\pi \left[e^{-\alpha^2} - \alpha \int_{\alpha}^{\infty} e^{-x^2/2}\, dx \right] \tag{2.13}$$

where

$$\alpha = (2q)^{1/2} (2\pi \hat{\kappa}/\kappa_B) \tag{2.14}$$

The universal constant q was estimated in [41] as 3.9 ± 1.5. In [42], theoretical range of q was shown to be $3^{1/2} < q < 2(3)^{1/2}$ while in [28] and [29], it was suggested

that q is in the range 3.4-4.1. However, a fixed value of q is used in this study ($q = 2\sqrt{3}$).

1. Estimation of TKED

TKED is an important parameter in turbulence mixing theory and knowledge of the magnitude of ϵ allows the estimation of the rate of vertical mixing, e.g., [43]; [44]; [45]. In [27], it was shown that the higher wavenumber part of one dimensional temperature gradient spectrum due to turbulence is a function of ϵ and the dissipation of temperature variance (χ). There are numerous comparisons of the theoretical universal temperature and temperature gradient spectra predicted in [27] with spectra measured in natural waters (e.g. [29]; [43]; [46]; [47]; [41]; [48]). In [28], a nonlinear least squares method was used to fit the Batchelor spectrum to well-resolved temperature gradient spectra with high signal-to-noise levels. In [49], it was shown that some temperature gradient spectra are difficult to fit this way because of instrument noise at the high wavenumber end of the spectra, and internal wave and finestructure contamination at the lower end. Luketina and Imberger[45] argue that their algorithm is robust in selecting the turbulent Batchelor component from temperature gradient spectra which have finestructure, internal wave, and noise contributions. In [26], an algorithm based on direct application of the maximum likelihood approach (MLE) was developed and its advantages over other least squares or cost-function based approaches were shown. MLE was shown to be robust and unbiased as compared to least squares and statistical quantities that indicated the goodness of a fit were defined, thereby making the analysis completely automated [26].

As an example, MLE fit to a raw data segment in the BBL at Station 5 is shown in Fig. 2. Two horizontal green lines in the left panels demarcate the segment selected for the fit (includes 512 points, i.e. $\sim$0.5m in the vertical), while the right

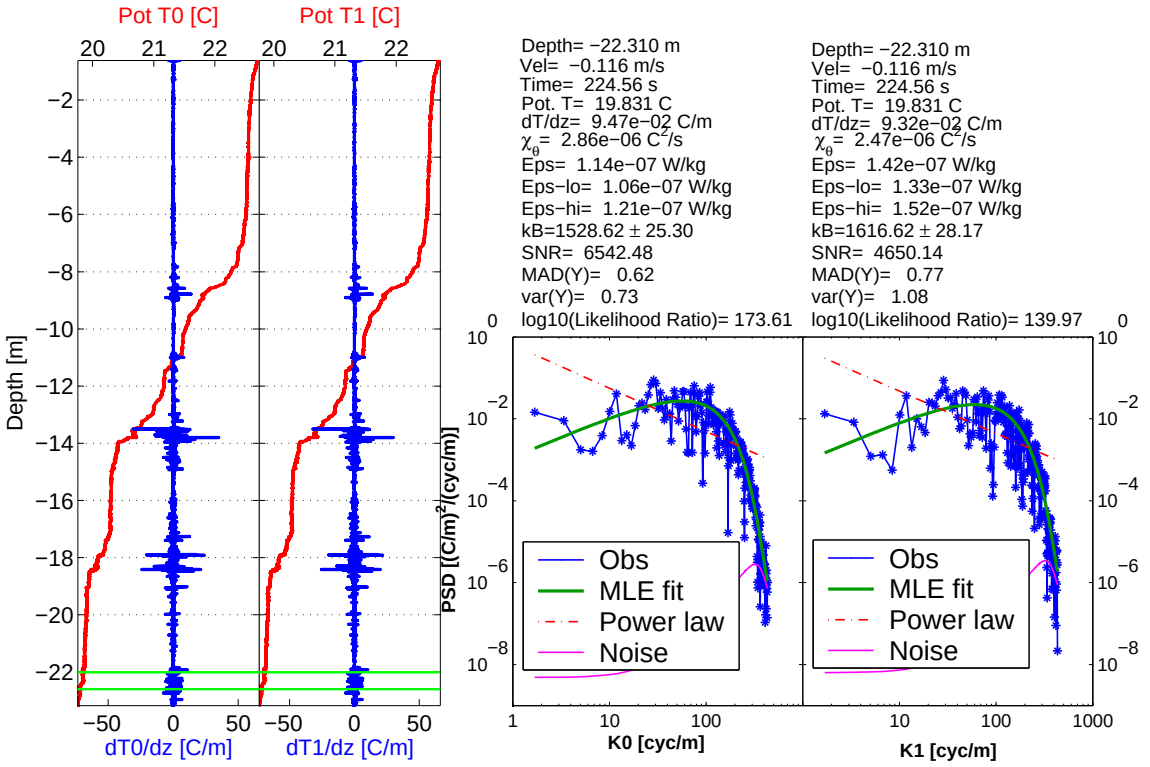

Fig. 2. Estimation of TKED, ϵ; the left two panels show Fast T0 and Fast T1 temperature profiles (red line) overlaid by their respective gradients (blue line); the right two panels show a fit of data (blue line) to a theoretical Batchelor Spectra (green line), and modelled noise spectra (magenta line).

panels show fits to the Batchelor Spectrum for the two Fast temperature sensors. By visual inspection, we can clearly see that the fit is very good.

We used three different approaches in spectral analyses to estimate ϵ : 1) segment length = 128 points ($\sim$ 0.12 m) with no overlap, (2) segment length = 512 points ($\sim$ 0.5 m) with half overlap and (3) segment length = 512 points with no overlap. We analyzed all the segments from all the profiles and based on a visual inspection we accepted or rejected a fit. After rejecting the fits based on visual inspection, we examined four different fit parameters :

- Signal to Noise Ratio (SNR),
- Likelihood Ratio (LR) - the ratio of likelihood of Batchelor fit and the straight line fit using power law (red dash-dot line in Fig. 2),
- Mean Absolute Deviation (MAD) - the average of the absolute differences between the reduced chi-square probability density function (χ^2 pdf) and the mean of the reduced χ^2 pdf,
- Variance (VAR) - the variance of the reduced χ^2 pdf.

We performed a statistical analysis to estimate critical values of these parameters to suggest a rejection criteria. It was noted that the fits accepted based on visual inspection had high SNRs, high LRs, low MADs and low VARs. Henceforth, we performed the statistical analyses only on the "rejected" fits to arrive at critical values that will allow us to automate the rejection of "bad" fits.

In [26], it was shown that VAR is more sensitive to outliers and thus they suggested that the most successful pair of rejection measures is MAD and log_{10}(LR). Histograms and cumulative distribution functions were plotted for 5991 rejected fits from a SCAMP dataset of 26066 segments based on visual inspection (Fig. 3). (About 23% ($\sim$ 5991/26066) of the fits are considered bad based on visual inspection).

We used different combinations of SNR, LR, MAD and VAR to minimize inclusion of bad fits. Table I summarizes these combinations and we suggest that a given data segment be rejected *if any* of the following criteria are true:

- SNR is less than 5,
- MAD is greater than 1
- log_{10}(LR) is less than 2

Table I. Summary of rejection criteria for 5991 rejected fits.

SNR	log_{10}LR	VAR	MAD	% of bad fits passed
5	2	5.7	1	6.7
5	2	5.7	1.2	9
5	5	5.7	1.2	8.3
5	10	5.7	1.2	7
10	2	5.7	1.2	6.8

We can see from Table I that if we use the above rejection criteria, $\sim 6.7\%$ of the bad fits will still pass.

Estimation of ϵ done using three different techniques is shown (Fig. 4(a), (b), and (c)). Note that by using larger segments one obtains vertically smoother estimates (Fig. 4(a) and (b)), however, the main features, albeit with less vertical resolution, remain similar. We can also see that the estimates from the automated analysis compare favorably with those obtained using visual inspection (Fig. 4(c)).

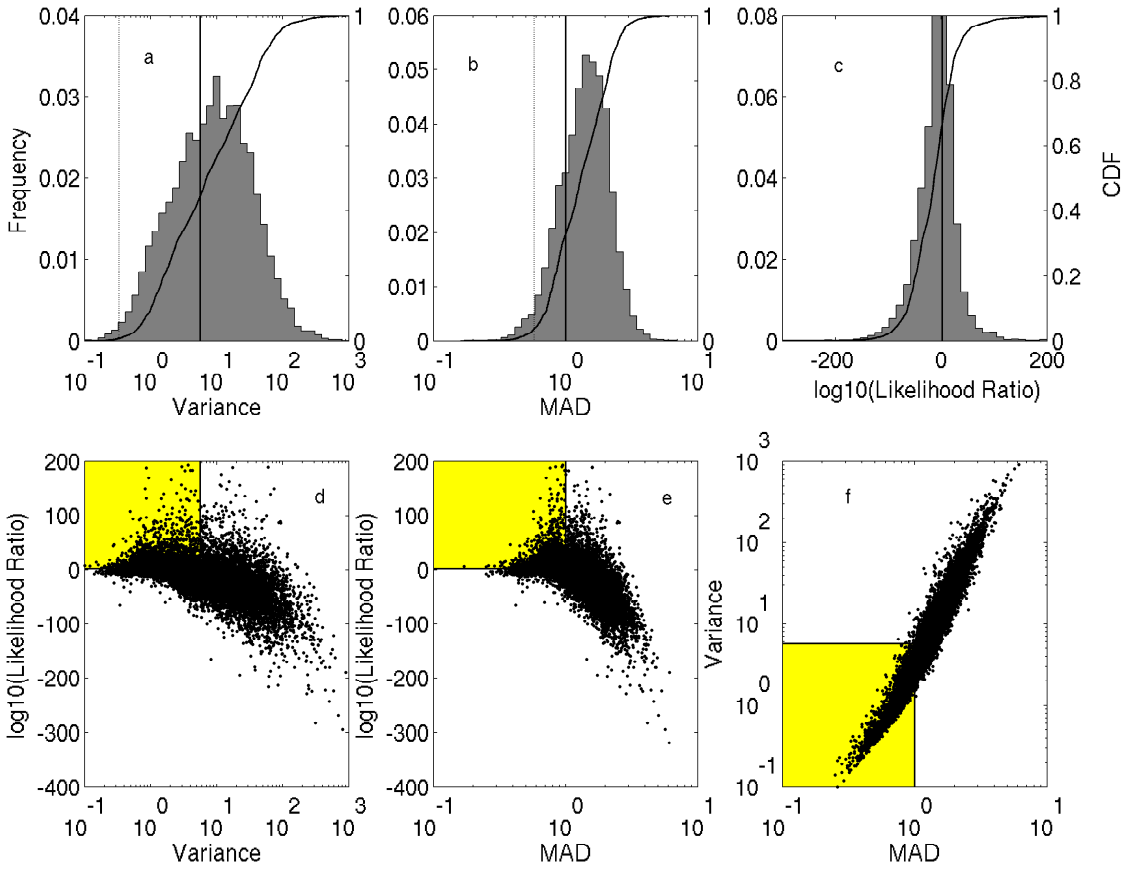

Fig. 3. Histogram and cumulative distribution function plots for a total of 5991 rejected segments obtained from visual inspection of SCAMP dataset with 26066 segments - (a) Variance, (b) MAD and (c) log_{10}(LR); Solid lines in (a)-(c) show our rejection limits; Dotted vertical line in (a) shows theoretical perfect fit variance ($2/d = 1/3$) while in (b) it shows perfect fit MAD ($(\overline{(2/d)}^{1/2}$) where d is the degree of freedom; (d) Scatterplot of log_{10}(LR) vs. VAR; (e) Scatterplot of log_{10}(LR) vs. MAD; and (f) Scatterplot of VAR vs. MAD. Yellow regions indicate fits considered bad based on visual inspection but that do pass the automated rejection criteria.

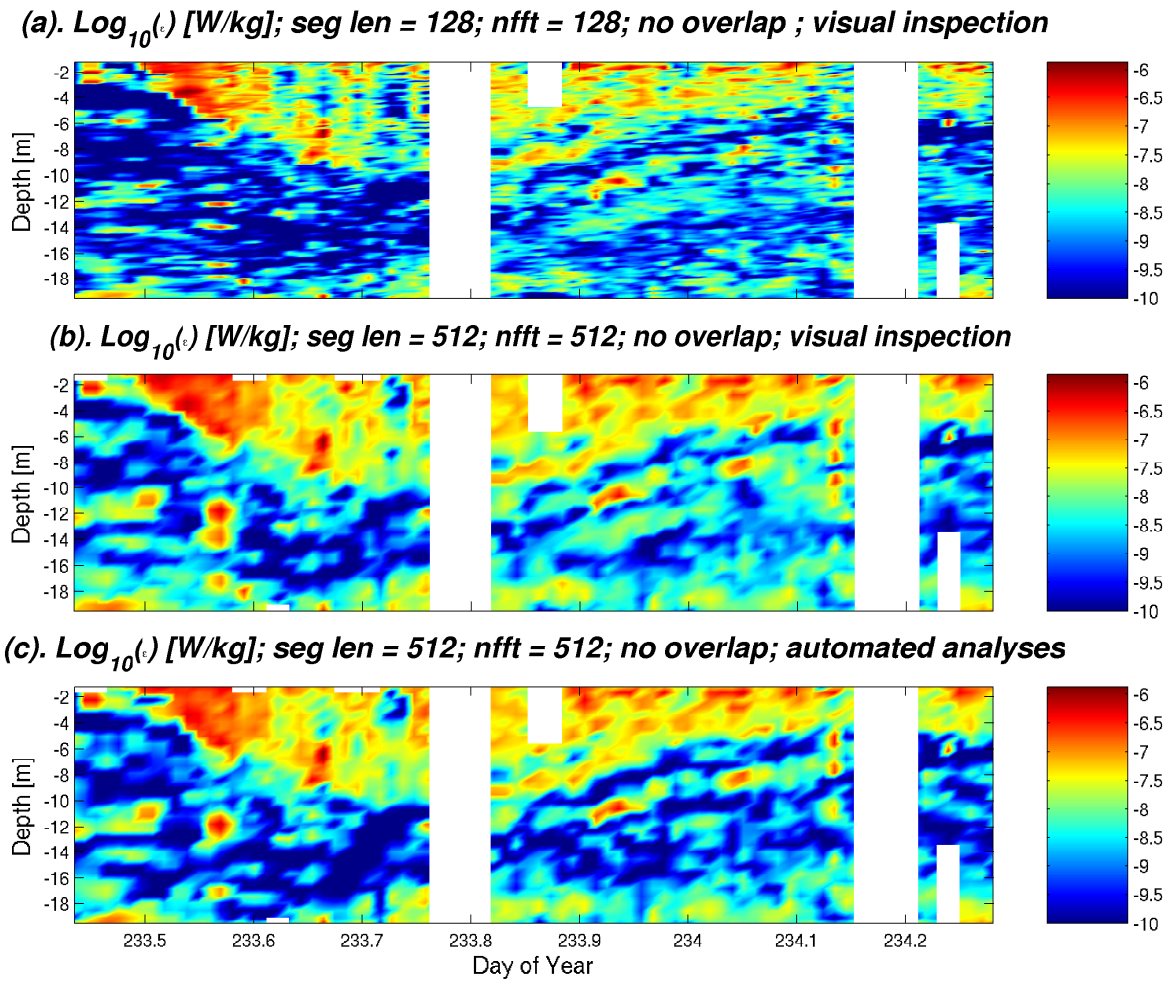

Fig. 4. Contour plot of ϵ estimated using various techniques - (a) Visual inspection for goodness of fit and segment length = 128; (b) Visual inspection and segment length = 512; and (c) Automated rejection criteria and segment length = 512.

CHAPTER III

OBSERVATIONS

Observational data for this study were collected at four stations - Station 2, 5, 8 and 12 between August 21-25, 2003 (Fig. 1). The next section describes the observations from SCAMP; water-current measurements are then explained followed by the surface meteorological observations. The last section shows contour plots of SCAMP microstructure data along with the surface forcing (heat flux and wind stress).

A. Temperature Microstructure

1. Instrumentation

The data for the present discussion were obtained using the temperature microstructure profiler SCAMP. This instrument consists of a cylinder 0.06 m in diameter and 0.76 m long containing electronics with forward mounted sensors protected by a sensor guard. The sensors mounted on SCAMP are two Fast Temperature sensors (Fast T0 and Fast T1; Thermometrics FP07 thermistor with an accuracy of $+/-0.050^{o}$C), one Fast Conductivity sensor (Fast C; PME 4-electrode sensor with an accuracy of $+/-5\%$ full scale depending on calibration), one Accurate temperature (Acc T; Thermometrics P85 thermistor with an accuracy of $+/-0.020^{o}$C), one Accurate conductivity (Acc C; PME 4-electrode ceramic sensor with an accuracy of $+/-0.2\%$ full scale) and a pressure sensor (Keller PSI PAA-10 with an accuracy of $+/-0.5\%$ full scale). The instrument is buoyancy balanced and drag-stabilized to free-fall at a nominal rate of 0.1 m/sec while sampling all sensors at 100 Hz. It is recovered after each profile and redeployed using a light, neutrally buoyant Kevlar tether line.

Vertical profiles of temperature microstructure in the water column were collected

every 10-15 minutes using SCAMP. Over 350 profiles were collected during the entire length of the experiment. An example of a raw SCAMP profile with panels showing the various measured paramters is shown (Fig. 5).

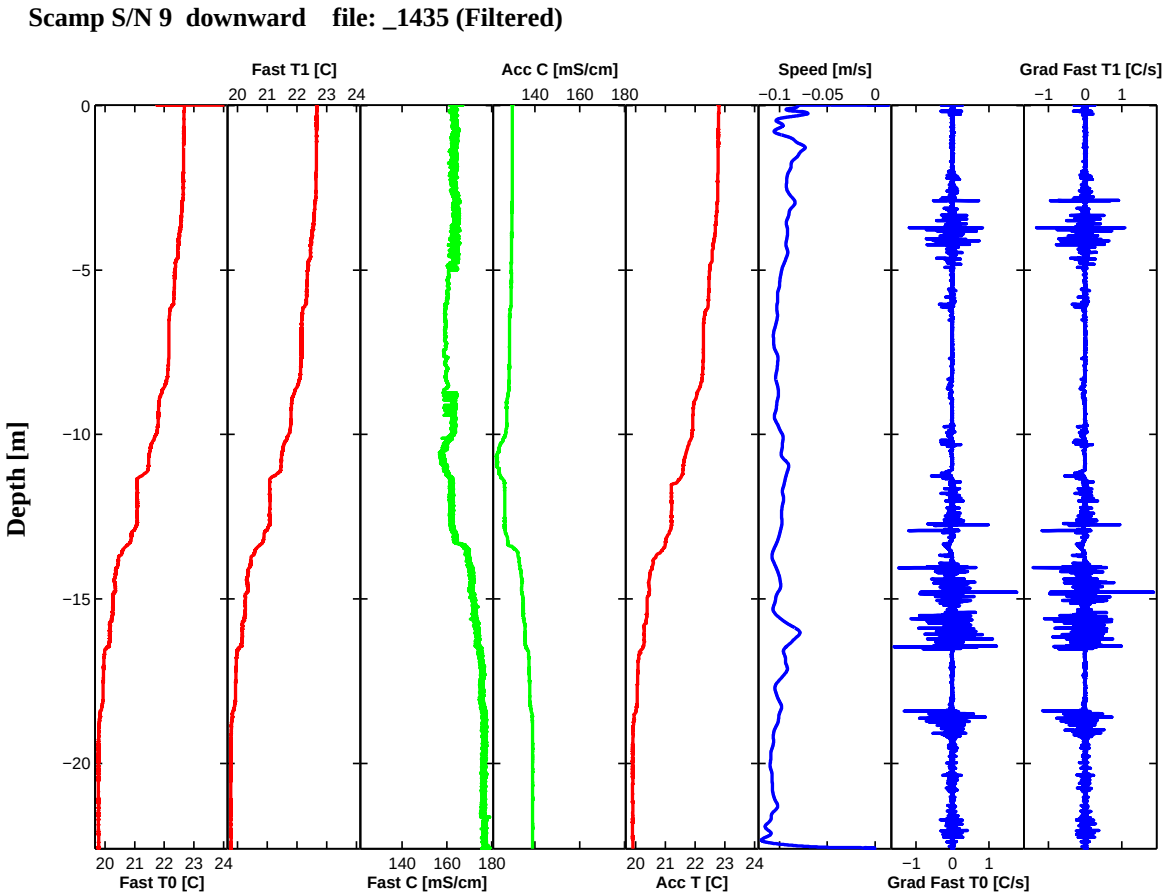

Fig. 5. A plot of a typical SCAMP profile during daytime collected at station 5; the panels show (from L to R) profiles of Fast T0, Fast T1, Fast C, Acc C, Acc T, descend speed and microstructure temperature gradients, Grad Fast T0 and Grad Fast T1.

2. SCAMP Observations

In this section we present plots of observed data from SCAMP and compute various quantities from the measured data. Daytime and night-time profiles for all the sta-

tions are averaged for potential temperature (θ), salinity(S), potential density (σ_θ), buoyancy frequency(N), TKED (ϵ), chi (χ), vertical heat flux diffusivity (K_T) and eddy diffusivity (K_ρ). A representative day-time profile is shown in Fig. 5 while that for night-time is shown in Fig. 6

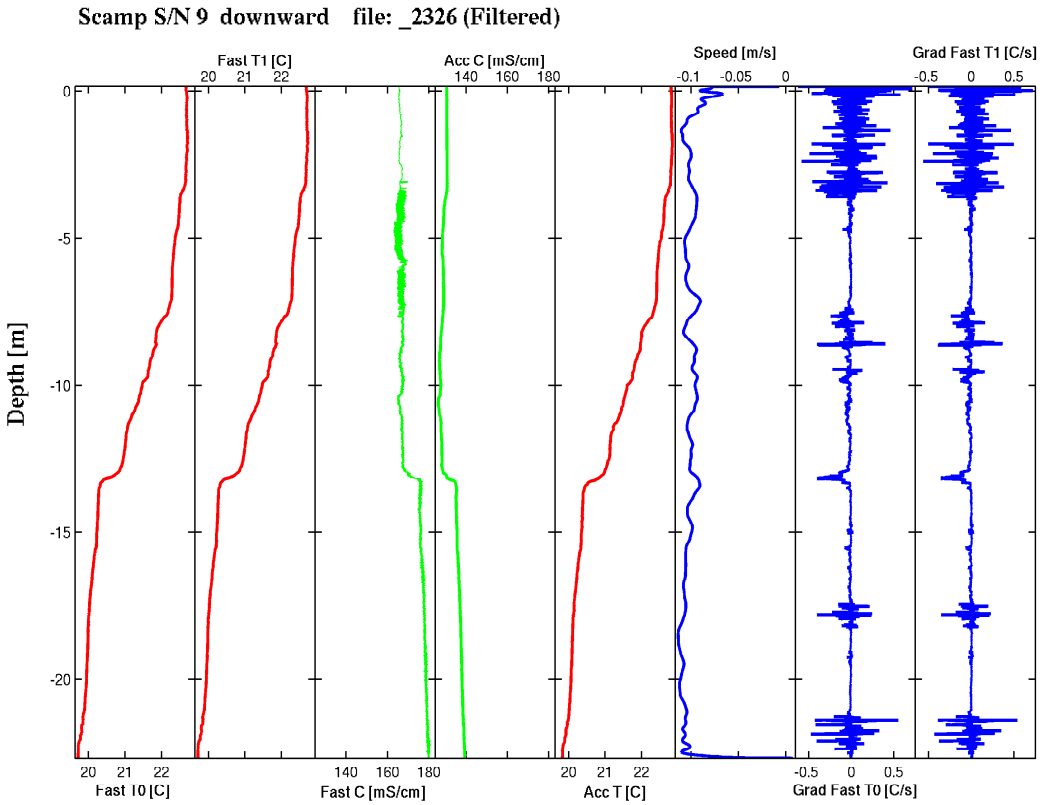

Fig. 6. A plot of a typical SCAMP profile during night-time collected at station 5. All panels are similarly defined as in Fig. 5.

S and σ_θ were calculated using the fresh water equation of state [30], buoyancy frequency squared is defined in Eq. 2.8; TKED was estimated through Batchelor Spectrum; χ was estimated from Eq.(2.4); K_T and K_ρ were calculated from Eqs. 2.6 and 2.7 as

$$K_T = \frac{\chi}{2(\partial T/\partial z)^2}; \qquad K_\rho = \frac{\Gamma\epsilon}{N^2} \tag{3.1}$$

where Γ is as defined in Eq. 2.9.

From the data plotted for Station 2 (Fig. 7), we can see that the thermocline depth is not well defined during the day but during night-time a relatively sharp thermocline developed at depths of $\sim$ 4 m (Fig. 7(a) and (b), panel(i)). An upward movement of relatively fresher water from 14-16 m during the day, to 6-10 m during the night was observed and is consistent with the passage of internal wave noticed at this station (Fig. 7(a) and (b), panel(ii)). Dissipation rates (χ and ϵ) were large in the surface layer (SL) and near-bottom ($\chi \sim 10^{-6}C^2/s$ and $\epsilon \sim 10^{-6}W/kg$) but in the thermocline region they decreased significantly ($\sim 10^{-9}$ in equivalent units for both χ and ϵ).

At station 5, the water column was weakly stratified with surface temperatures of 23^oC while near bottom temperatures were 20^oC during both day and night (Fig. 8(a) and (b), panel(i)). Several strong mixing events, similar to those at station 2, were observed in the BBL during daytime at this station (Fig. 8(a) panels (v) and (vi)). Values of χ and ϵ during this time were on the order of $10^{-6}C^2/s$ and $10^{-7}W/kg$ respectively. A probable explanation for this strong mixing is internal wave breaking over a sloping bottom. This is further discussed in detail in the next chapter with the aid of numerical model simulations. At night, the intensity of mixing in the BBL reduced to values of $\chi \sim 10^{-8}C^2/s$ and $\epsilon \sim 10^{-9}W/kg$.

The deepest station (station 8, $\sim$ 30m) was marked by an inflow of water through a dam into the reservoir (Fig. 1). At this station, the water column temperature structure did not change much from day to night maintaining SL temperatures around 22.5 deg C and near-bottom temperatures $\sim$ 20 deg C (Fig. 9).

The last sampling station was the shallowest (station 12, $\sim$ 15m). During the day, the thermocline was relatively close to the bottom $\sim 7m$ (Fig. 10(a), panel (i)), but during night, the water column became weakly stratified with the thermocline

depth shallowing to $\sim 5m$ (Fig. 10(b), panel(i)). Several strong mixing events were observed during the daytime when the thermocline was relatively close to the bottom (Fig. 10(a), panels (v) and (vi)) and the values of both χ and ϵ were relatively high ($\chi \sim 10^{-6}C^2/s$ and $\epsilon \sim 10^{-7}W/kg$).

Table II. Averaged day and night-time values for all stations. Mixed layer depth (MLD), D, was determined visually for each profile and then averaged for all the profiles. L is the Monin-Obukhov length scale (Eq. 4.14).

	Day				Night			
	2	5	8	12	2	5	8	12
Number of profiles	36	36	29	48	46	49	35	65
$\tau(N/m^2)$	0.018	0.014	0.018	0.015	0.0012	0.0032	0.0037	0.002
D (m)	-7.31	-7.82	-7.86	-6.38	-5.47	-7.88	-7.94	-5.34
L (m)	4.23	2.01	2.21	0.99	-0.05	-0.16	-0.21	-0.13
$J_q^0(W/m^2)$	-39.09	-171.4	-318.24	-260.06	155.4	177.1	169.25	145.3
$10^{-8}\ J_b^0(W/kg)$	-2.29	-9.6	-17.56	-14.38	8.27	9.5	9.14	7.79

Table II summarizes the averaged day and night-time values for all the stations. Wind stress, τ, and surface buoyancy flux, J_b^0, were determined from bulk aerodynamic formulas (e.g. [31]; [32]; [33]). Wind was found to be the major force driving mixing in the SL during the day while during night, convection ws the major driving force. This can be seen from the negative sign of L (Monin-Obukhov length) in Table II during night-time. Also during night-time, $\mid D/L \mid \gg 1$, which implies that most of the mixed layer (i.e. $D < z < L$) is dominated by convectively driven turbulence [50].

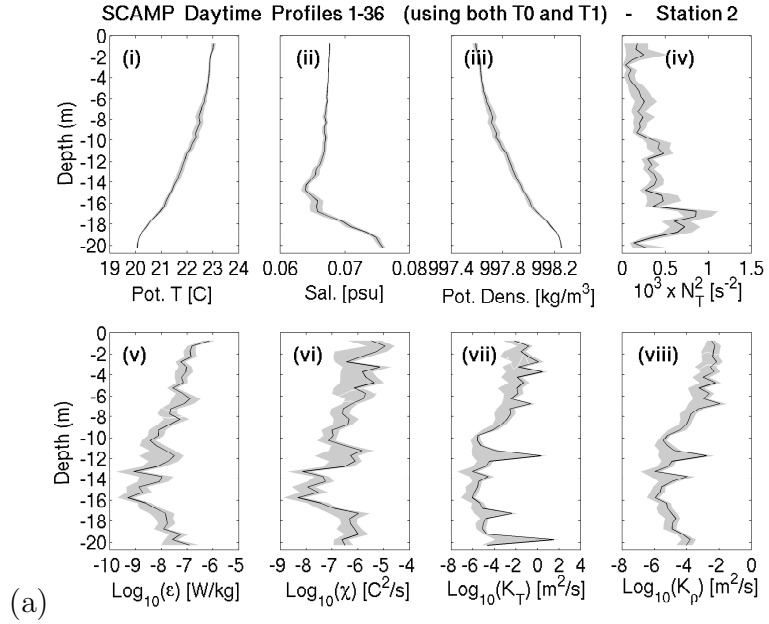

(a)

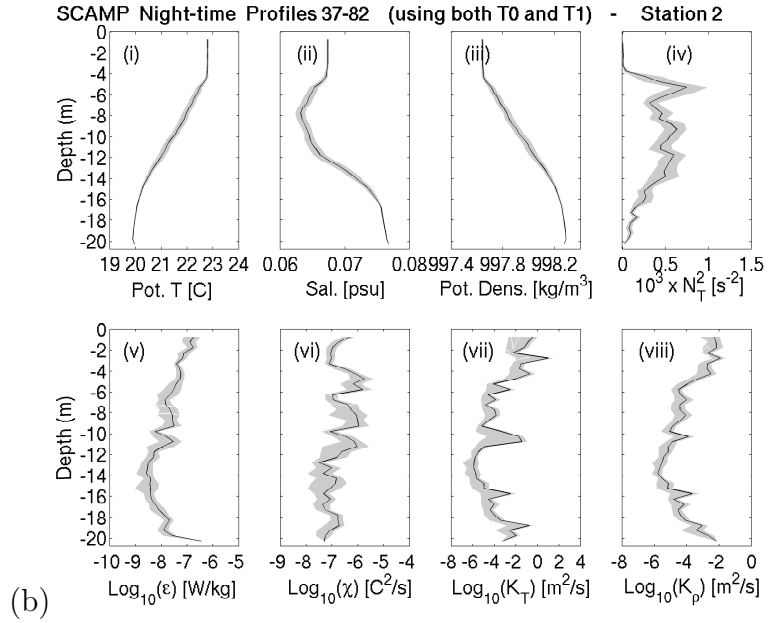

(b)

Fig. 7. (a) Averaged daytime profiles; (b) Averaged night-time profiles of various measured and computed quantities from station 2. In both figures, panels show (i) Potential Temperature (^{o}C); (ii) Salinity (psu); (iii) σ_θ (kg/m^3); (iv) Buoyancy frequency squared (s^{-2}); (v) TKED (W/kg); (vi) χ (C^2/s); (vii) K_T (m^2/s); and (viii) K_ρ (m^2/s). Shaded regions show 95% confidence intervals.

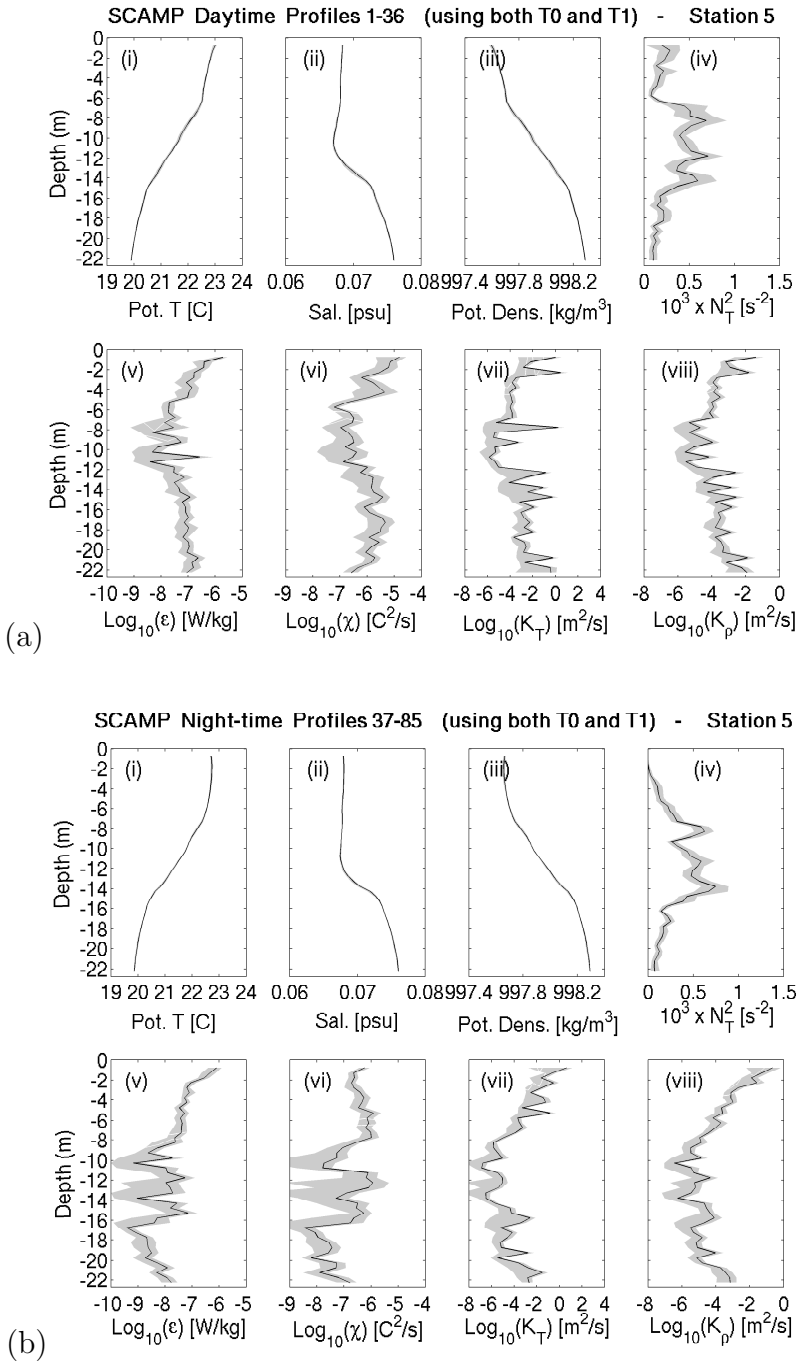

Fig. 8. Same as Fig. 7 but for station 5.

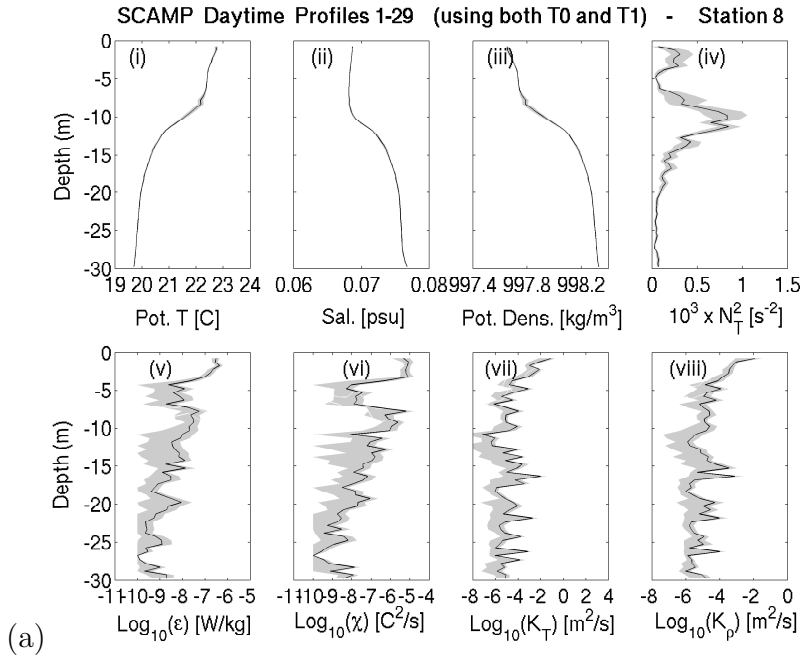

(a)

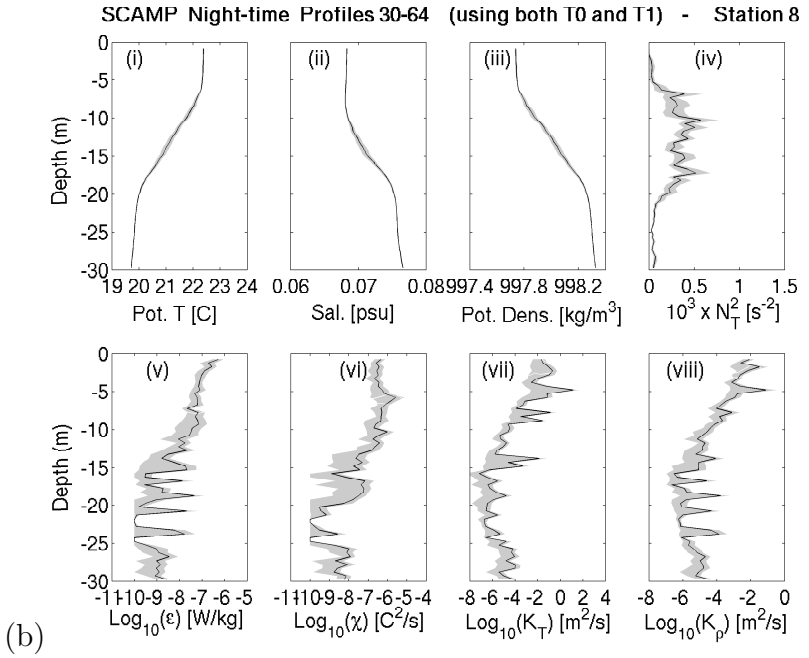

(b)

Fig. 9. Same as Fig. 7 but for station 8.

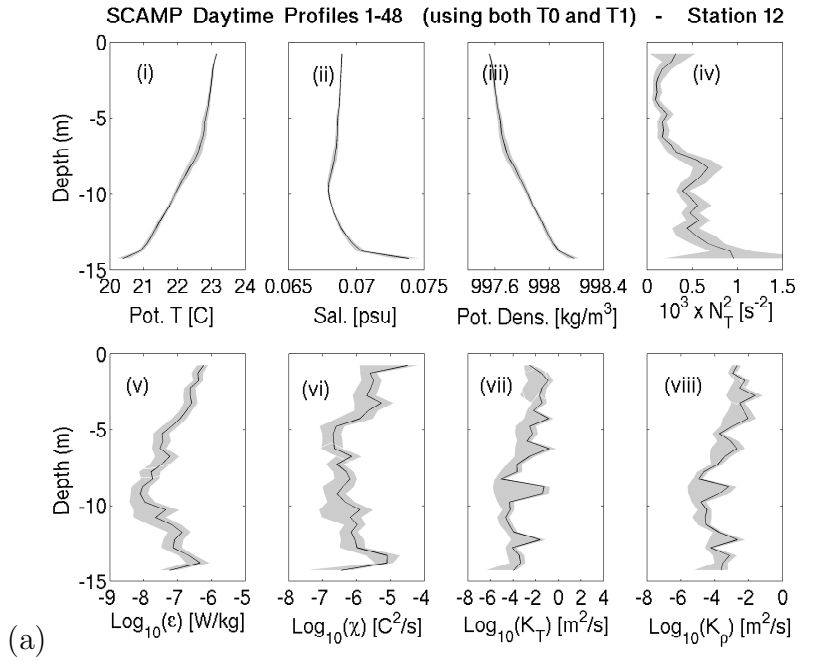

(a)

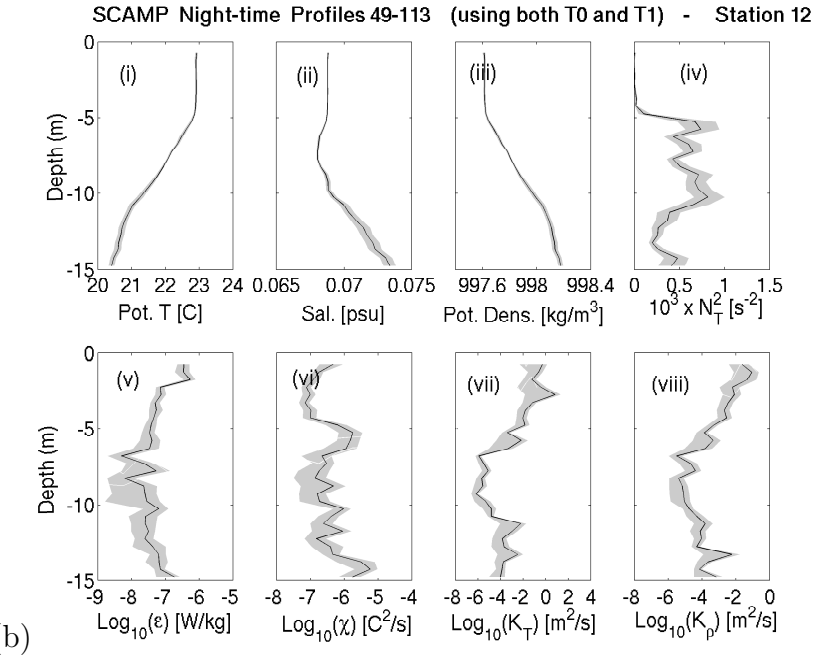

(b)

Fig. 10. Same as Fig. 7 but for station 12.

3. Statistics

Statistical analysis of turbulence dissipation rates was performed to check if they fit the lognormal distribution. In [51], it was shown that TKED has a lognormal distribution *if* TKED is homogeneous in the domain; the averaging scale is small compared to length scale of the domain; and the averaging scale is large compared to the Kolmogorov scale, k_s, defined in Eq. (2.10). The last two conditions can easily be satisfied but the condition of homogeneity is seldom satisfied due to the patchy nature of turbulence and dissipation rate datasets thus fail statistical tests for lognormality (e.g. [10]; [51]; [52]; [53]). In [50]; [54]; and [55], it was shown that dissipation rates are lognormal in the SL and the BBL. However dissipation rates were found to deviate from such behavior in between these layers (e.g. [10]; [51]).

For this study, the averaging scale is the vertical bin size where TKED estimates were averaged (~ 0.5 m) while the length scale is on the order of 20 m which is fairly large compared to the averaging scale. For oceans, k_s is on the order of 0.1 m [51] while for VB, k_s is on the order of 0.05 m (using Eq. (2.10) with $\epsilon \sim 10^{-7}$ W/kg and $\nu = 10^{-4} m^2/s$) which satisfies the last condition. The only condition left to be satisfied is that TKED should be homogeneous in the domain.

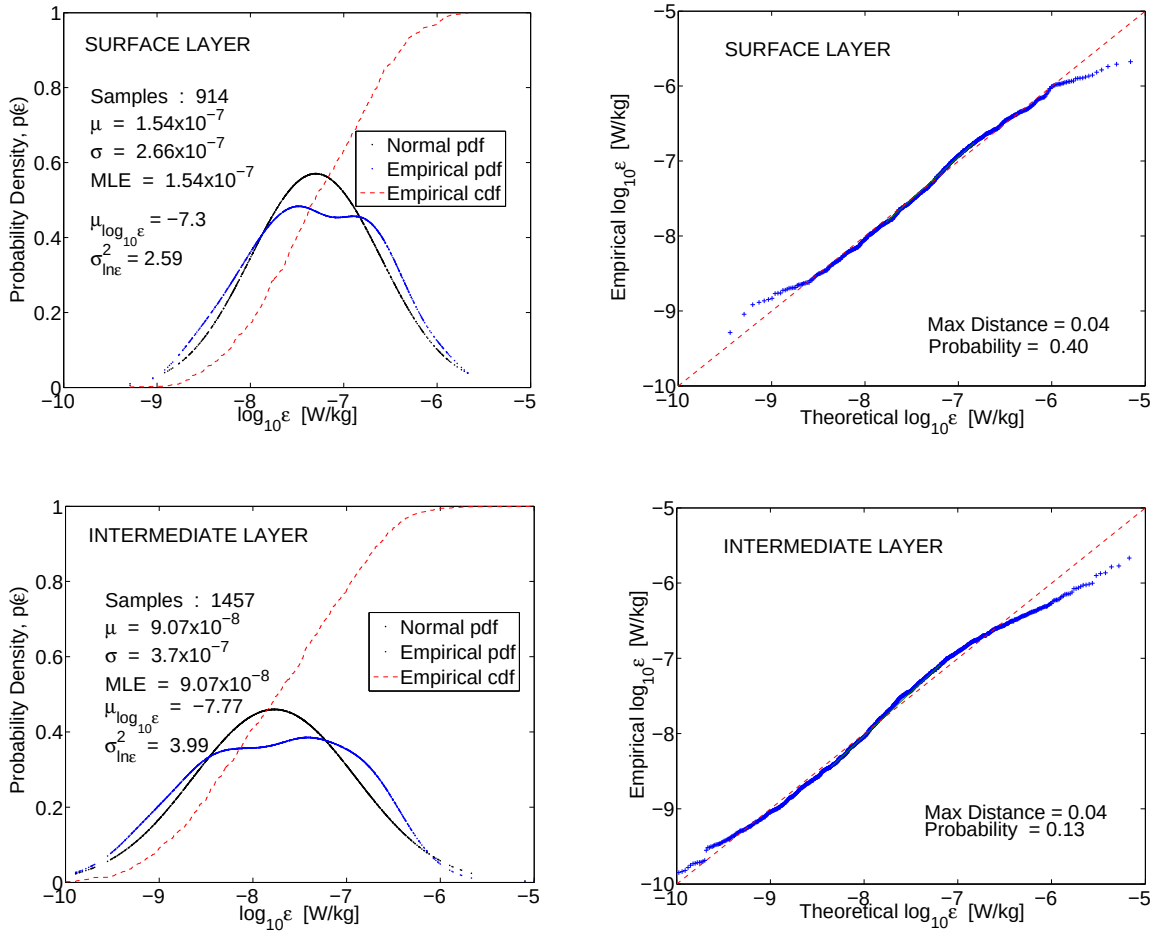

Fig. 11. PDF (left) and QQ (right) plots for $log_{10}\ \epsilon$ in the SL (top) and the IL (bottom) during day-time. In the left panels, the blue curve is the empirical pdf, the black curve is the fitted normal pdf, and the red dashed line is the empirical cumulative density function (cdf). For the right panels, the blue curve represents the QQ plot of observed $log_{10}\ \epsilon$ versus a theoretical normally distributed $log_{10}\ \epsilon$ and the red dashed line represents the best fit to normal distribution. μ is the arithmetic mean, σ is the standard deviation, MLE is the maximum likelihood estimator for $log_{10}\ \epsilon$, $\mu_{log_{10}\epsilon}$ is the mean of $log_{10}\ \epsilon$, and $\sigma^2_{ln(\epsilon)}$ is the square of standard deviation of $ln\ \epsilon$. Maximum distance (d_{max}) and probabilities in QQ plots are obtained from KS2 test (Appendix B).

PDFs were computed separately for the SL, the intermediate layer (IL) and the BBL for both χ and ϵ. Agreement of expected values of TKED (MLE in Figs. 11 and 12) with arithmetic mean (μ) provides one indication of agreement with the lognormal distribution [56].

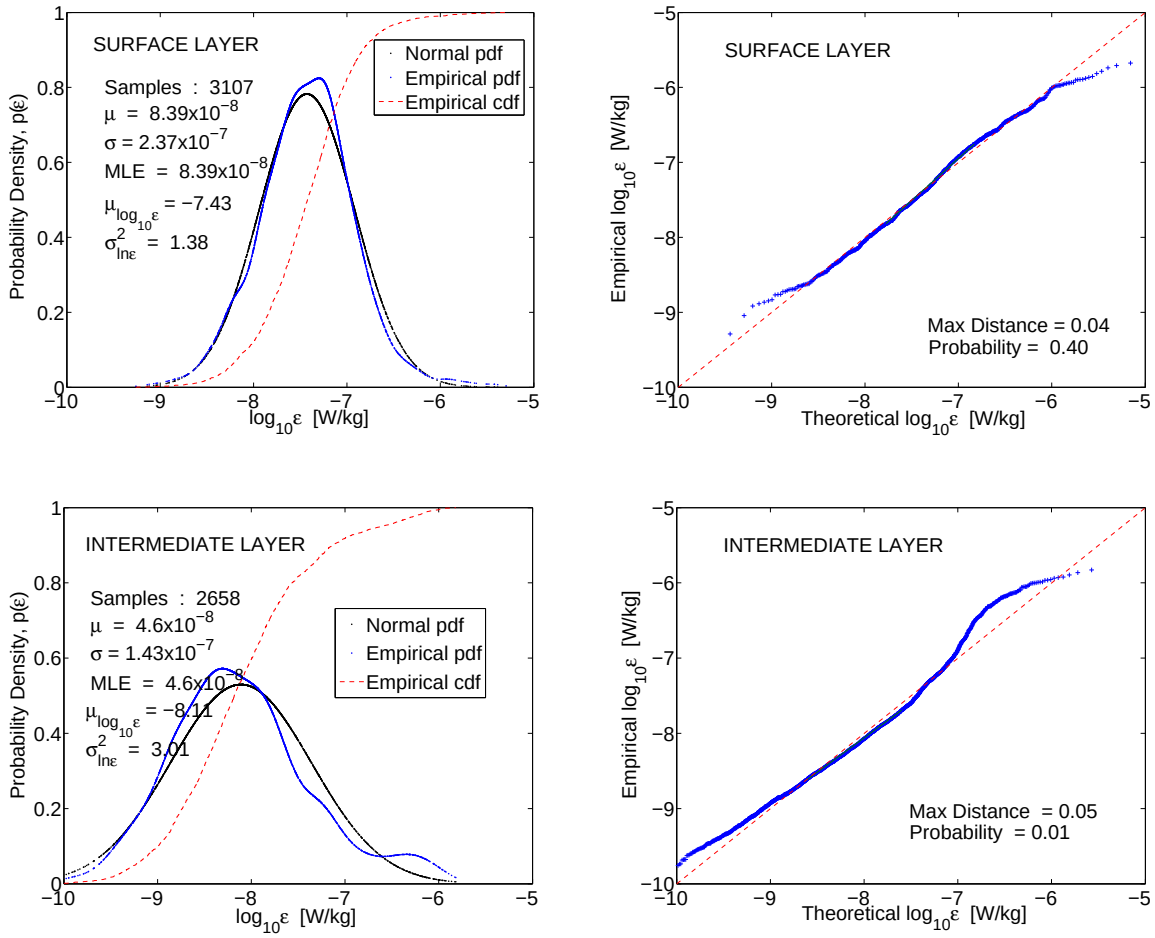

Fig. 12. Same as Fig. 11 but for night-time.

Table III. Mean (μ), standard deviation (σ), MLE, d_{max}, and d_{crit} values for χ and ϵ in the SL and the IL. d_{max} and d_{crit} are defined in Appendix B. If $d_{max} < d_{crit}$, the null hypothesis is accepted and the data follows a lognormal distribution.

	Day				Night			
	χ		ϵ		χ		ϵ	
	SL	IL	SL	IL	SL	IL	SL	IL
Samples	914	1457	914	1457	3107	2658	3107	2658
$10^{-8}\mu$	322	235	15.4	9.07	50.5	94.5	8.39	4.60
10^{-8} MLE	323	235	15.4	9.07	50.5	94.5	8.39	4.60
$10^{-7}\sigma$	113	717	2.66	3.7	17.3	38.8	2.37	1.43
d_{max}	0.06	0.03	0.04	0.04	0.04	0.02	0.03	0.05
d_{crit}	0.064	0.051	0.064	0.051	0.035	0.038	0.035	0.038
Null Hypothesis	Accept	Accept	Accept	Accept	Reject	Accept	Accept	Reject

Table IV. Same as Table III but for BBL.

	χ	ϵ
Samples	2032	2032
$10^{-8}\mu$	96	7.1
10^{-8} MLE	96	7.1
$10^{-7}\sigma$	51.1	2.07
d_{max}	0.03	0.02
d_{crit}	0.043	0.043
Null Hypothesis	Accept	Accept

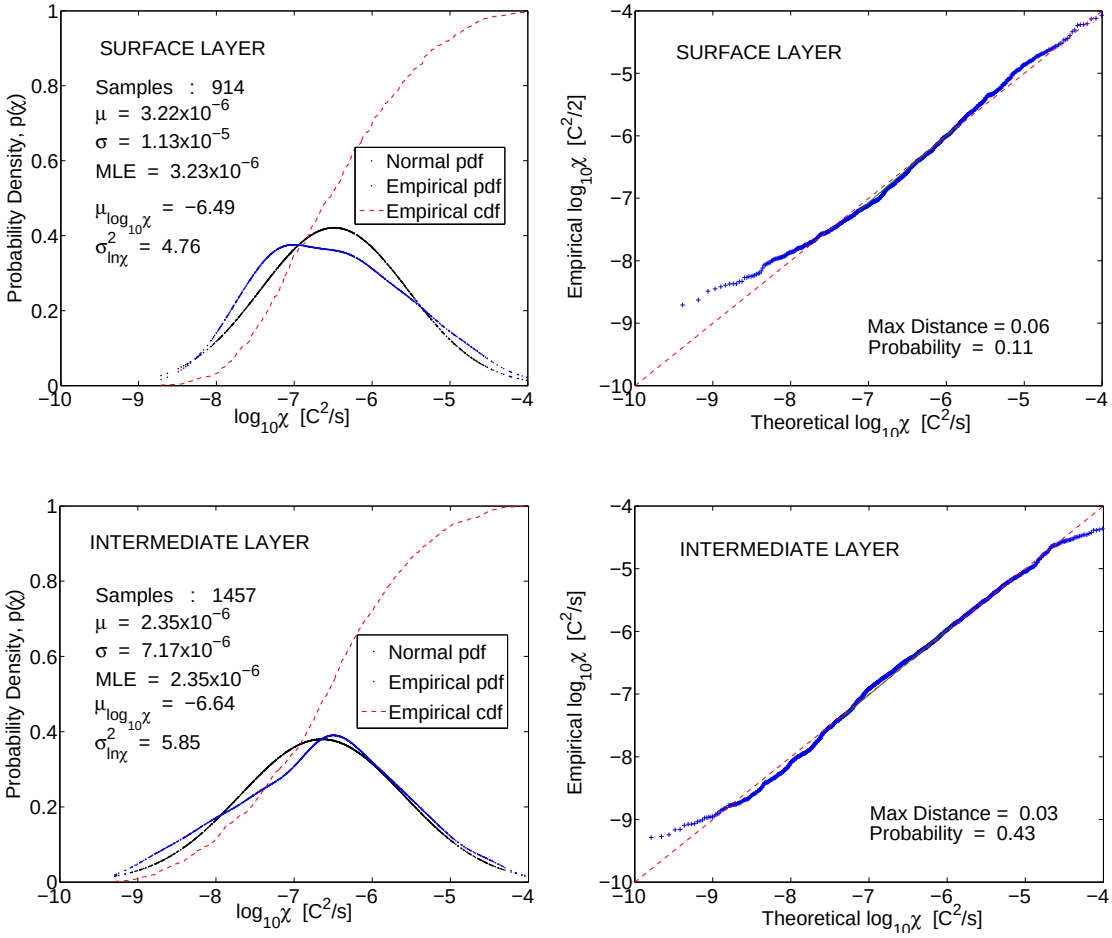

Fig. 13. PDF (left) and QQ (right) plots for $log_{10}\ \chi$ during day time. All panels have similar definitions as in Fig. 11.

A two-sample Kolmogorov-Smirnov test (hereafter, the KS2 test) was performed for theoretical and empirical values of TKED, and the KS2 statistic was calculated (Appendix B). KS2 test accepted the null hypothesis that TKED followed a lognormal distribution at 5% significance level during daytime in the SL and the IL, but failed in the IL during night-time (Table III).

From a similar analysis, $log_{10}\ \chi$ was found to be normally distributed (Figs. 13

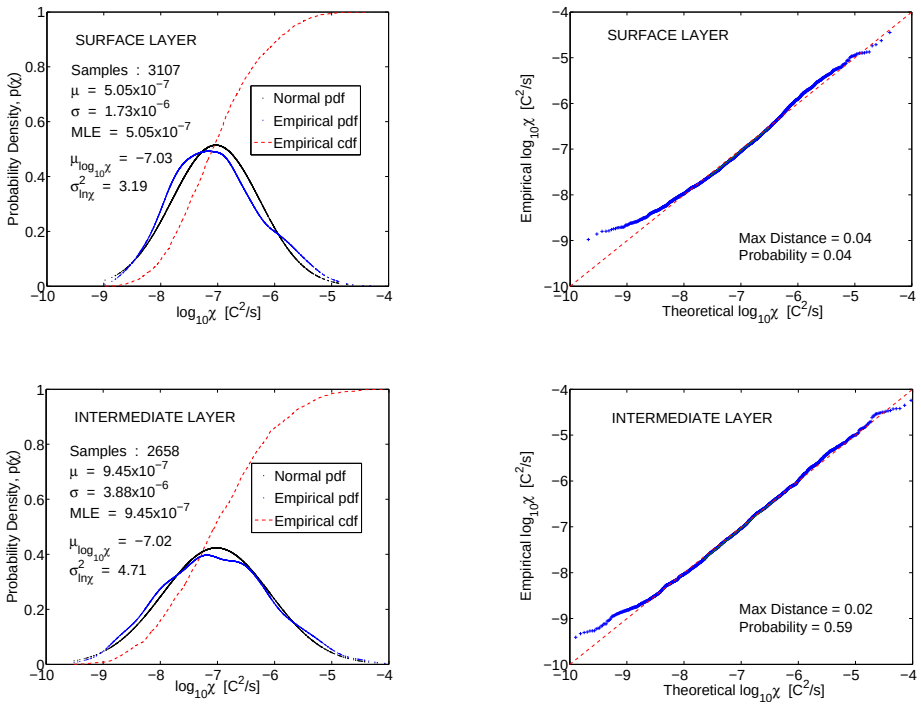

Fig. 14. Same as Fig. 13 but for night-time.

and 14) in the SL and IL during day and night.

We did a similar analysis in the BBL, but combined the day and night time samples since there was no significant change in the dynamics of mixing processes in the BBL (Fig. 15). KS2 test accepted the hypothesis that both χ and ϵ were lognormally distributed in the BBL.

Table III summarizes the statistical quantities computed in the SL and the IL during day and night for χ and ϵ while Table IV summarizes the values in the BBL.

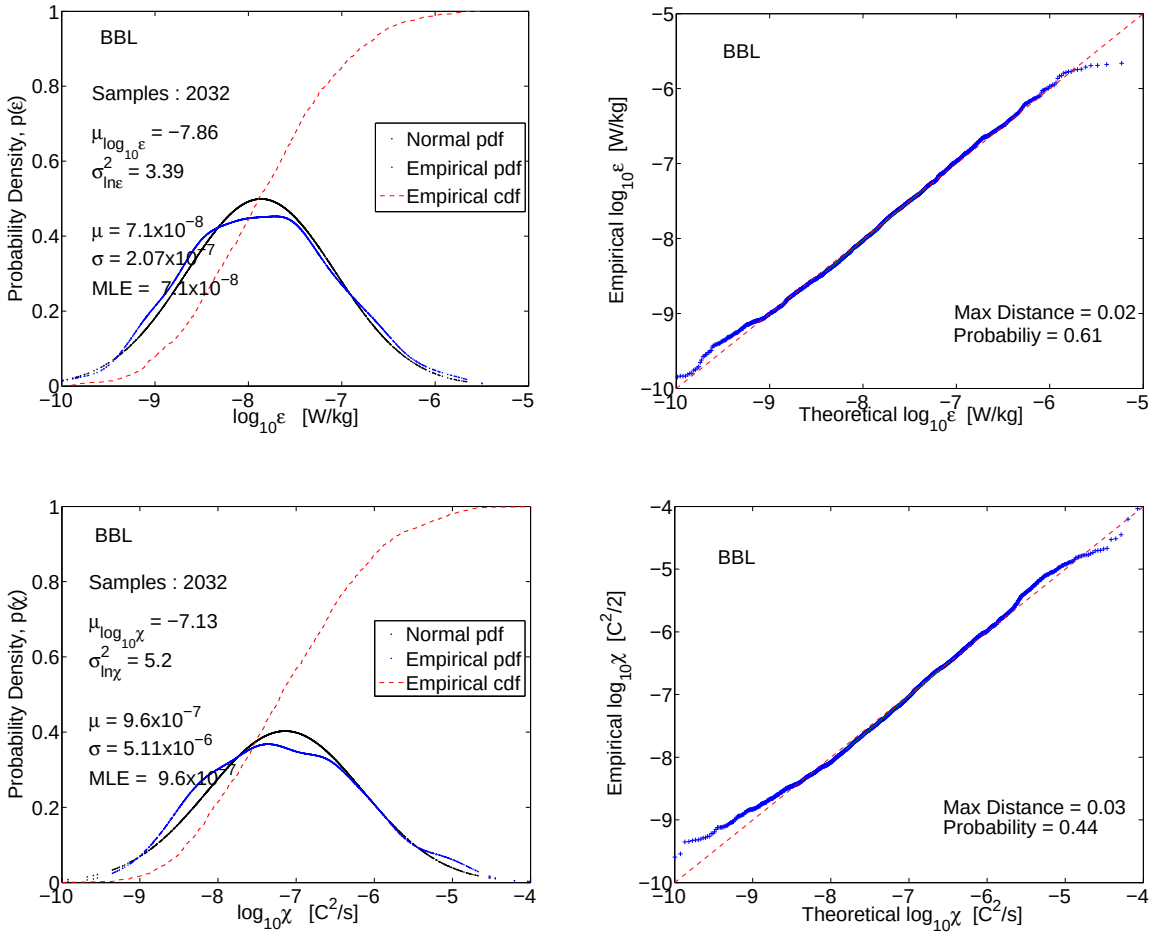

Fig. 15. PDF (left) and QQ (right) plots for $log_{10}\ \epsilon$ (top), and $log_{10}\ \chi$ (bottom) in the BBL. Day and night-time profiles are combined together. All panels have similar definitions as in Fig. 11.

B. Water Current Measurements

Current velocities of the water column were measured using the ADCP manufactured by Nortek AS. It uses the Doppler effect to measure current velocity by transmitting a short pulse of sound, listening to its echo and measuring the change in pitch of the echo. This instrument consists of a cylinder 75 mm in diameter and 561 mm long containing sensors for measuring temperature (thermistor embedded in head with an accuracy of -0.1^{o}C), compass (accuracy of 2^o), tilt (accuracy of -0.2^o) and pressure (accuracy of 0.25% of full scale per sample). The velocity range is $\pm$ 10 m/s in horizontal direction while $\pm$ 5 m/s along the beam with an accuracy of 1% of measured value $\pm$ 0.5 cm/s.

The current meter mooring was deployed for 24 hours at every station. At stations 2 and 8, the ADCP was about a meter below the surface and looking downward while at Station 5, the centermost station, we deployed the ADCP about 18 m below the surface and looking upward. At station 12, the shallowest station, we mounted the ADCP on a boogie board looking downward. Unfortunately, due to a malfunction in the signal amplifier board of the ADCP, we do not have current measurements for the whole water column and only the first two bins near to the transducer could be used (the amplitude signal for the first two bins is well above the noise level). Fig. 16 shows the magnitude and direction of the currents at station 5 from the first bin of the ADCP. From the plot, it can be observed that the current flow changed direction from northward to southward during the night, though the magnitude of current flow was relatively weak with values around 5-8 cm/sec.

Current measurements from the first bin of ADCP at Station 5 are used to force the one-dimensional model to determine the actual dynamics of mixing processes below the thermocline. At station 5, estimates of ϵ are on the order of 10^{-7} W/kg in

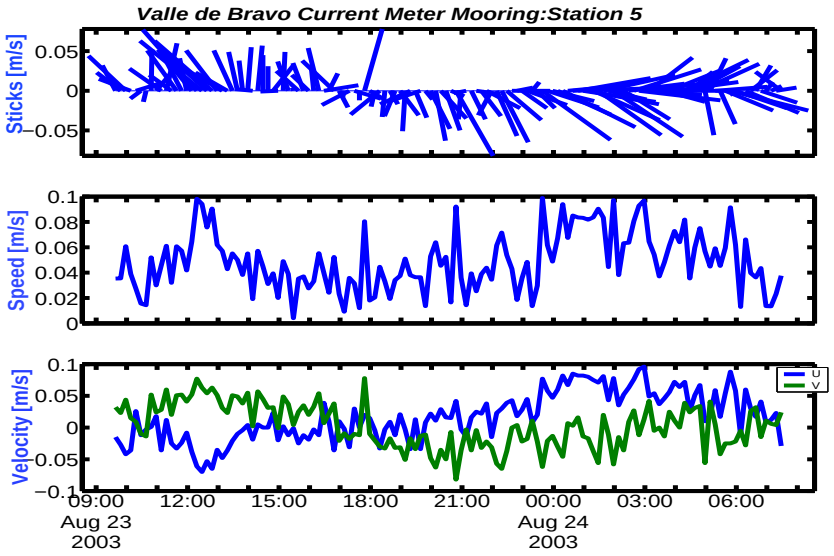

Fig. 16. Water currents measured at station 5 (30 min averages); upper panel shows the velocity sticks, middle panel shows the current speed and the lower panel shows the U (east-west, blue line) and V (north-south, green line) velocity components.

the BBL, a relatively large value, which might be a result of internal wave breaking near the bottom or due to other processes. Due to modeling requirements, in order to determine the dynamics of mixing processes below the thermocline, current measurements should be known at a point below the thermocline [57]. Hence due to the electronic malfunction described above, it would be difficult to simulate mixing processes below the thermocline at other stations where the ADCP was deployed near the surface.

C. Meteorological Measurements

Surface meteorology is essential for understanding related physical processes within the water column. For this purpose, an on-lake meteorological station continously monitored the following parameters : air temperature and humidity (CS500 - accuracy

of ± 0.6^{o}C at temperature range of 0-40^{o}C and ±3% for 10 to 90 % relative humidity range at 20^{o}C); atmospheric pressure (PTA427 Vaisala Barometer - linear accuracy of ±0.3 mb between 800-1600 mb pressure range); solar radiation (SP Lite Silicon Pyranometer - with a temperature dependence of ±0.15% per ^{o}C and a directional error of < 10% at 80^o); wind speed (03101-5 Wind Anemometer - accuracy of ±0.5 m/s) and direction (03301-5 Wind Vane - accuracy of ±5^o); and rainfall rate (TE525 Tipping Bucket Rain Gage - accuracy of 1% at 2 inch/hr or less).

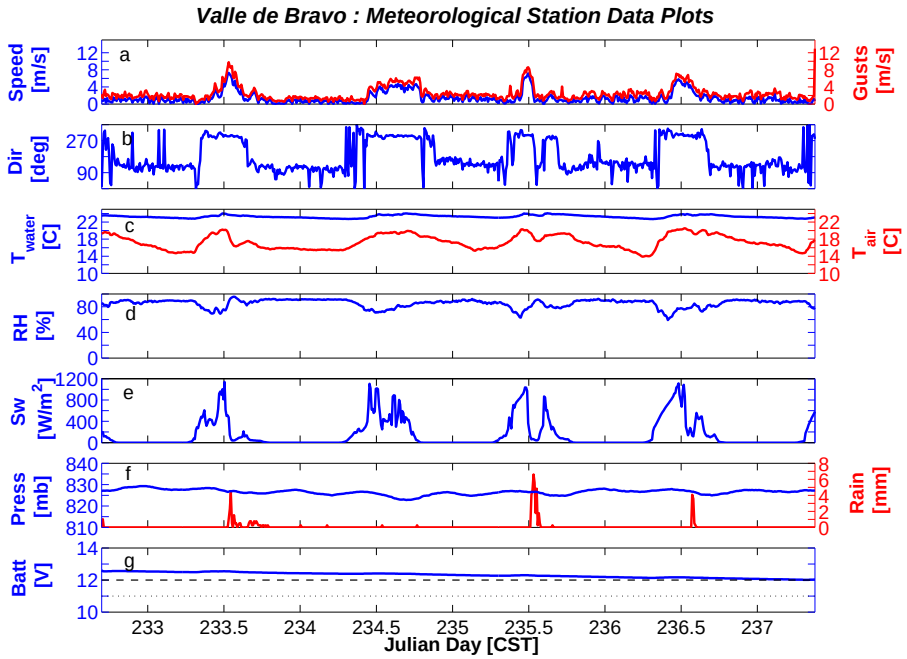

Fig. 17. Plot of meteorological quantities, (a) wind speed (blue) and wind gusts (red); (b) wind direction in degrees; (c) Air temperature (red) and water temperature (blue); (d) Relative humidity; (e) Short wave radiation; (f) Atmospheric pressure (blue) and amount of rain (red); (g) Battery voltage.

A Campbell CR10 data logger polled each sensor every 5 seconds, averaged for 10 minutes and stored the average in memory for temperature and relative humidity, pressure, wind speed and direction, solar radiation, and rainfall rate . The air-temperature sensor was inside a fan-aspirated radiation shield to minimize the effects

of solar radiation heating.

A plot of measured meteorological quantities is shown (Fig. 17). The experiment period was marked with thunderstorms with a fair amount of rain recorded on the 21st, 23rd and 24th of August, 2003 (Fig. 17(f)).

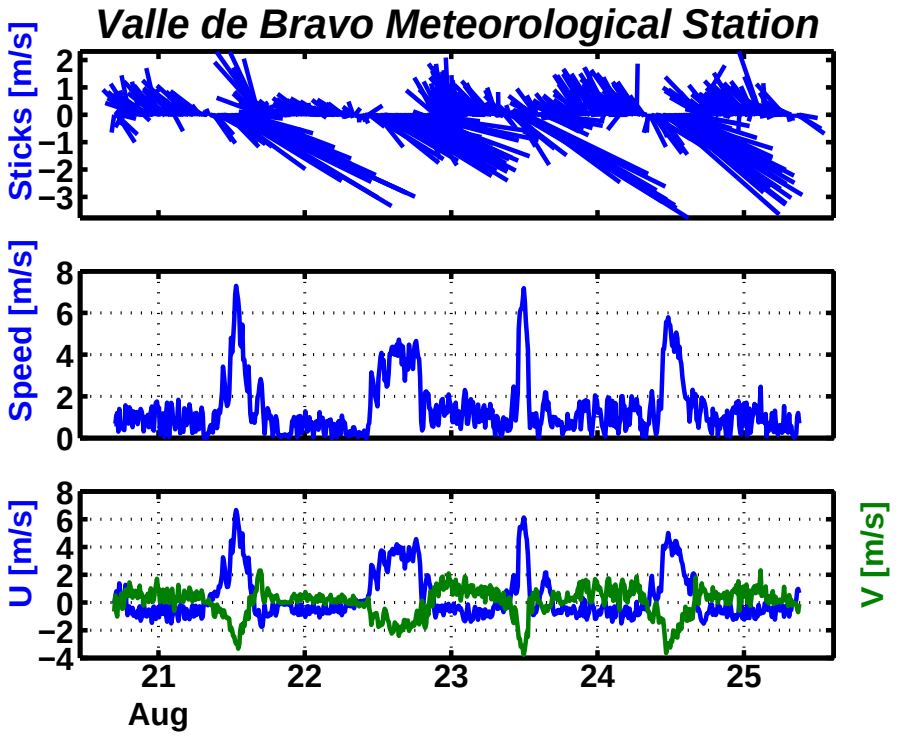

Fig. 18. Plot of wind data; top panel shows velocity sticks, middle panel - wind speed and bottom panel shows the U (east-west) and V (north-south) components of wind velocity. All times are in CST.

Throughout the duration of the experiment, surface water temperature was about $2-3^{\circ}$C warmer than the air temperature (Fig. 17(c)). The average relative humidity was observed to be between 70 - 80% (Fig. 17(d)).

Winds were fairly calm except during the four afternoons when the wind speed rose to about 5-7 m/s and the wind direction changed from north-west to south-east (Fig. 18). From Fig. 1, we can say that during this time, winds blew from the dam into the reservoir, while at other times winds were blowing in opposite direction. Hence, during this period winds were predominantly along the main axis of the reservoir.

From surface meteorology, we estimated the surface heatflux components (net short wave, net long wave, sensible and latent heat flux) using bulk formulaes. Net short wave flux into the ocean was computed following [58] from the measured solar radiation. Net long wave flux was computed using the bulk formulaes defined by [59] after applying the cloud correction [60]. Sensible and latent heat fluxes were computed using the bulk formulaes suggested by [32] and [33]. Plots of surface heat flux and wind stress are shown in the next section along with the measured SCAMP data.

D. Contour plots

In this section, plots of solar radiation, surface heat flux, wind stress and contour plots of potential temperature, χ and TKED (ϵ) for all the stations are shown. An attempt has been made to calculate salinity and potential density following the equation of state for fresh water bodies [30] and interesting features were noticed based on these parameters.

1. Station 2

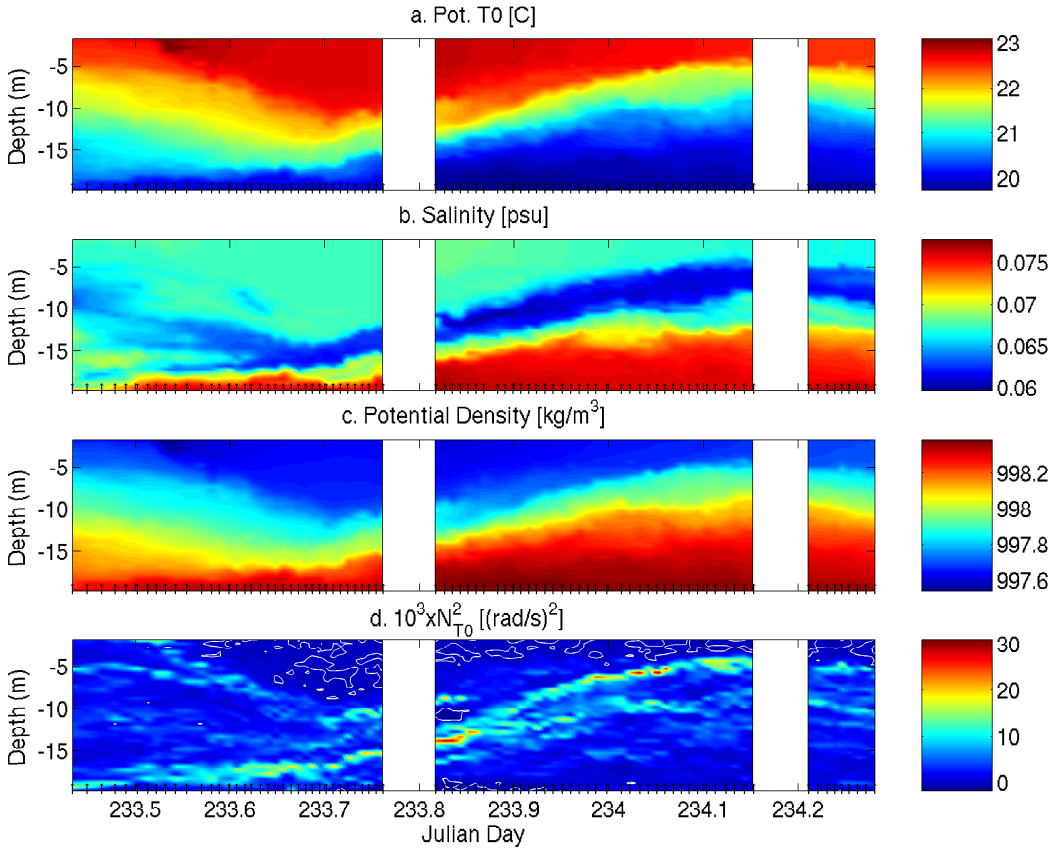

Fig. 19. Observed data from station 2; (a) Potential temperature; (b) Salinity; (c) Potential density; and (d) Buoyancy frequency squared (white contour lines represent $N^2 = 0$.

Contour plot of potential temperature (Fig. 19 (a)) reveals surface warming around noon due to increased solar radiation ($\sim 1000 W/m^2$; Fig. 20 (a)). We can also notice an internal wave of the first vertical and first horizontal mode, with a period $\sim$ 15 hours and vertical displacement $\sim$ 5m. (see Appendix C for details).

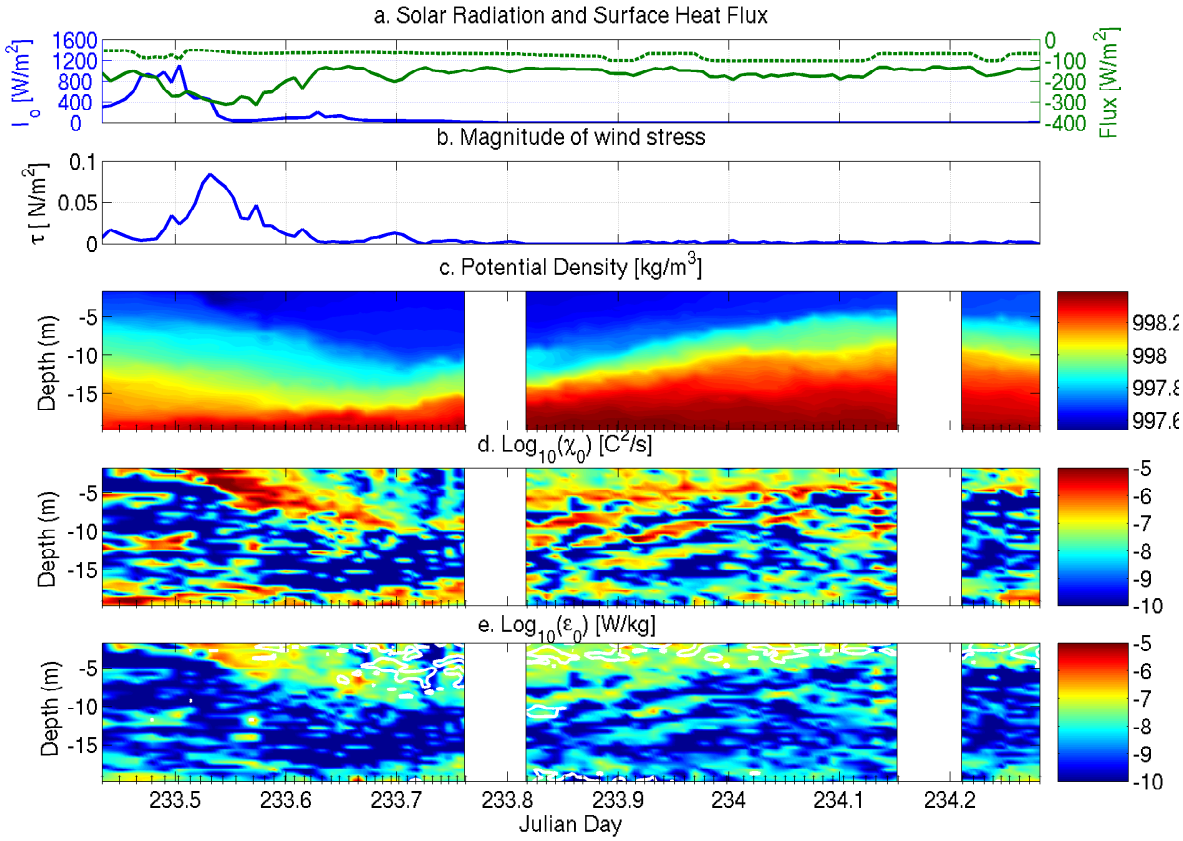

Fig. 20. Observed data from station 2; (a) Solar radiation (solid blue), net surface heat flux (solid green) and latent heat flux (dashed green); (b) Magnitude of wind stress; (c) Salinity; (d) Chi (χ) ; and (e) TKED (ϵ), overlaid white lines represent $N^2 = 0$.

Contour plot of salinity (Fig. 19 (b)) shows an interesting feature, namely, a fresh blob of water trapped around 10m depth. We might speculate that it comes either as a fresh water input from precipitation a day before or as a break-off from the internal wave. However, this fresher layer also seem to be closely related to the intermediate temperature layer.

Due to intense cloud cover later in the afternoon, net solar radiation rapidly reduced close to zero while wind stress increased to $\tau_{max} = 0.08 N/m^2$ (Fig. 20 (a) and (b)). As a result, the warm layer formed due to surface heating, was mixed with the deeper layers in the late afternoon.

This trend of mixing is very well depicted in the contour plots of χ and ϵ (Fig. 20 (d)and (e)). During daytime, strong mixing events ($\epsilon \sim 10^{-6} W/kg$) near the surface ($\sim 0 - 6$m) were mainly driven by winds (Fig. 20 (d) and (e)) while during night, convection was the major driving force in surface layer mixing. However, night time mixing was more confined to shallower layers ($\sim 0 - 3$m).

2. Station 8

This station was occupied on the second day of our sampling period and was our deepest station with depths around 30m, located right next to a dam. Winds were relatively weak ($\tau = 0.03 N/m^2$) compared to Station 2 ($\tau = 0.08 N/m^2$) resulting in weaker mixing in the surface layer (Fig. 22 (d) and (e)).

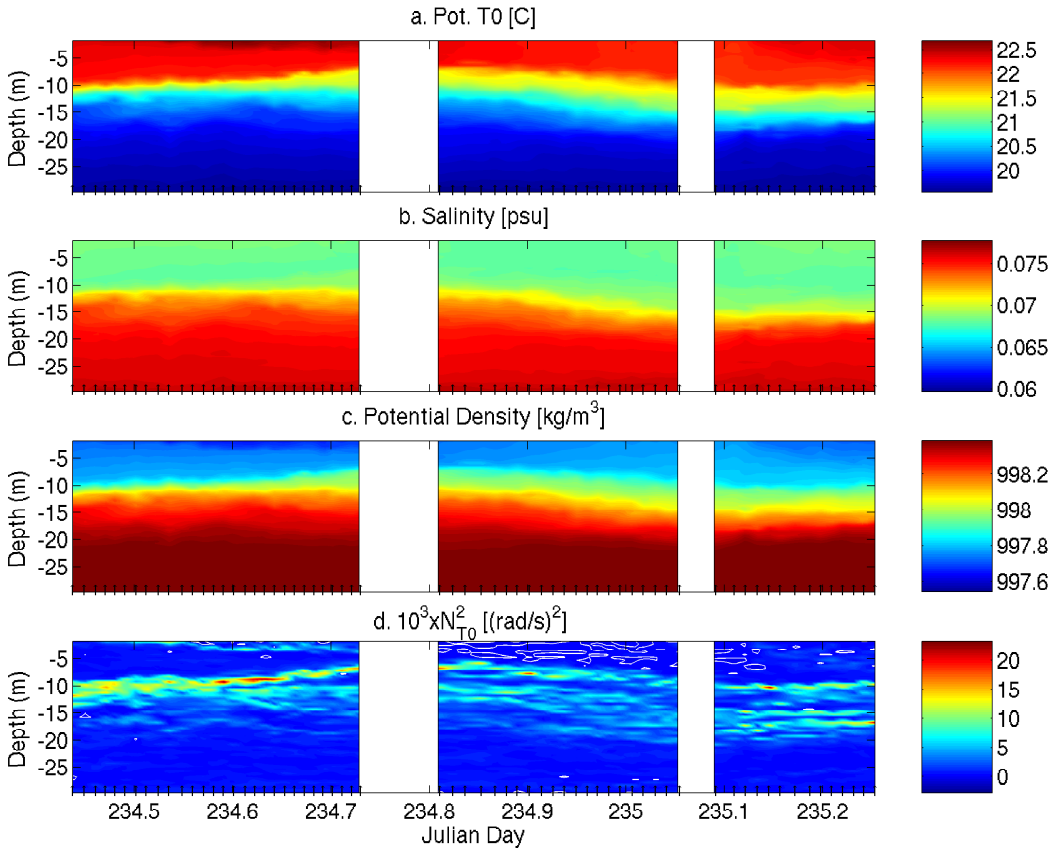

Fig. 21. Same as Fig. 19 but for station 8.

Solar radiation reached values as high as $1100 W/m^2$ and surface temperatures were $\sim 22.5^o C$ (Fig. 21 (a)) and there was no rainfall at this station. No special features were observed in the salinity structure. The water column was again stably stratified (Fig. 21 (d)) and the thermocline did not fluctuate vertically as much as it did at station 2 and was roughly between 10-12 m depth during the time of sampling.

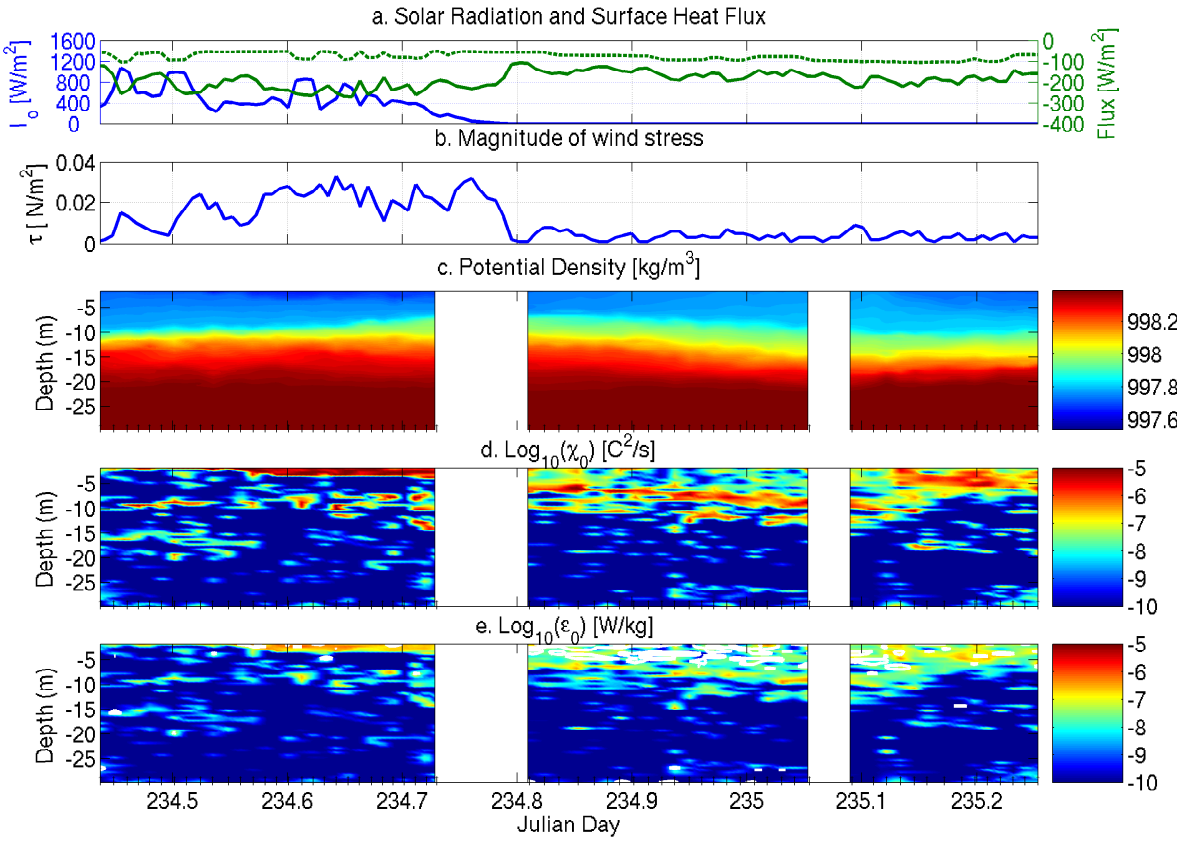

Fig. 22. Same as Fig. 20 but for station 8.

Convection was again a driving force for mixing in the surface layer during nighttime. We did not observe much of an activity in the BBL and values of both χ and ϵ were close to noise level ($\chi_{noise} = 10^{-10} C^2/s$ and $\epsilon_{noise} = 10^{-10} W/kg$).

3. Station 5

The third day of sampling was performed at this station. This is our central lake station with depths of $\sim$ 23 m. Conditions during the beginning of sampling were fairly calm and sunny (solar radiation was $\sim 1000 W/m^2$; Fig. 24 (a)) but around noon the major part of the reservoir was covered with clouds and light rain was observed.

As observed at the other stations, we had surface warming around noon but as winds increased the warmer surface waters were mixed with the deeper layers. The

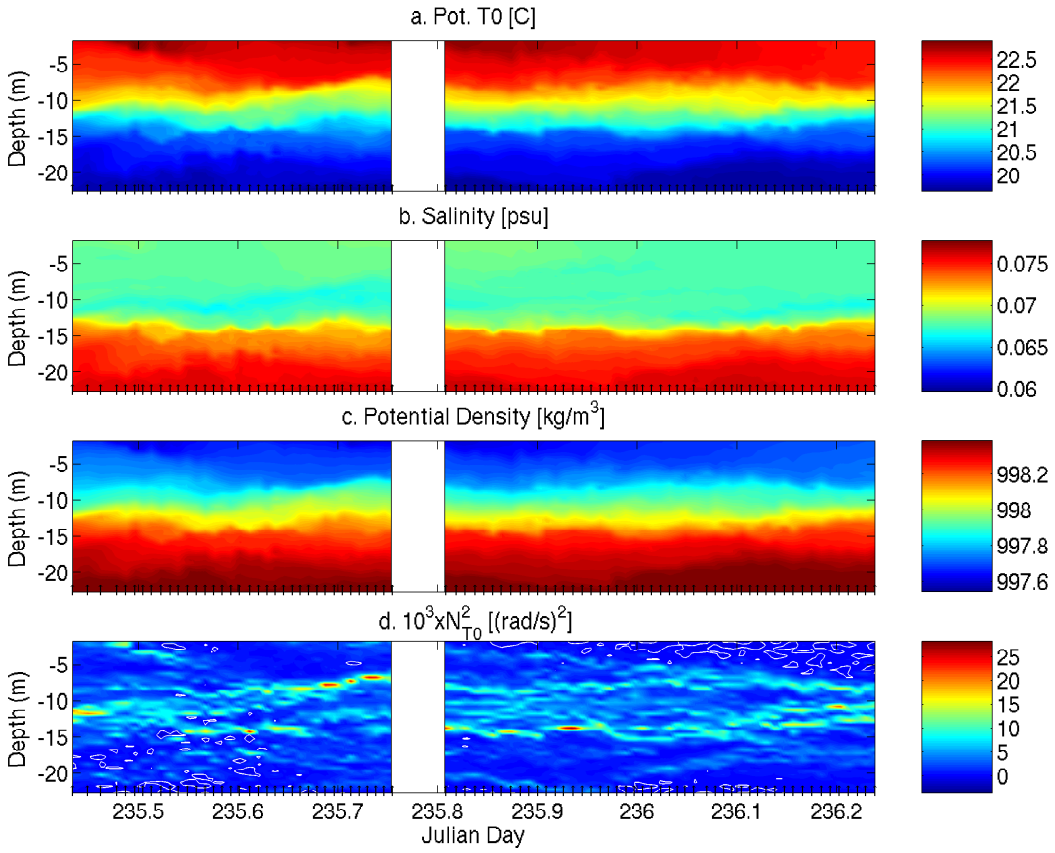

Fig. 23. Same as Fig. 19 but for station 5.

thermocline depth was fairly constant at $\sim$ 11 m throughout the sampling period at this station (Fig. 23 (a)). Water column was stably stratified with the exception in the BBL during daytime where we could see small "packets" of instability (Fig. 23 (d)). χ and ϵ plots during day-time (Fig. 24 (d) and (e)) reveal strong mixing activity in the BBL. It was found that the slopes were critical for breaking of internal waves at the bottom which might be a reason for this intense mixing (Appendix C).

4. Station 12

This was our final and shallowest sampling station ($\sim$ 12 m depth). Winds were fairly weak ($\tau = 0.05 N/m^2$) compared to a day before ($\tau = 0.08 N/m^2$) (Fig. 26 (b)) and

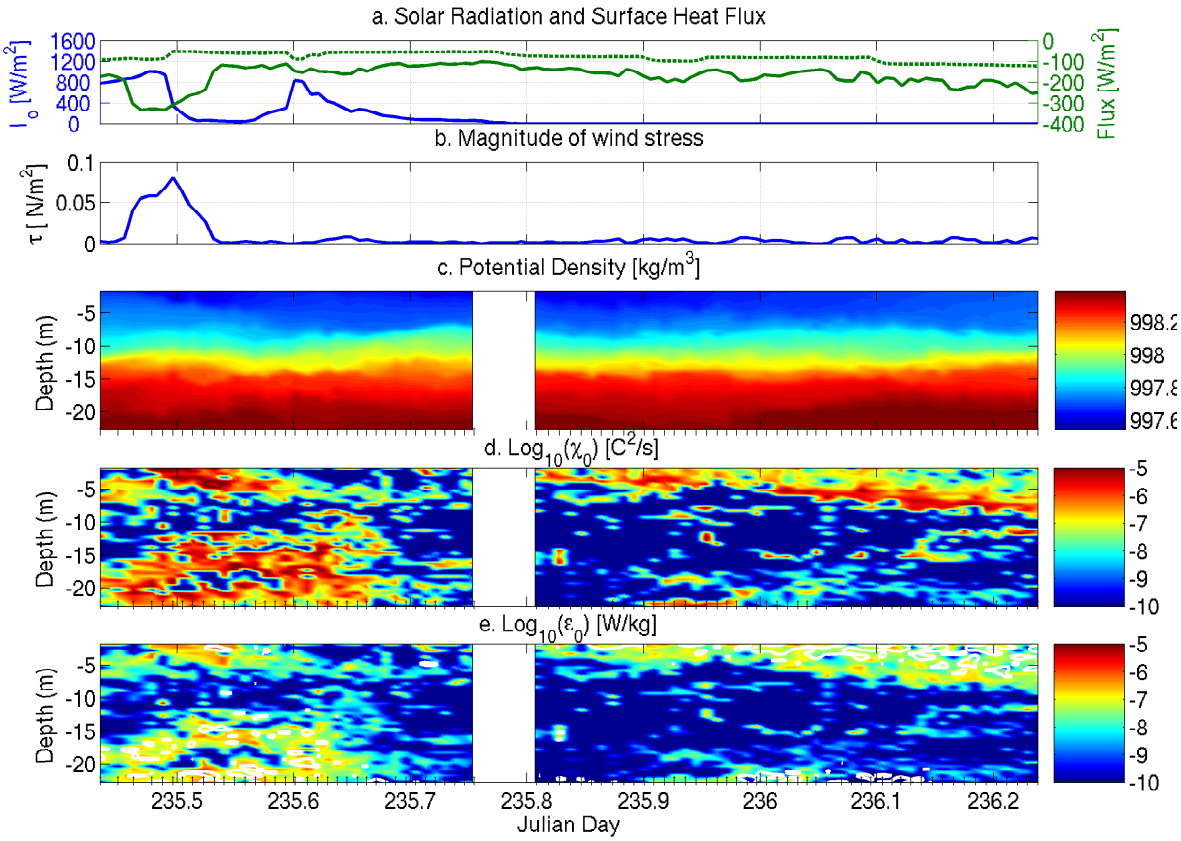

Fig. 24. Same as Fig. 20 but for station 5.

there was a slight rainfall late afternoon.

Contour plot of temperature (Fig. 25 (a)) shows higher surface temperatures around noon ($\sim 23^oC$) due to increased solar radiation ($\sim 1100 W/m^2$). An internal wave of period $\sim$ 18 hours with a vertical displacement of $\sim$ 3 m can be noticed. It was also identified as a V1H1 mode seiche (Appendix C). Salinity shows similar features with fresher water between the saltier waters in the epilimnion and hypolimnion (Fig. 25 (b)) although weaker than observed at station 2. (Epilimnion refers to the layer above the thermocline; hypolimnion is the layer below the thermocline; thermocline is referred as the metalimnion).

Due to the shallow depth at this station, thermocline was very close to the bottom late afternoon (Fig. 25 (a)) and relatively strong activity can be observed

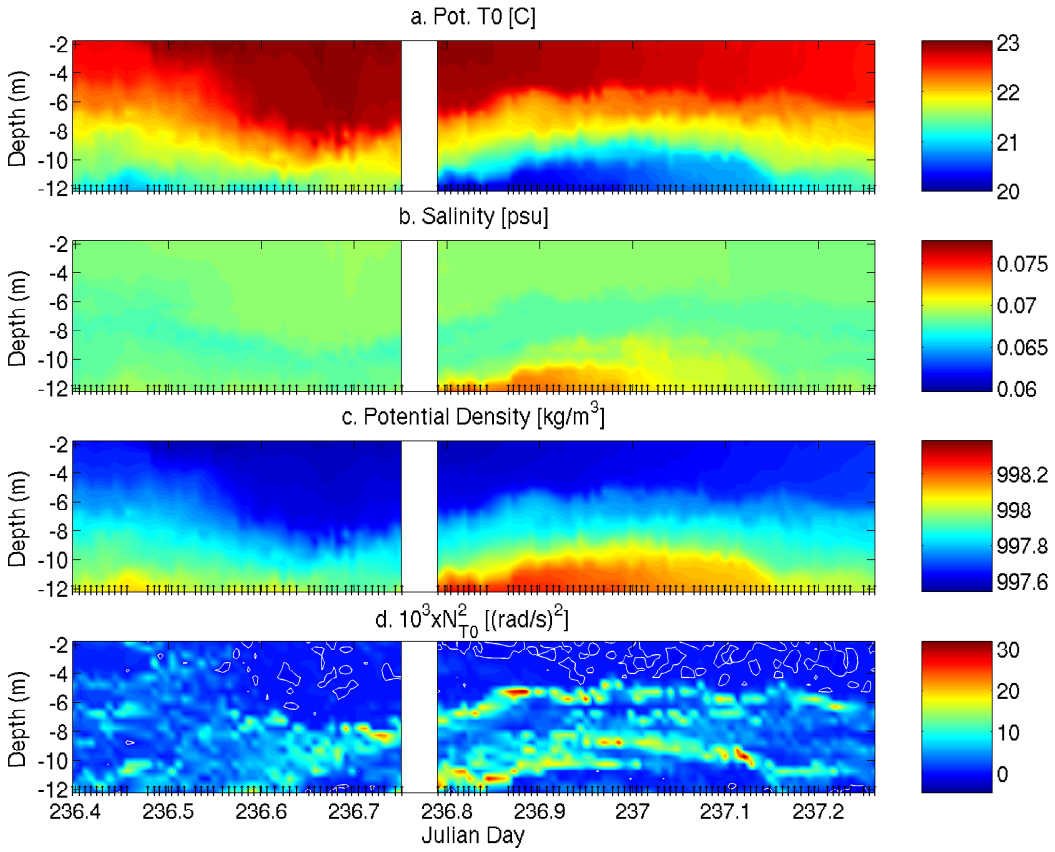

Fig. 25. Same as Fig. 19 but for station 12.

in the BBL during this time (Fig. 26 (d) and (e)). Surface layer mixing was wind forced during daytime while convection was the apparent driving force during night, a feature observed at all the stations.

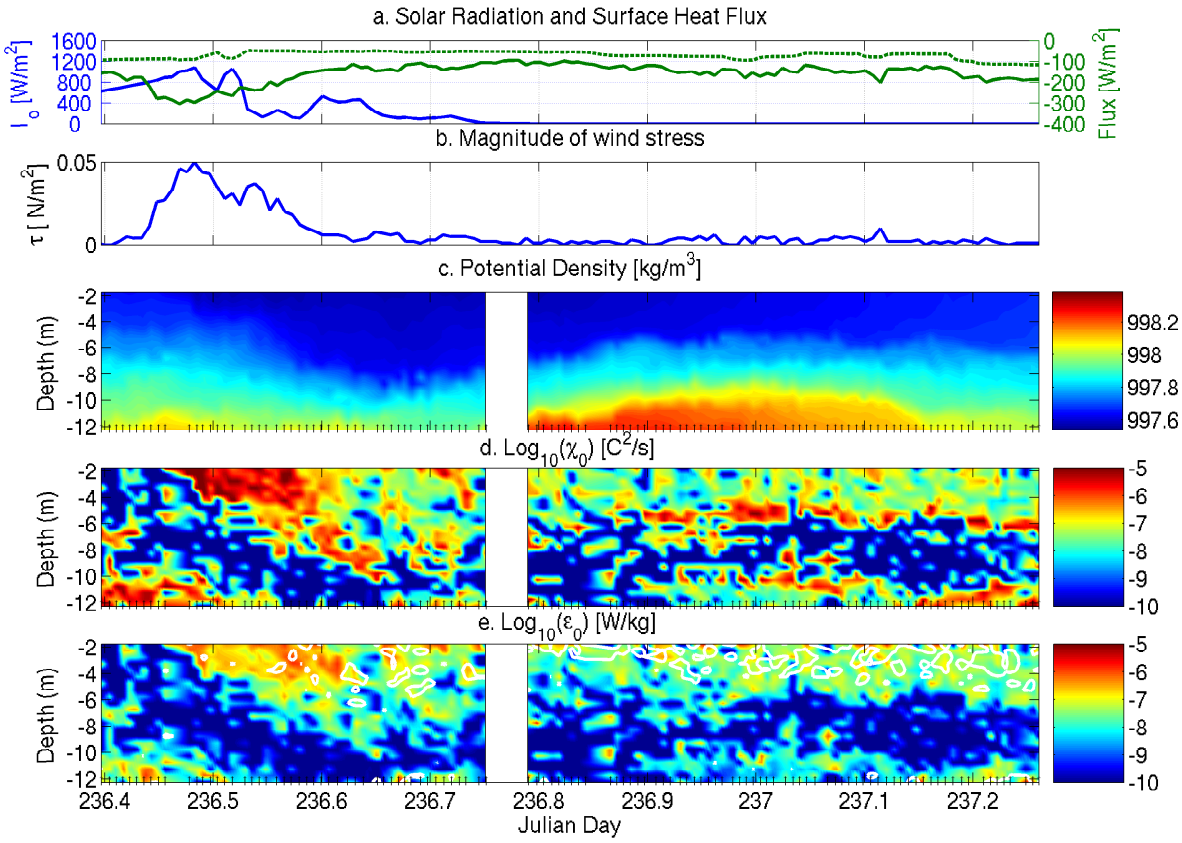

Fig. 26. Same as Fig. 20 but for station 12.

CHAPTER IV

NUMERICAL MODEL SIMULATIONS

Numerical Modelling has served as an important tool for prediction and understanding of complex processes such as turbulence in the water column. For this study, we used the state-of-the-art one dimensional General Ocean Turbulence Model (GOTM). One dimensional water-column models that simulate physical and bio-geochemical processes along a vertical axis are popular in the ocean-modelling community. Compared to three dimensional models, they are much less complex and the computational time is minimal. Most one dimensional models are based on the hydrostatic assumption (i.e. vertical scales are much smaller than horizontal scales) and they also assume that the horizontal variations are almost negligible. But in some models, we can also add horizontal gradients. Although, most of these models exclude mesoscale features, upwelling and downwelling, and various coastal effects, they have been used for decades for studies in various marine and aquatic environments (e.g. [13]; [19]; [21]; [61]).

GOTM is a one-dimensional water column model which simulates small-scale turbulence and vertical mixing. In this model, Reynolds-averaging is used and the hydrostatic and Boussinesq approximations are made. The user can choose turbulence closure schemes such as the two equation k-ϵ and Mellor-Yamada level 2.5 (MY) model to parameterize turbulence. It was shown in various studies (e.g. [19]; [23]; [24]; [25]; [62]) that the k-ϵ turbulence closure scheme does, in general, better than other parameterization schemes. This study uses the k-ϵ turbulence closure scheme for all simulations and a direct comparison to the observations is made.

As mentioned in previous chapters, we focus on two turbulence quantities, the temperature dissipation rate (χ) and TKED (ϵ). Next we describe the main model equations and the boundary conditions. Numerical simulations of VB reservoir per-

formed for the four sampling stations, and comparison to observations are shown in subsequent sections. In the last section, we present statistics and scaling of χ and ϵ and discuss possible relationship between the turbulent quantities, wind stress, surface buoyancy flux, and internal waves.

A. Model Equations

The mathematical model, on which the numerical modelling is based, consists of six dynamical equations for the two velocity components u (eastward) and v (northward). the potential temperature T, the salinity S, TKE k, and TKED ϵ [34]:

$$\partial_t u - \partial_z((\nu_t + \nu)\partial_z u) - fv = -\frac{\partial_x P}{\rho_0} \tag{4.1}$$

$$\partial_t v - \partial_z((\nu_t + \nu)\partial_z v) + fu = -\frac{\partial_y P}{\rho_0} \tag{4.2}$$

$$\partial_t T - \partial_z((\nu_t^{'} + \nu^{'})\partial_z T) = I(z) \tag{4.3}$$

$$\partial_t S - \partial_z((\nu_t^{'} + \nu^{''})\partial_z S) = \tau_S^{-1}(S_d - S) \tag{4.4}$$

$$\partial_t k - \partial_z(\nu_k \partial_z k) = P + B - \epsilon \tag{4.5}$$

$$\partial_t \epsilon - \partial_z(\nu_\epsilon \partial_z \epsilon) = \frac{\epsilon}{k}(c_{\epsilon 1} P + c_{\epsilon 3} B - c_{\epsilon 2}\epsilon) \tag{4.6}$$

with gravitational acceleration g, reference density ρ_0 and the Coriolis frequency $f = 2\omega sin(\phi)$ with the earth's angular velocity ω and latitude ϕ. In the potential temperature Eq. (4.3), $I(z)$ is the solar radiation in the water column (generally calculated from the given surface condition as an exponentially decreasing function with depth). In the salinity Eq. (4.4), τ_S is the relaxation time (defined as the time after which model is nudged back to the observed values) and S_d is a prescribed salinity. The molecular diffusivities for momentum, temperature and salinity are given by ν, $\nu^{'}$ and $\nu^{''}$. respectively.

In addition to above system of equations, the UNESCO equation of state (e.g. [63]) for calculating potential density as functions of T, S and hydrostatic pressure is applied, and the horizontal pressure gradients $\partial_x P$ and $\partial_y P$ are prescribed or parameterized.

The use of k-ϵ turbulence model (Eqns. (4.5) and (4.6)) serves two purposes : 1) reproducing observations of turbulence dissipation rate and 2) calculating eddy viscosity ν_t for momentum and eddy diffusivity ν_t' for tracers by making use of the Kolmogorov-Prandtl relation :

$$\nu_t = c_\mu \sqrt{k} L; \quad \nu_t^{'} = c_\mu^{'} \sqrt{k} L \tag{4.7}$$

where c_μ and $c_\mu^{'}$ are non-dimensional stability functions recently suggested in [64]. In TKE equation (Eq. (4.5)), P and B are the shear production and buoyancy production terms, respectively, given as :

$$P = \nu_t \left((\partial_z u)^2 + (\partial_z v)^2 \right); \quad B = -\nu_t^{'} N^2 \tag{4.8}$$

where N is defined in Eq. (2.8).

The eddy diffusivities ν_k and ν_ϵ (Eqns. (4.5) and (4.6)) are modelled as $\nu_k = \nu_t$ and $\nu_\epsilon = \nu_t / \sigma_\epsilon$ and the turbulent length scale described above (Eq. (4.7)) is related to k and ϵ by

$$L = \left(c_\mu^0 \right)^3 . \frac{k^{3/2}}{\epsilon} \tag{4.9}$$

Table V summarizes the constants used in $k - \epsilon$ turbulence model.

The boundary conditions for L at the bottom and at the surface are given by

$$L = \kappa (z_0 + \tilde{z}) \tag{4.10}$$

Table V. Constants for k-ϵ model.

$c_{\epsilon 1}$	$c_{\epsilon 2}$	$c_{\epsilon 3}(B<0)$	$c_{\epsilon 3}(B>0)$	σ_ϵ	c_μ^0
1.44	1.92	-0.4	1.0	1.08	0.5562

where $\kappa = 0.4$ is the von K*árm*á*n* constant, $\tilde{z}$ is the distance from the bottom or surface, and z_0 is the bottom or surface roughness length.

The boundary conditions for k at the bottom and sruface (no flux condition) are

$$\nu_k \partial_z \kappa = 0 \tag{4.11}$$

By combining Eqs. (4.9) and (4.10), a Dirichlet boundary condition for ϵ can be derived as

$$\epsilon = \left(c_\mu^0\right)^3 \frac{\kappa^{3/2}}{\kappa(\tilde{z}+z_0)} \tag{4.12}$$

By differentiating above equation with respect to $\tilde{z}$, an equivalent flux boundary condition (von Neumann boundary condition) for ϵ can be derived

$$\frac{\nu_t}{\sigma_\epsilon}\partial_{\tilde{z}}\epsilon = -\left(c_\mu^0\right)^3 \frac{\nu_t}{\sigma_\epsilon}\frac{\kappa^{3/2}}{\kappa(\tilde{z}+z_0)^2} \tag{4.13}$$

B. Model Simulations

In this section, we discuss the model simulations for our four stations (Fig. 1). Comparisons to corresponding observations are shown in the following sections. We have maintained consistency in keeping all modelling parameters the same for all the stations. These parameters are discussed briefly in the next section.

1. Model Parameters

GOTM provides a number of options for simulating turbulence and takes different forcings such as surface heat flux; incoming solar radiation; momentum fluxes (i.e. the wind stress components τ_x and τ_y); vertical temperature and salinity profiles; internal and external pressure gradients; and current velocity profiles into account. This study uses the k-ϵ parameterization scheme for all simulations with a vertical and temporal resolution of $\triangle$z=0.25m and $\triangle$t=20 s, respectively. Salinity was not used in the simulations because gradients in salinity were relatively small for this fresh water body. Due to uncertainties in estimated heat fluxes and the role of horizontal heat advection, a nudging of simulated temperature towards observations was necessary and was done at 1 hour intervals. The model can also be forced with surface slopes (right hand side terms of Eqns. (4.1) and (4.2)) which may be computed from a times series of current velocities at a single point in the water column [57]. This type of barotropic (tidal) forcing allows in simulating BBL turbulence in a better way. In [57], it is explained that the current measurements can be taken at any point in the water column however in order to minimize the effect of near-surface processes such as surface wave-breaking or convection, the current meters should be positioned below the mixed layer. For this study, we placed the ADCP below the mixed layer only at Station 5 (central) while at other stations, the ADCP was mounted near-surface. Unfortunately as mentioned earlier, we had problems with the signal-amplifier board of the ADCP and only the first two bins could be used. Hence, the model does not perform well near-bottom at those stations where the ADCP was mounted near-surface.

2. Station 2

Station 2 was the first and southern most sampling station (Fig. 1). Nearly continous 24-hour sampling was performed to obtain microstructure profiles with the SCAMP. We also deployed a surface current meter mooring with the ADCP looking downwards. Surface meteorology was obtained from the station that was setup about 3 km of station 2.

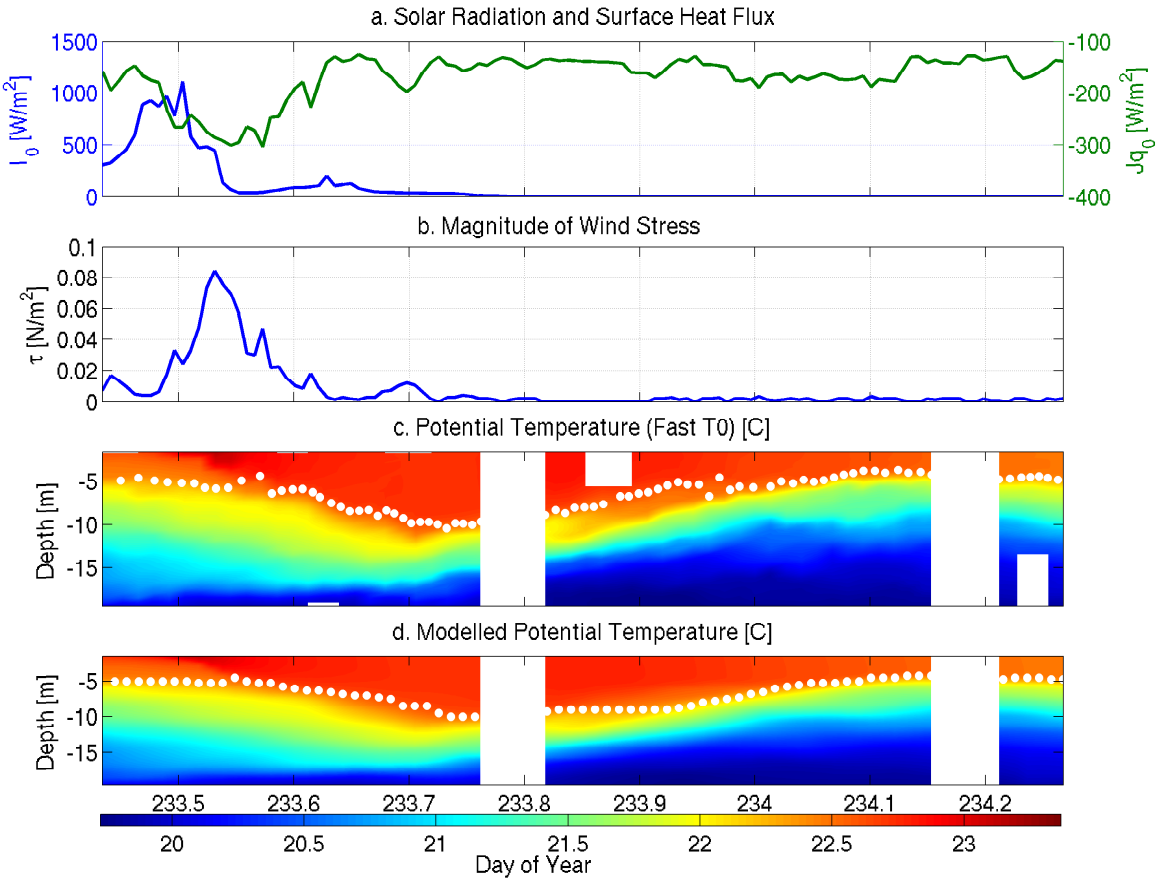

Fig. 27. Meteorological quantities with observed and simulated potential temperature for station 2; (a) solar radiation (blue) and surface heat flux (green); (b) magnitude of wind stress; (c) observed potential temperature and (d) simulated potential temperature; white circles represent the mixed layer depth obtained visually for every profile.

The model was forced with the meteorological observations and vertical profiles

of temperature were supplied as an input. An initial 6 hour spin-up was used and the model was nudged back to the observations every hour.

In Fig. 27(a), a plot of a time series of solar radiation (blue) and surface heat flux (green) is shown. Solar radiation is the net radiation penetrating into the water column while the surface heat flux consists of three components : latent heat flux, sensible heat flux and net long wave radiation. The sign convention used here is positive for fluxes entering the water and negative for fluxes leaving the water. There was an increase in net solar radiation as the day progressed but early afternoon it decreased to nearly zero due to intense cloud cover and rain activity (Fig. 27). The maximum flux into the water column was $\sim 1100 W/m^2$ while the maximum heat loss was $\sim 300 W/m^2$. During night, there was an average heat loss rate of $\sim 150 W/m^2$ to the atmosphere.

The maximum wind stress observed was $\sim 0.08 N/m^2$ (Fig. 27(b)) corresponding to wind speeds of $\sim 8 m/s$. Wind mainly came from north (Fig. 18) and it can be noticed that at the time solar radiation decreased, wind speed rose reaching a maximum at the time solar radiation almost fell to zero. After this winds also decreased and reduced to near zero with afternoon thunderstorms.

The color scheme is the same for observed and simulated temperatures, with red representing warmer temperatures and blue cooler temperatures (Fig. 27). It can be noticed that with an increase in solar radiation during the first few hours of sampling, the observed surface water temperature increased and with an increase in wind speeds, the warmer water was soon mixed into the deeper layers, consequently deeping the mixed-layer.

Both the observed and simulated χ plots show how the warmer layer, formed due to increased surface heating, is mixed and eventually dissipated into the deeper layers (Fig. 28). The intensity of χ decreases with depth, with values as high as

$10^{-5}C^2/s$ near the surface and $\sim 10^{-9}C^2/s$ below the thermocline. Apparently, the thermocline acts as a barrier for dissipation to reach the deeper layers and just below the thermocline we can find lower values of χ (fairly close to noise level, $\chi_{noise} = 10^{-10}C^2/s$).

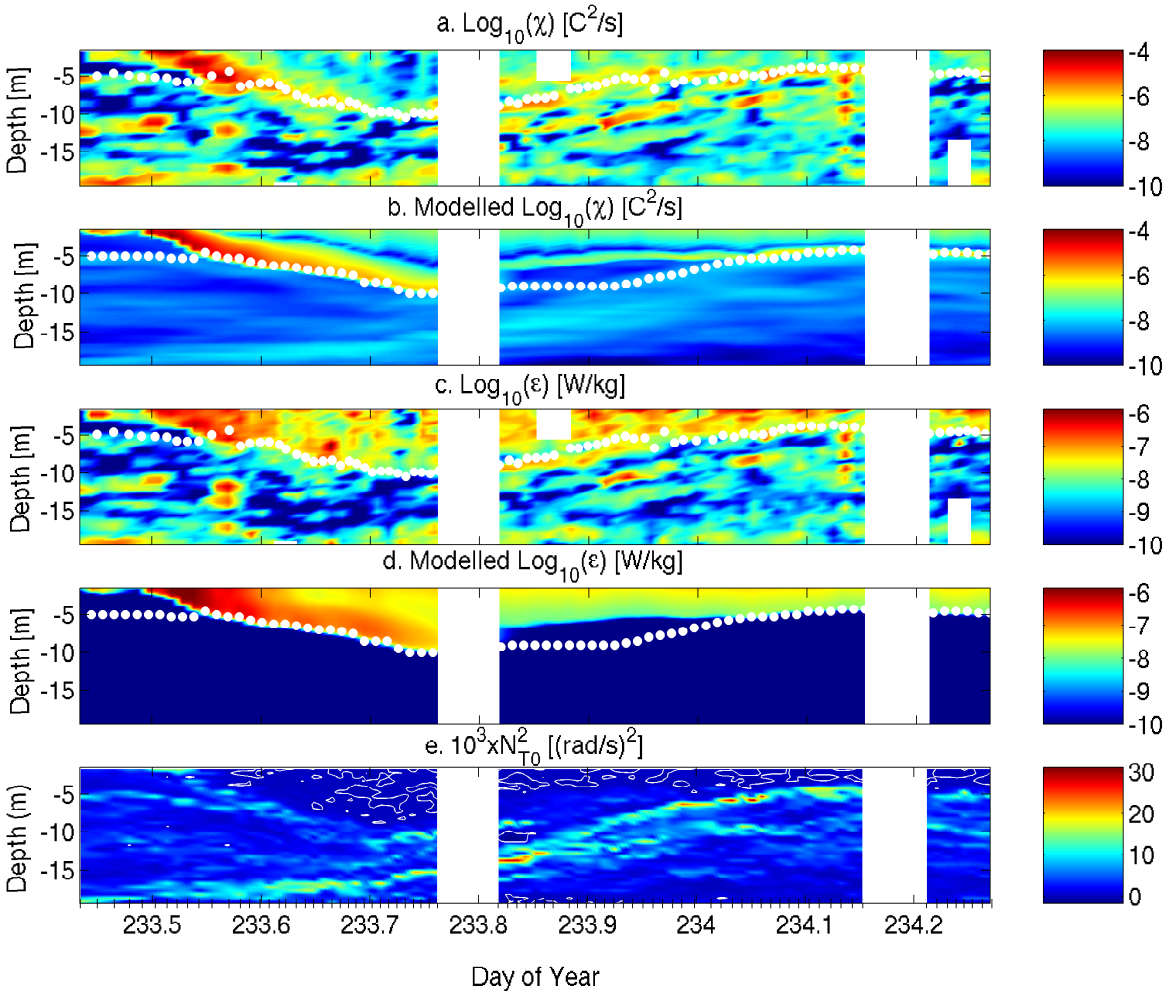

Fig. 28. Contour plots of observed and modelled turbulence dissipation rates for station 2; (a) observed χ; (b) simulated χ; (c) observed ϵ; (d) simulated ϵ; and (e) Buoyancy frequency squared, white contours represent $N^2 = 0$. White circles represent mixed layer depth.

When winds were strong, we observed relatively high values of ϵ ($\sim 10^{-7} - 10^{-6}W/kg$ which corresponds to intense mixing) near the surface and continues to

the mixed layer with decreasing values with increasing depth (Fig. 28(c) and (d)). During night, convection was the main driving force for mixing in the surface and mixed layers. The model simulations slightly underestimated the intensity of mixing near-surface during night but they follow the same trend as that of the observations. Below the thermocline, model simulations do not perform well because the surface forcing is no longer effective in producing turbulence.

3. Station 8

On the second day of the experiment period, we sampled at station 8 (Fig. 1) which was since it is the deepest station ($\sim$ 30 m) and is situated next to a dam controlling the major source of inflow into the reservoir.

The modelling parameters for this station are the same as those for station 2. The conditions were fairly calm and sunny at this station with maximum solar radiation reaching $\sim 1000 W/m^2$ (Fig. 29(a)). Winds were relatively weak during the day ($\tau_{max} \sim 0.03 N/m^2$) compared to the winds ($\tau_{max} \sim 0.08 N/m^2$) a day before and during night, conditions were calm.

Similar to what was observed at station 2, there were relatively strong near-surface mixing events throughout the sampling period (Fig. 30). However, beneath the thermocline and in the BBL, we did not observe significant mixing as we did at station 2. During the day, wind was the main driving force resulting into higher levels of turbulence ($\chi \sim 10^{-5} C^2/s$ and $\epsilon \sim 10^{-6} W/kg$) while during nighttime, convection was the apparent driving force near-surface. Both χ and ϵ decreased with increasing depth and falling rapidly just below the thermocline to $\chi \sim 10^{-9} C^2/s$ and $\epsilon \sim 10^{-10} W/kg$. Comparison between observations and model results reveal that the basic dynamics are qualitatively as well as quantitatively reproduced by the model. The major differences occur in the vicinity of the thermocline where the numerical

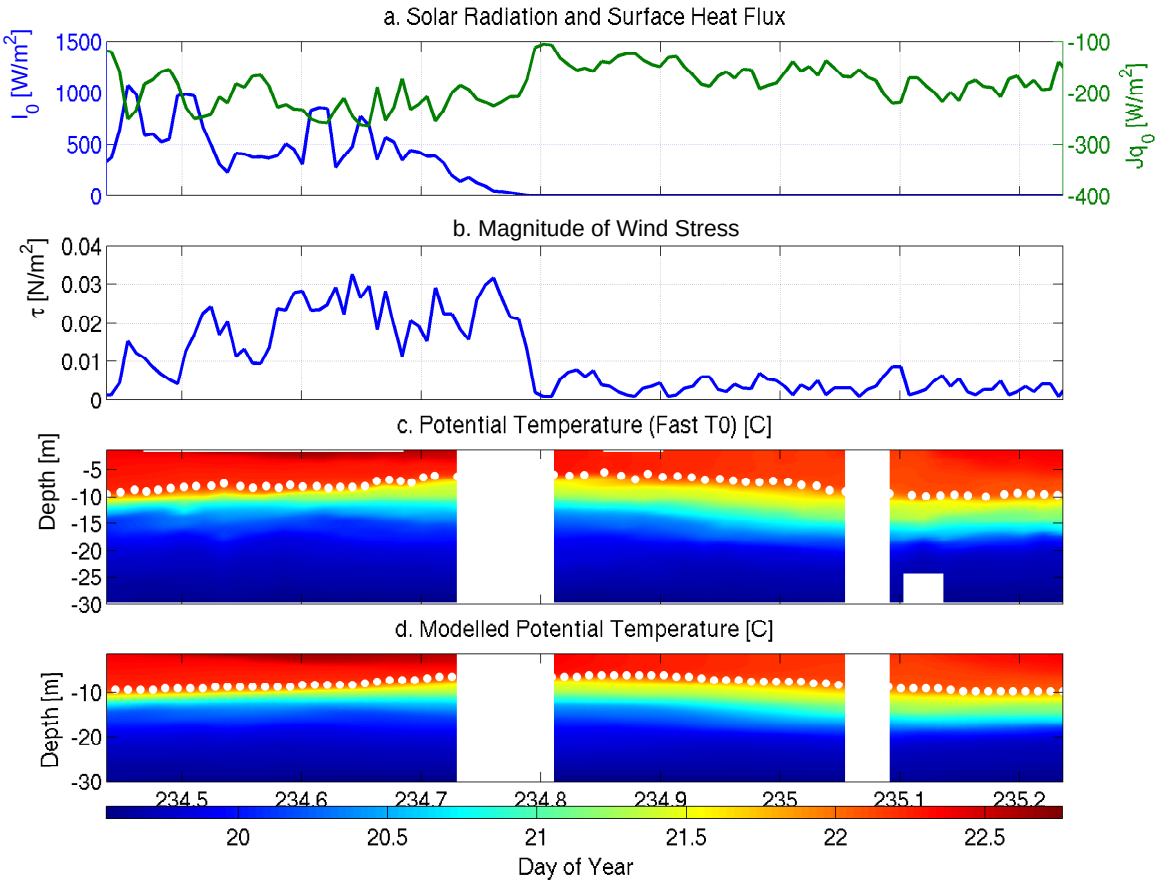

Fig. 29. Same as Fig. 27 but for station 8.

model cannot resolve the complex dynamics of decaying turbulence.

4. Station 5

The central station (station 5; depth $\sim$ 25 m; Fig. 1) was occupied during the third day of the experiment. At this station we deployed the ADCP below the thermocline ($\sim$ 6.5 m above the bottom) and looking upwards. The conditions during the beginning of sampling were fairly calm and sunny (solar radiation reaching $\sim 1000 W/m^2$ during this time; Fig. 31), however, around noon most of the reservoir was covered with clouds and light rain was observed. With increased cloud cover, solar radiation decreased but at the same time winds increased (Fig. 31(b)) and reached a maximum

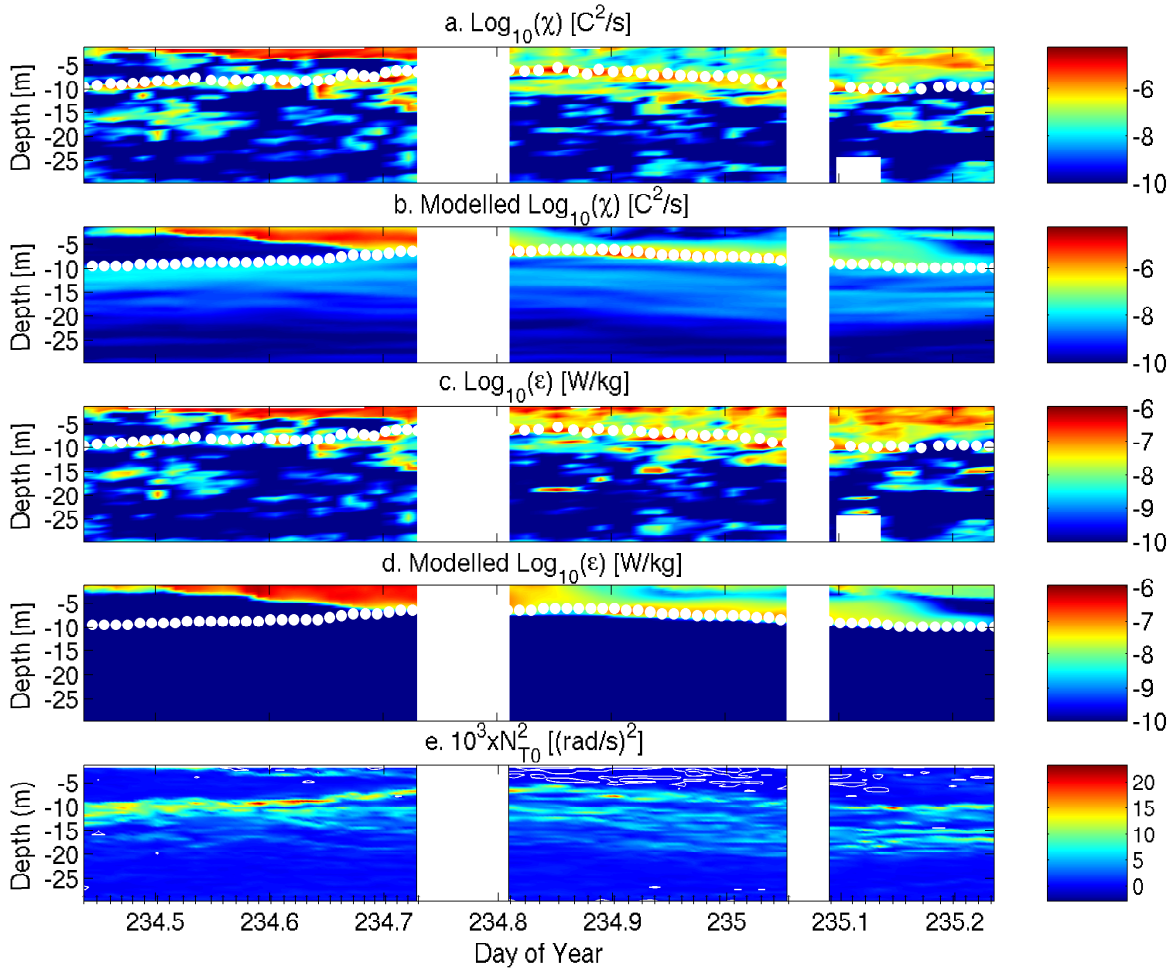

Fig. 30. Same as Fig. 28 but for station 8.

of $\sim 0.08 N/m^2$ around noon. Conditions were calm and sunny again after a couple of hours of light rainfall.

The model parameters were kept the same as before with the exception of inclusion of current velocities at a point below the thermocline. These measurements were used as a forcing input to simulate turbulent mixing processes below the thermocline and in the BBL (Fig. 16).

The water column was weakly stratified with surface temperatures $\sim 22.5^{o}C$ while near-bottom temperatures were $\sim 20^{o}C$ (Fig. 31(c)). The thermocline depth

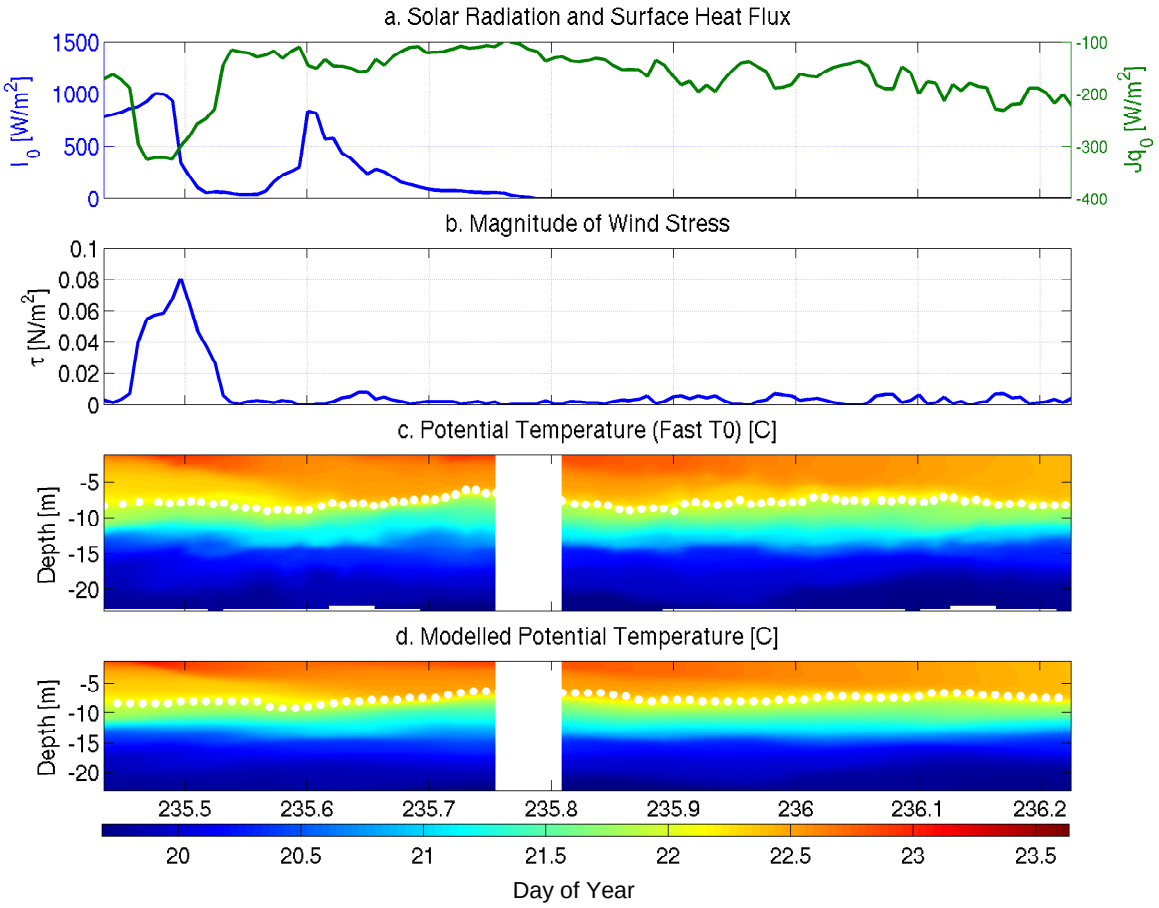

Fig. 31. Same as Fig. 27 but for station 5.

($\sim 8m$) was fairly constant throughout the sampling period.

We can notice some strong mixing near-bottom during daytime sampling (Fig. 32), the exact cause for this intense mixing might be increased shear and/or breaking of internal-waves. Internal wave-breaking seems consistent with the fact that during the first day of sampling, we observed an internal wave of period $\sim$ 15 hours and also, bottom slopes were critical for breaking of internal waves (Appendix C). From wind data (Fig. 18), it is apparent that winds blew mainly along the major axis of the reservoir and were cyclic : every morning winds increased and later in the afternoon there were almost no winds. These type of wind patterns have been shown to set up an internal wave [65]. Inclusion of current velocities in the model reveal intense

mixing events in the BBL during both day and night times (Fig. 32(b) and (d)). During night, observations do not show intense mixing events in the BBL, however we do see scattered "packets" of high values following the same trend as that of model simulations (Fig. 32(a) and (c)). Near-surface model simulations do a nice job in capturing major features and follow the same trend as that of the observations.

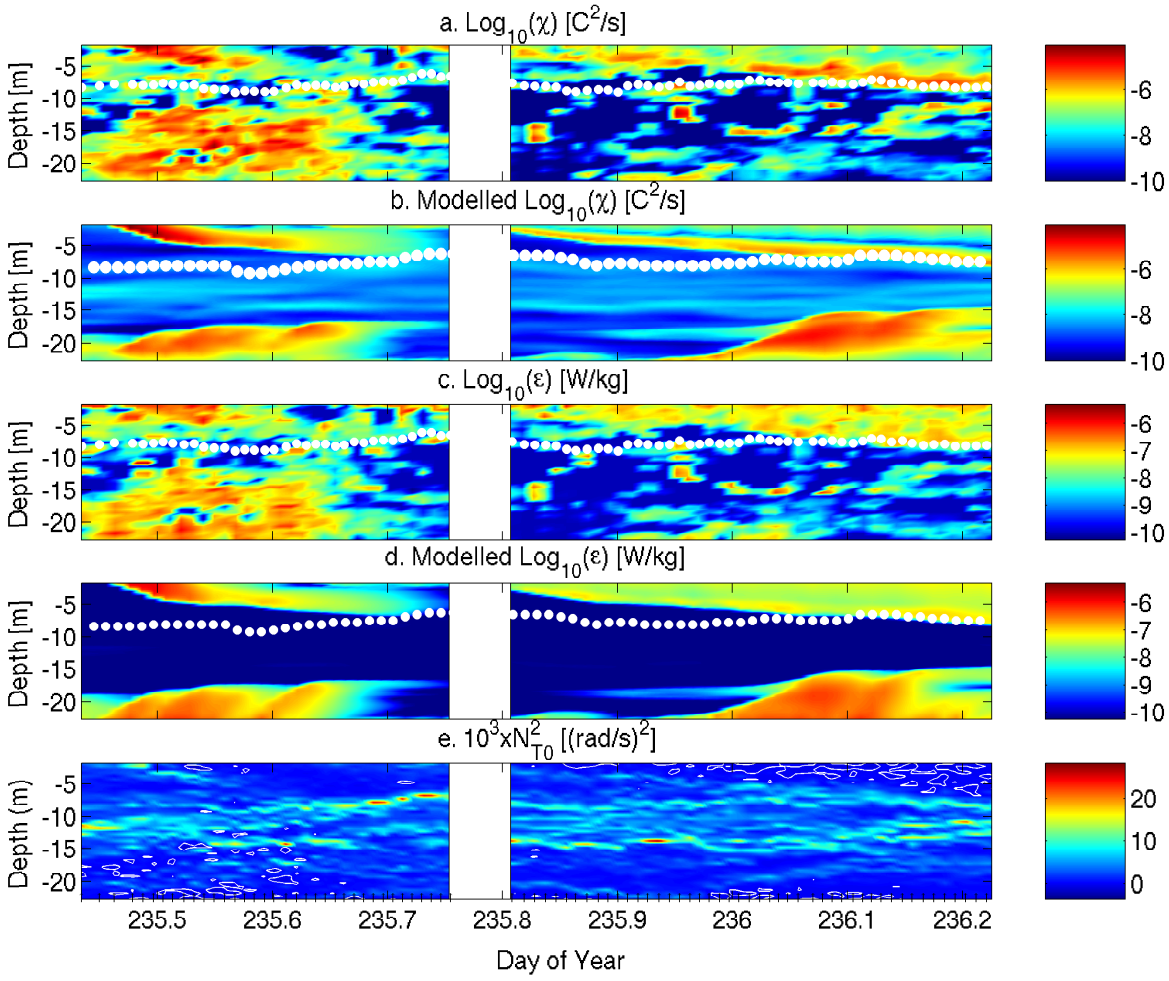

Fig. 32. Same as Fig. 28 but for station 5.

5. Station 12

We sampled at this station (the shallowest with a depth of $\sim$ 12 m) on the last day of the experiment period. The experiment period was marked with light winds ($\tau \sim 0.05 N/m^2$, Fig. 33(b)) and a few clouds. Solar radiation reached values of $\sim 1000 W/m^2$ just before noon and surface waters warmed upto $\sim 23^oC$ (Fig. 33). Along with solar radiation, wind speed also increased resulting in mixing of the warmer surface layer with deeper layers.

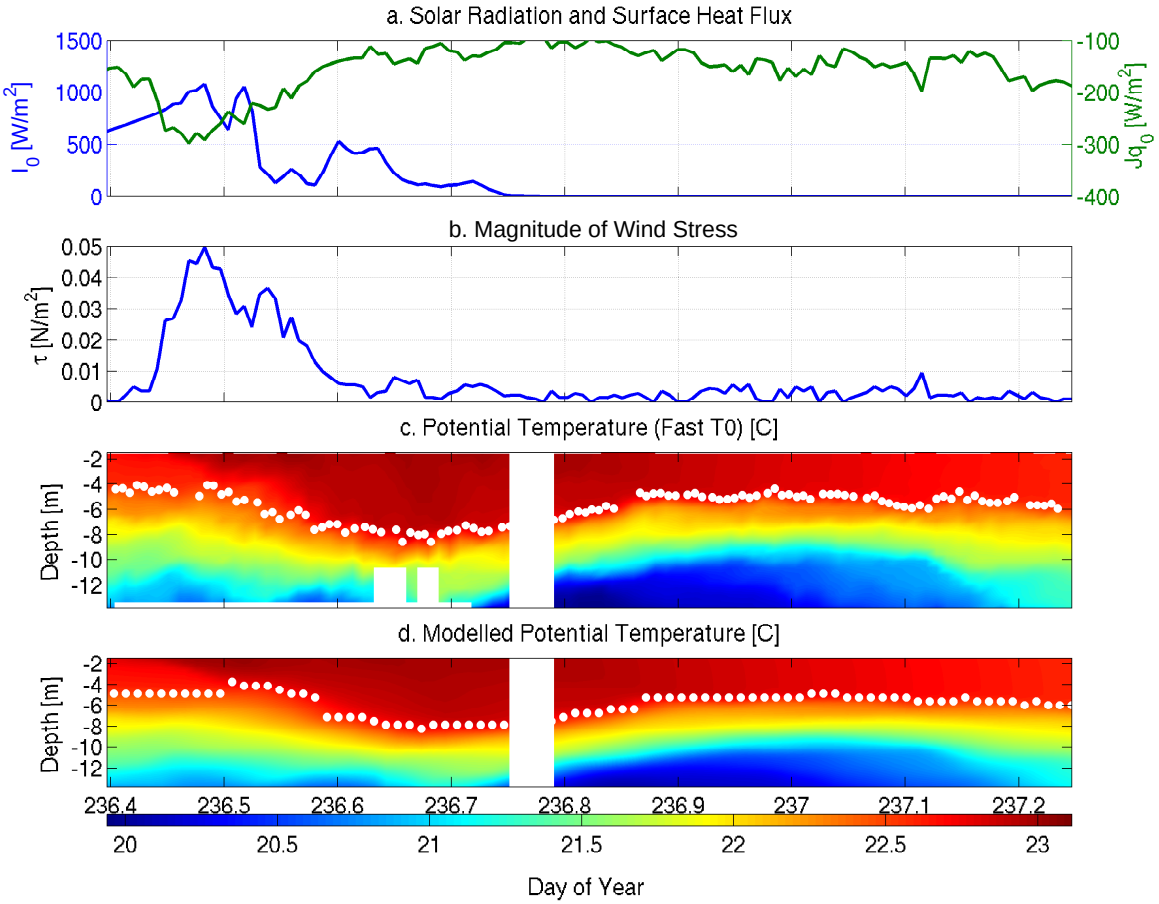

Fig. 33. Same as Fig. 27 but for station 12.

Model parameters were kept same as those for simulations of stations 2 and 8. The thermocline was close to the bottom and fluctuated between 8-11 m throughout

the duration of the sampling period. We again observed an internal wave, having a V1H1 mode (Appendix C), of period roughly 18 hours throughout the sampling period.

As observed at other stations, we again had strong mixing events near-surface during daytime resulting from the strong wind events (Fig. 34). We can see several strong mixing events in the BBL with values of $\chi \sim 10^{-5} C^2/s$ and $\epsilon \sim 10^{-6} W/kg$ (Fig. 34(a) and (c)).

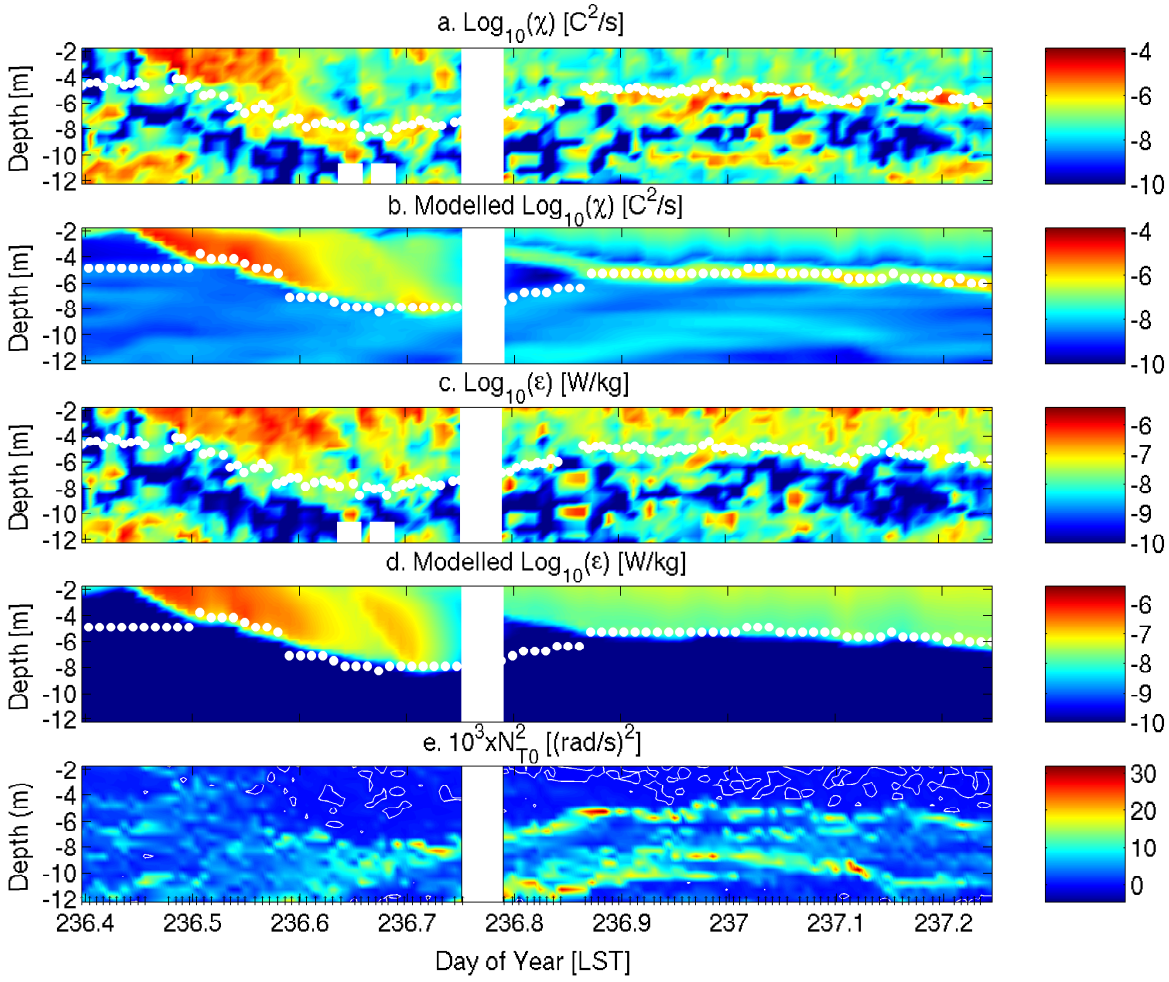

Fig. 34. Same as Fig. 28 but for station 12.

This was probably due to internal wave breaking at the bottom as the slopes

estimated for internal wave breaking were critical. Modelled χ (Fig. 34(b)) and ϵ (Fig. 34(d)) do not show such features due to absence of current measurements at a point below the thermocline. However, near-surface model simulations show a very good agreement to the observations with values ranging from 10^{-5} to $10^{-9}C^2/s$ for χ and from 10^{-6} to $10^{-10}W/kg$ for ϵ.

6. Vertical Eddy Diffusivity

One of the important characteristics of turbulent motion is its ability to transport or mix momentum, kinetic energy, and scalars such as heat, salt and moisture. The rates of transfer and mixing are parameterized by a turbulent or eddy diffusivity which is analogous to the molecular diffusivity [66].

Estimates of vertical eddy diffusivities, K_ρ, were done for observations using Eq.(2.8) and compared to those obtained from model simulations. K_ρ for the observed data was plotted together with the simulated K_ρ for all the stations during day and night (Fig. 35). Earlier, we have shown that the SL mixing was driven by winds during the day, while at night, the SL mixing was convectively driven. Thus, to estimate rates of vertical transport within the SL, observed and simulated K_ρ were plotted against scaled depth, z/D, where D is the mixed layer depth. In general, both observed and simulated values followed the same trend, decreasing with depth from $\sim 10^{-2}m^2/s$ near the surface to $\sim 10^{-4}m^2/s$ in the vicinity of the thermocline. Since the model could not resolve BBL mixing at stations 2, 8 and 12, plots of vertical eddy diffusivities were restricted to mixed layer depth for a fair comparison with the observations (Fig. 35).

However, at station 5, the model resolved BBL mixing since it was forced by current measurements near the bottom and hence simulated K_ρ was plotted for the whole water column and compared with that obtained from the observations (Fig. 36).

Table VI. Averaged $log_{10}(K_\rho)$ for day and night within the SL for all the stations. Numbers in parentheses represent 95% confidence intervals calculated from bootstrap method.

Station		Day	Night
2	Obs	$-2.73(-3.25, -2.18)$	$-2.92(-3.42, -2.34)$
	Model	$-3.34(-3.63, -2.99)$	$-2.72(-3.16, -2.1)$
5	Obs	$-3.68(-4.22, -3.15)$	$-3.11(-3.64, -2.62)$
	Model	$-4.56(-5.14, -4.02)$	$-3.39(-3.95, -2.75)$
8	Obs	$-3.69(-3.99, -3.41)$	$-2.97(-3.36, -2.6)$
	Model	$-4.84(-5.5, -4.12)$	$-3.83(-4.01, -3.66)$
12	Obs	$-2.71(-2.93, -2.45)$	$-2.47(-2.82, -2.16)$
	Model	$-3.61(-3.86, -3.32)$	$-2.53(-2.88, -2.08)$
Mean	Obs	$-3.29(-3.53, -3.01)$	$-3.15(-3.45, -2.84)$
	Model	$-4.33(-4.66, -3.98)$	$-3.40(-3.91, -2.86)$

Modelled K_ρ in the BBL compared well to the calculated K_ρ from the observations with values as high as $\sim 10^{-3} m^2/s$.

Table VI summarizes the averaged values during day and night within the SL for all the stations.

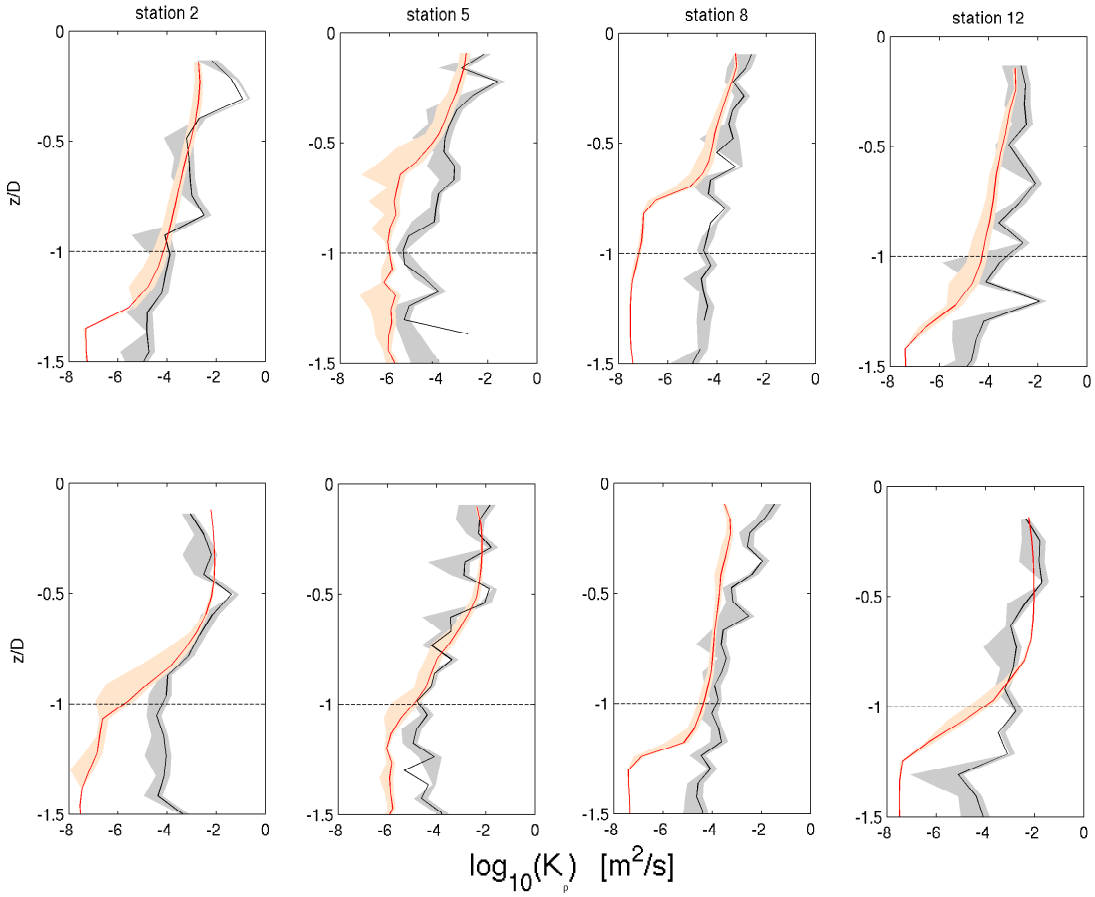

Fig. 35. Averaged eddy diffusivity ($log_{10}(K_\rho)$) for day (top panels) and night (bottom panels) estimated for station 2, station 5, station 8 and station 12. Black curve represents mean of the observed $log_{10}(K_\rho)$; red curve represents mean of the modelled $log_{10}(K_\rho)$; shaded regions represent 95% confidence limits calculated using the bootstrap method.

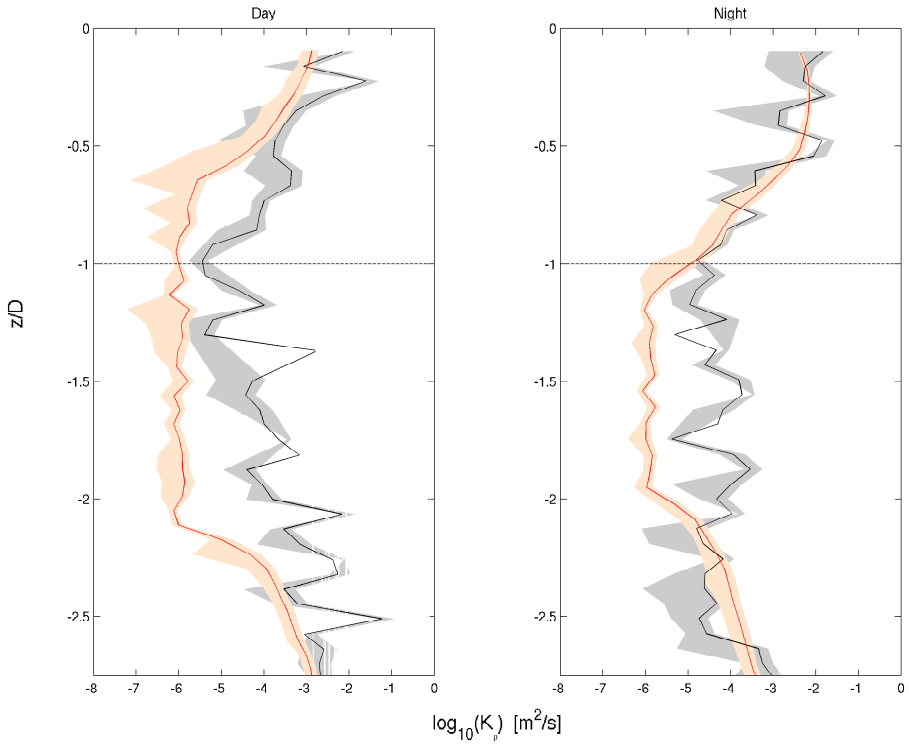

Fig. 36. Same as Fig. 35 but only for station 5.

7. Similarity Scaling of χ and ϵ

Scaling of χ and ϵ was done in order to understand their possible relationship with wind stress and surface buoyancy flux (e.g. [35]; [36]; [37]). Similar to the atmospheric boundary layer (ABL), the oceanic boundary layer (OBL) is also directly affected by wind stress and buoyancy flux at the surface. The ABL develops vertically by the action of wind stress and heat flux at the surface and the turbulent structure within the boundary layer is mainly controlled by four variables : the heat flux at the surface, J_q^o; the wind stress at the surface, τ; the distance above the surface, z; and the buoyancy of heated air, g/T where g is the acceleration due to gravity. [5] characterized the use of these four variables to normalize boundary layer measurements as similarity scaling.

A second length scale, the Monin-Obukhov length, is defined as the distance above the surface where the wind stress and buoyancy flux are equally effective at producing turbulence.

$$L = -\frac{u_*^3}{\kappa J_b^0} \tag{4.14}$$

where u_* is the surface friction velocity, $u_* \equiv \sqrt{\tau/\rho}$; κ is the von Kármán constant, $\kappa = 0.4$; J_b^0 is the surface buoyancy flux. L is used to separate two asymptotic regimes: when $z/-L \ll 1$, wind stress dominates the production of turbulence; when $z/-L \gg 1$, buoyancy controls production.

The scaling procedure is to nondimensionalize boundary layer parameters using the similarity variables, e.g., dimensionless temperature is T/T_*. T_* is defined in Table VII which shows various similarity variables pertinent during day-time and night-time. In this study, similarity scaling is applied to both χ and ϵ using both observed and simulated values.

Table VII. Similarity variables for day and night.

Characteristic	Day	Night
Velocity	$u_* = \left(\frac{\tau_0}{\rho}\right)^{1/2}$	$w_* = (DJ_b^0)^{1/3}$
Temperature	$T_* = \frac{J_q^0}{c_p \rho u_*}$	$\theta_* = \frac{J_q^0}{c_p \rho w_*}$
ϵ	$\epsilon_* = \frac{u_*^3}{\kappa z}$	$\epsilon_* = J_b^0$
χ	$\chi_* = \frac{u_* T_*^2}{z}$	$\chi_* = \frac{w_* \theta_*^2}{D}$

During daytime, the scaling is applied only when winds were significantly strong and J_q^o was roughly constant and negative; while during night, it is applied to times when buoyancy flux was roughly constant and positive [37]. [36] argued that this similarity is valid only for the mixed layer and should not be expected to work when z/D exceeds unity (D is the mixed layer depth).

Fig. 37 shows similarity scaling for χ and ϵ during day and night times, combining the data from all the stations. Both χ and ϵ were scaled using the similarity variables defined in Table VII. During daytime, 90 profiles were depth-averaged using a vertical bin size of 0.1 m and 95% confidence intervals of the mean were determined using the Bootstrap method [67]. A total of 182 profiles were averaged using the same technique during the nighttime.

The horizontal dashed line in all the panels represent mixed-layer depth while the vertical dashed line in panels (b), (c), (e) and (f) represents either $\chi/\chi_* = 1$ or $\epsilon/\epsilon_* = 1$, defining the boundary where production terms are exactly balanced by the dissipation terms. In general, simulated and observed quantities follow a similar trend during both day and night.

Wind stress scaling of ϵ (day-time) works well in the mixed layer ($z/D < -1$; Fig. 37(b)) with values decreasing with increasing depth. Significant deviations are observed below the mixed layer as the surface forcing no longer plays a role in driv-

ing mixing. During night, convection scaling of ϵ works well for observed data but modelled values are almost an order of magnitude smaller than expected (Fig. 37(e)). This is consistent with the explanation that model slightly underestimates turbulence during night near the surface.

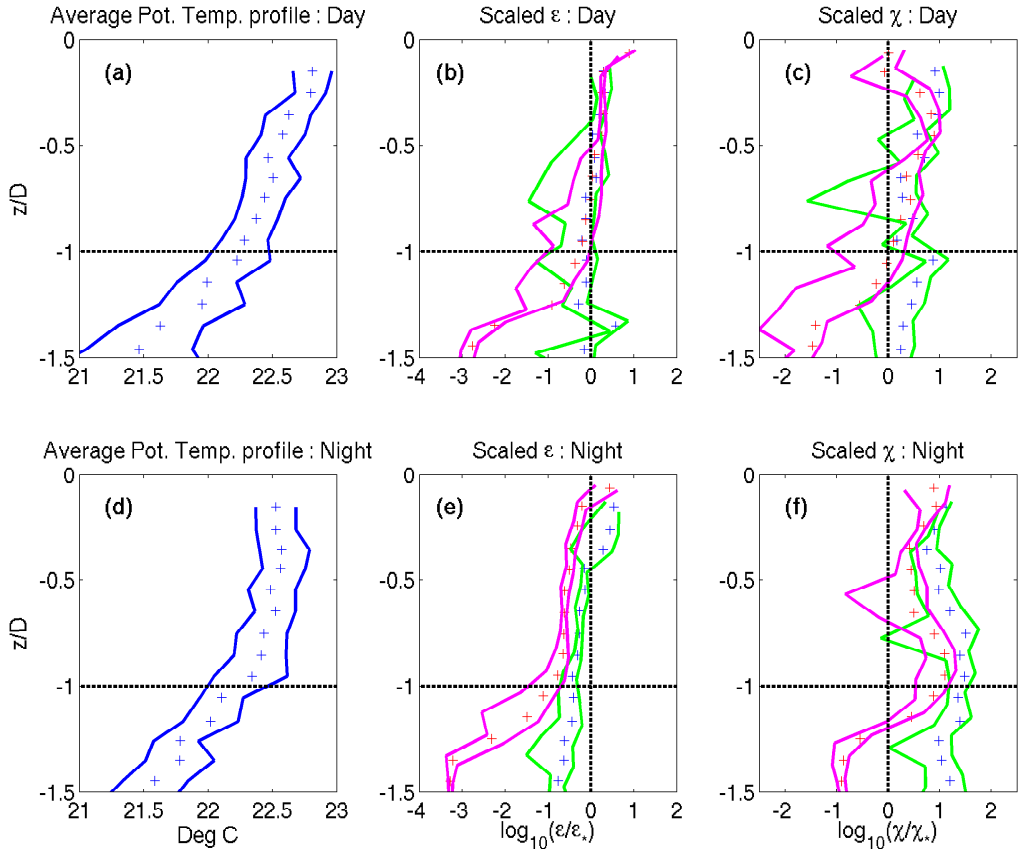

Fig. 37. Similarity scaling of χ and ϵ during day (top) and night (top) times. Panels (a) and (d) show averaged potential temperature during day and night, respectively; (b) and (e) show scaled ϵ during day and night, respectively; (c) and (f) show scaled χ during day and night, respectively; + signs represent mean values; green and magenta lines represent observed and simulated parameters with 95% confidence level determined using the Bootstrap method.

Wind stress scaling is less successful with χ (Fig. 37(c)). Nevertheless, it can be seen that $log_{10}(\chi/\chi_*) \sim 0$ within $-0.5 < z/D < -1$. Convection scaling of χ (Fig. 37(f)) shows estimates almost an order of magnitude higher than expected,

assuming this scaling is applicable, for both observed and modelled values. But, it can be seen that the scaled values for both observed and modelled χ follow the same trend.

We have summarised the averaged values during day and night-times in Table VIII. During the day, we averaged ϵ/ϵ_* over the depth range $-D < z < 0$ while during night, averaging was performed within $-D < z < 2L$ (e.g. [35]); for both observed and modelled data. During the day, the observed and the modelled ϵ/ϵ_* values were close to unity. During night, the modelled values do not relate well to the observed because the model underestimated ϵ values during nighttime. Numbers in parentheses are 95% confidence intervals of the mean determined using the bootstrap method [67].

Table VIII. Averaged values for day and night.

	Day	Night
Number of profiles	90	182
D (m)	6.76	6.63
L (m)	2.23	-0.14
$\tau(N/m^2)$	0.03	0.003
$J_q^0(W/m^2)$	-504.92	162.45
$10^{-8}\ J_b^0(W/kg)$	-23.02	8.71
$\epsilon/\epsilon_*(obs)$	1.29	0.92
	$(0.81, 1.42)$	$(0.41, 1.38)$
$\epsilon/\epsilon_*(model)$	0.93	0.21
	$(0.57, 1.28)$	$(0.11, 0.33)$

CHAPTER V

SUMMARY AND CONCLUSIONS

Using a combined observational-modeling approach, this study has investigated small-scale turbulence processes in a complex, enclosed fresh water reservoir in VB, Mexico. Based on an extensive data set of temperature microstructure from four stations, estimates of turbulence parameters such as χ and ϵ were made. χ was calculated directly from the temperature microstructure data while ϵ was estimated by fitting a theoretical Batchelor spectrum to the raw data from SCAMP. We used the rejection criteria suggested by [26] and based on statistical analyses of parameters such as SNR, LR, and MAD we proposed our critical limits for these parameters to automate the fitting procedure. The critical limits for rejecting a fit were :

- SNR less than 5,
- MAD more than 1
- log_{10}(LR) less than 2

In addition, we did an analysis based on visual inspection to accept a particular fit and compared it to the automated analyses. With the above limits, we rejected $\sim 16\%$ of the fits compared to a rejection of $\sim 23\%$ based solely on visual inspection. TKED estimates from visual inspection were, eventually, used for all further data analyses.

From the meteorological data, it was concluded that winds blew mainly along the main axis of the reservoir. Winds gained intensity every morning but later afternoon there were almost no winds. This continous waxing and waning of wind strength over the length of the experiment period led to internal seiches of V1 vertical and H1 horizontal mode (see App.C). This has been manifested from our data set at stations 2 and 12, where seiche periods were 15 and 18 hours, respectively.

At all four stations, winds played a major role in driving surface layer mixing during daytime. At night, convection was the apparent driving force for surface layer mixing. Relatively intense BBL mixing was observed at station 5, which might result from internal wave breaking near the sloping bottom. A crude estimate of the bottom slope suggests that they were critical for breaking of internal waves. We also noticed BBL mixing at other stations, though it was not as intense as at station 5.

Computation of salinity was done using the fresh water equation of state, as suggested by [30]. Although salinity changes were relatively small, they showed a slightly fresher water lens trapped between saltier water at station 2. At this time we can only speculate that it might have originated from a fresh water input from precipitation which may have been mixed from the surface downwards.

The second part of this study focused on numerical model simulations of turbulence processes in the reservoir. For this purpose, we used a general one-dimensional ocean turbulence model, GOTM, with the "classic" two-equation k-ϵ model combined with the algebraic second moment closure as recently suggested by [64]. The model was forced by surface fluxes calculated from meteorological observations and also by an external pressure gradient at station 5. For the latter, near-bed velocity observations from an ADCP were used, following the method suggested by [57]. Temperature profiles were relaxed to the observations every hour in order to improve modeling of turbulence processes.

The questions posed for this study and the main results are discussed next.

- **How well do the model simulations compare to the observations and what are the model limitations ?**

  Concerning the agreement between observations and model results, it must be stated that the basic dynamics are qualitatively and quantitatively reproduced.

The most striking differences occur in the region of the thermocline and BBL where the numerical models could not resolve the complex dynamics of decaying turbulence. In contrast, the model does a fair job in reproducing turbulence in the surface layer both during day and night, however, during night, it slightly underestimated χ and ϵ values.

For simulating mixing processes in the BBL, we used the near-bottom current measurements from the ADCP at station 5. The model reproduced the relatively strong mixing events in the BBL during day and followed the same trend as that of the observations. However, the extent of mixing was limited to a few meters ($\sim$ 4m) above the bottom compared to $\sim$ 8m for the observations.

- **How do TKED, ϵ and χ relate to wind stress and bouyancy flux ?**

  For almost two decades, atmospheric scientists have parameterized turbulence in the atmospheric boundary layer (ABL) using similarity scaling. Based on similar principles, there have been subsequent developments in understanding the vertical structure in the oceanic boundary layer (OBL). The ABL develops vertically by the action of wind stress and heat flux at the surface. Using the same analogy, the OBL is also directly affected by wind stress and buoyancy flux at the surface [35]. In [68], it was shown that dissipation rates measured close to the surface of the OBL are inversely proportial to depth, z, as predicted by wind stress similarity scaling. [50] reported the first evidence for convective scaling using TKED profiles from two oceanic sites, and in [36], it was shown that the vertical structure of TKED in the convective boundary layer of a lake is remarkably similar to that found in the ABL. However, [36] argued that similarity scaling is valid in the mixed layer and should not be expected to work when $|z/D|$ exceeds unity, where D is the mixed layer depth.

In this study, during daytime, similarity scaling was applied only when winds were significant, while during night, it was applied to periods when buoyancy flux was relatively constant and positive [37]. During both day and night, ϵ values measured in the mixed layer were close to those predicted by the similarity scaling and followed the same trend. Measured χ did not correspond well to the structure predicted by similarity scaling. During night, measured χ values were almost an order of magnitude higher than those predicted by the similarity scaling. However, during daytime, measured values followed the similarity structure within $-1 < z/D < -0.5$.

- **What is the role of Bottom Boundary Layer (BBL) in the overall picture of mixing ?**

  With recent advances in field measurements, the importance of BBL mixing as a means of nutrient circulation in the hypolimnion of lakes has become increasingly evident (e.g. [69]; [70]; [71]). A number of processes initiate BBL mixing : bottom intrusions over rough topography, turbidity currents, internal wave breaking at the bottom; and river inflows. Some of these processes have been identified, but it has been suggested that breaking internal waves on slopes are the most likely driving mechanism for BBL mixing (e.g. [72]; [73]).

  Internal waves, noticed at stations 2 and 12, behave in a fashion similar to a suction pump - continously pumping fresh stratified fluid into the boundary layer, while simultaneously extracting the mixed boundary fluid. Breaking of internal waves at the sloping bottom results in strong mixing in the BBL which might extend into the interior stratified fluid. This eventually leads to redistribution of nutrients from the bottom back to the surface. Since BBL mixing was observed at almost all the four stations in VB, this might be a possible

mechanism recirculating nutrients into the water column and hence increasing the likelihood of advancing the reservoir towards a state of eutrophication.

REFERENCES

[1] J.N. Moum and W.D.Smyth, "Upper ocean mixing," in *Encycl. Oc. Sci.* Academic Press, Orlando, FL, 2000.

[2] A.N.Kolmogorov, "The local structure of turbulence in incompressible viscous fluid for very large reynolds number," *Dokl. Akad. Nauk SSSR*, vol. 30, pp. 301–305, 1941.

[3] G.K.Batchelor and A.A.Townsend, "The nature of turbulent motion at large wave-numbers," *Proc. Roy. Soc. A.*, vol. 199, pp. 238–255, 1949.

[4] A.M.Obukhov, "Some specific features of atmospheric turbulence," *J. Fluid Mech.*, vol. 13, pp. 77–81, 1962.

[5] A.Monin and A.Obukhov, "Basic laws of turbulent mixing in the atmosphere near the ground," *Dokl. Akad. Nauk SSSR Geofiz. Inst.*, vol. 151, pp. 163–187, 1954.

[6] H.L.Grant, R.W.Stewart, and A.Moilliet, "Turbulence spectra from a tidal chanel," *J. Fluid Mech.*, vol. 12, pp. 241–263, 1962.

[7] H.L.Grant, A.Moilliet, and W.M.Vogel, "Some observations of the occurence of turbulence in and above the thermocline," *J. Fluid Mech.*, vol. 34, pp. 443–498, 1968.

[8] M.C.Gregg and C.S.Cox, "Measurements of the oceanic microstructure of temperature and electrical conductivity," *Deep Sea Res.*, vol. 18, pp. 925–934, 1971.

[9] T.R.Osborn and C.S.Cox, "Oceanic finestructure," *Geophys. Fluid Dyn.*, vol. 3, pp. 321–345, 1972.

[10] T.R.Osborn and R.G.Lueck, "Turbulence measurements with a submarine," *J. Phys. Oceanogr.*, vol. 15, pp. 1502–1520, 1985.

[11] M.C.Gregg, "The study of mixing in the ocean : A brief history," *Oceanography*, vol. 4, pp. 39–45, 1991.

[12] J.Röttger and M.F.Larsen, "UHF/VHF techniques of atmospheric research and wind profiler application," in *Radar in Meteorology*, D.Atlas, Ed. Washington DC: American Meteorological Society, 1990, pp.235-281.

[13] E.B.Kraus, "Modelling and prediction of the upper layers of the ocean," *Pergamon, New York*, 1977.

[14] S.A.Orszag and G.S.Patterson, "Numerical simulation of turbulence," *Statistical Models and Turbulence, Lecture Notes in Physics*, vol. 12, 1972.

[15] J.Smagorinsky, "General circulation experiments with the primitive equations," *Monthly Weather Rev.*, vol. 91, pp. 99–120, 1963.

[16] J.W.Deardroff, "A numerical study of three-dimensional turbulent channel flow at large reynolds number," *J. Fluid Mech.*, vol. 41, pp. 453–480, 1970.

[17] G.L.Mellor and T. Yamada, "Development of a turbulence closure model for geophysical fluid problems," *Rev. Geophys. Space Phys.*, vol. 20, pp. 851–875, 1982.

[18] W.Rodi, "Examples of calculation methods for flow and mixing in stratified fluids," *J. Geophys. Res.*, vol. 92, pp. 5305–5328, 1987.

[19] H.Burchard and K.Bolding, "Comparative analysis of four second-moment turbulence closure models for the oceanic mixed layer," *J. Phys. Oceanogr.*, vol. 31, pp. 1943–1968, 2001.

[20] H.Baumert and H.Peters, "Second-moment closures and length scales for weakly stratified turbulent shear flows," *J. Geophys. Res.*, vol. 105, pp. 6453–6468, 2000.

[21] H. H.Burchard and H.Baumert, "On the performance of a mixed-layer model based on the k-ϵ turbulence closure," *J. Geophys. Res.*, vol. 100, pp. 8523–8540, 1995.

[22] H.Burchard, O.Petersen, and T.P.Rippeth, "Comparing the performance of the Mellor-Yamada and the k-ϵ two-equation turbulence models," *J. Geophys. Res.*, vol. 103, pp. 10543–10554, 1998.

[23] H.Burchard, K.Bolding, T.P.Rippeth, A.Stips, J.H.Simpson, and J.Sundermann, "Microstructure of turbulence in the northern North Sea: a comparative study of observations and model simulations," *J. Sea Res.*, vol. 47, pp. 223–238, 2001.

[24] A.Stips, H.Burchard, K.Bolding, and W.Eifler, "Modelling of convective turbulence with a two-equation k-ϵ turbulence closure scheme," *Ocean Dynamics*, vol. 52, pp. 153–168, 2002.

[25] H.Burchard and O.Petersen, "Models of turbulence in the marine environment - a comparative study of two-equation turbulence models," *J. Mar. Sys.*, vol. 21, pp. 29–53, 1998.

[26] B.Ruddick, A.Anis, and K.Thompson, "Maximum likelihood spectral fitting: The Batchelor spectrum," *J. Atmos. Ocean. Tech.*, vol. 17, pp. 1541–1555, 2000.

[27] G.K.Batchelor, "Small-scale variation of convected quantities like temperature in turbulent fluid. Part 1. General discussion and the case of small conductivity," *J. Fluid Mech.*, vol. 5, pp. 113–133, 1959.

[28] T.M.Dillon and D.R.Caldwell, "The Batchelor spectrum and dissipation in the upper ocean," *J. Geophys. Res.*, vol. 85, pp. 1910–1916, 1980.

[29] N.S.Oakey, "Determination of the rate of dissipation of turbulent energy from simultaneous temperature and velocity shear microstructure measurements," *J. Phys. Oceanogr.*, vol. 12, pp. 256–271, 1982.

[30] C.T.Chen and F.J.Millero, "Precise thermodynamic properties for natural waters covering only the limnological range," *Limnol. Oceanogr.*, vol. 31, no. 3, pp. 657–662, 1986.

[31] S.D.Smith, "Coefficients for sea surface wind stress, heat flux, and wind profiles as a function of wind speed and temperature," *J. Geophys. Res.*, vol. 93, pp. 15467–15472, 1988.

[32] C.W.Fairall, E.F.Bradley, D.P.Rogers, J.B.Edson, and G.S.Young, "Bulk parameterization of air-sea fluxes for Tropical Ocean-Global Atmosphere Coupled-Ocean Atmosphere Response Experiment," *J. Geophy. Res.*, vol. 101, pp. 3747–3764, 1996.

[33] C.W.Fairall, E.F.Bradley, J.E.Hare, A.A.Grachev, and J.B.Edson, "Bulk parameterization of air-sea fluxes: Updates and verification for the COARE algorithm," *J. Climate*, vol. 16, pp. 571–591, 2003.

[34] H.Burchard, "Applied turbulence modelling in marine waters," *Lect. Notes in Earth Sci.*, vol. 100, 2002.

[35] A.Anis and J.N.Moum, "The superadiabatic surface layer of the ocean during convection," *J. Phys. Oceanogr.*, vol. 22, pp. 1221–1227, 1992.

[36] J.Brubaker, "Similarity structure in the convective boundary layer of a lake," *Nature*, vol. 330, pp. 742–745, 1987.

[37] C.P.Lombardo and M.C.Gregg, "Similarity scaling of viscous and thermal dissipation in a convecting surface boundary layer," *J. Geophys. Res.*, vol. 94, pp. 6273–6284, 1989.

[38] D.R.Caldwell, "Small-scale physics of the ocean," *Rev. Geophys. Space Phys.*, vol. 21, pp. 1192–1205, 1983.

[39] T.R.Osborn, "Estimates of the local rate of vertical diffusion from dissipation measurements," *J. Phys. Oceanogr.*, vol. 10, pp. 83–89, 1980.

[40] W.H.Munk, "Abyssal recipes," *Deep Sea Res.*, vol. 13, pp. 707–730, 1966.

[41] H.L.Grant, B.A.Hughes, W.M.Vogel, and A.Moilliet, "The spectrum of temperature fluctuations in turbulent flow," *Fluid Mech.*, vol. 34, no. 3, pp. 423–442, 1968.

[42] C.H.Gibson, "Finestructure of scalar fields mixed by turbulence, 1, 2," *Phys. Fluids*, vol. 11, pp. 2305–2327, 1968.

[43] M.C.Gregg, "Variations in the intensity of small-scale mixing in the main thermocline," *J. Phys. Oceanogr.*, vol. 7, pp. 436–454, 1977.

[44] G.N.Ivey and J.Imberger, "On the nature of turbulence in a stratified fluid. Part I : The energetics of mixing," *J. Phys. Oceanogr.*, vol. 21, pp. 650–680, 1991.

[45] D.A.Luketina and J.Imberger, "Determining turbulent kinetic energy dissipation rate from Batchelor curve fitting," *J. Atmos. Oceanic Technol.*, vol. 18, pp. 100–113, 2001.

[46] J.A.Elliott and N.S.Oakey, "Spectrum of small-scale oceanic temperature gradients," *J. Fish. Res. Bd. Can.*, vol. 33, pp. 2296–2306, 1976.

[47] M.C.Gregg, "Finestructure and microstructure observations during the passage of a mild storm," *J. Phys. Oceanogr.*, vol. 6, pp. 528–555, 1976.

[48] G.O.Marmorino and D.R.Caldwell, "Temperature finestructure and microstructure observations in a coastal upwelling region during a period of variable winds (Oregon, summer 1974)," *Deep Sea Res.*, vol. 25, pp. 1073–1106, 1978.

[49] M.C.Gregg, E.A.D'Asaro, T.J.Shay, and N.Larson, "Observations of persistent mixing and near-inertial internal waves," *J. Phys. Oceanogr.*, vol. 16, pp. 856–885, 1986.

[50] T.J.Shay and M.C.Gregg, "Convectively driven turbulent mixing in the upper ocean," *J. Phys. Oceanogr.*, vol. 16, pp. 1777–1798, 1986.

[51] H.Yamazaki and R.Lueck, "Why oceanic dissipation rates are not lognormal," *J. Phys. Oceanogr.*, vol. 20, pp. 1907–1918, 1990.

[52] R.G.Lueck, "Turbulent mixing at the Pacific subtropical front," *J. Phys. Oceanogr.*, vol. 18, pp. 1761–1774, 1988.

[53] T.R.Osborn, "Measurements of energy dissipation adjacent to an island," *J. Geophs. Res.*, vol. 83, pp. 2939–2957, 1978.

[54] W.R.Crawford and R.K.Dewey, "Confidence limits for friction velocities determined from turbulence profiles in coastal waters," *J. Atmos. Oc. Technol.*, vol. 7, pp. 50–57, 1990.

[55] T.R.Osborn and R.G.Lueck, "Turbulence measurements from a towed body," *J. Atmos. Oc. Technol.*, vol. 2, pp. 517–527, 1985.

[56] J.N.Moum, D.R.Caldwell, and C.A.Paulson, "Mixing in the equatorial surface layer and thermocline," *J. Geophys. Res.*, vol. 94, no. C2, pp. 2005–2021, 1989.

[57] H.Burchard, "Recalculation of surface slopes as forcing for numerical water column models of tidal flow," *App. Math. Modelling*, vol. 23, pp. 737–755, 1999.

[58] R.E.Payne, "Albedo of the sea surface," *J. Atmos. Sci.*, vol. 29, pp. 959–970, 1972.

[59] I.Y.Fung, D.E.Harrison, and A.A.Lacis, "On the variability of the net longwave radiation at the ocean surface," *Rev. Geophys. Space Phys.*, vol. 22, pp. 177–193, 1984.

[60] R.H.Clarke, "Attempts to simulate the diurnal course of meteorological variables in the boundary layer," *Izvestiya - Akad. Nauk. SSSR*, vol. 10, no. 6, pp. 600–612, 1974.

[61] G.L.Mellor and T. Yamada, "A hierarchy of turbulence closure models for planetary boundary layers," *J. Atmos. Sci.*, vol. 31, pp. 1791–1806, 1974.

[62] K.Bolding, H.Burchard, T.Pohlmann, and A.Stips, "Turbulent mixing in the northern North Sea: A numerical model study," *Cont. Shelf Res.*, vol. 22, pp. 2707–2724, 2002.

[63] A.E.Gill, *Atmosphere-Ocean Dynamics*, Academic Press, Orlando, FL, 1982.

[64] V.M.Canuto, A.Howard, Y.Cheng, and M.S.Dubovikov, "Ocean turbulence I. One-point closure model. Momentum and heat vertical diffusivities," *J. Phys. Oceanogr.*, vol. 31, pp. 1413–1426, 2001.

[65] M.Munnich, A.Wuest, and D.M.Imboden, "Observations of the second vertical mode of the internal seiche in an Alpine Lake," *Limnol. Oceanogr.*, vol. 37, no. 8, pp. 1705–1719, 1992.

[66] H.Tennekes and J.L.Lumley, *A first course in turbulence*, MIT Press, Cambridge, MA, 1985.

[67] B.Efron and G.Gong, "A leisurely look at the bootstrap, the jacknife and cross-validation," *Amer. Statist.*, vol. 37, pp. 36–48, 1983.

[68] T.M.Dillon, J.G.Richman, C.G.Hansen, and M.D.Pearson, "Near-surface turbulence measurements in a lake," *Nature*, vol. 290, pp. 390–392, 1981.

[69] I.P.D.De Silva, J.Imberger, and G.N.Ivey, "Localized mixing due to a breaking internal wave ray at a sloping bed," *J. Fluid Mech.*, vol. 350, pp. 1–27, 1997.

[70] C.C.Eriksen, "Implications of ocean bottom reflection for internal wave spectra and mixing," *J. Phys. Oceanogr.*, vol. 15, no. 9, pp. 1145–1156, 1985.

[71] A.Wuest, D.C.Van Senden, J.Imberger, G.Piepke, and M.Gloor, "Diapycnal diffusivity measured by microstructure and tracer techniques - a comparison," in *Proc. Intl. Symp. on Stratified Flows*, Grenoble, France, 1994, vol. 3, pp. B5–8.

[72] C.Garrett, P.Maccready, and P.Rhines, "Boundary mixing and arrested Ekman layers : Rotating stratified flow near a sloping boundary," *Ann. Rev. Fluid Mech.*, vol. 25, pp. 291–323, 1993.

[73] G.N.Ivey and R.I.Nokes, "Vertical mixing due to the breaking of critical internal waves on sloping boundaries," *J. Fluid Mech.*, vol. 204, pp. 479–500, 1989.

[74] L.H.Miller, "Table of percentage points of Kolmogorov statistics," *J. Amer. Statist. Assoc*, vol. 51, pp. 111–121, 1956.

[75] F.Lampariello, "On the use of the Kolmogorov-Smirnov statistical test for immunofluorescence histogram comparison," *Cytometry*, vol. 39, pp. 179–188, 2000.

[76] T.Dauxois and W.R.Young, "Near-critical reflection of internal waves," *J. Fluid Mech.*, vol. 390, pp. 271–296, 1999.

[77] D.N.Slinn and J.J.Riley, "Turbulent mixing in the oceanic boundary layer caused by internal wave reflection from sloping terrain," *Dyn. of Atmos. and Oceans*, vol. 24, pp. 51–62, 1996.

APPENDIX A

DISSIPATION RATE ESTIMATES USING MACSCAMP

This appendix provides the description of χ and TKED (ϵ) estimates using a software - MacSCAMP, kindly provided to us by Dr. Sally MacIntyre from University of California at Santa Barbara. We will show comparisons of TKED estimates from all the stations using our software (AASCAMP) and MacSCAMP. The fitting parameters have been kept the same for both the softwares to maintain consistency in dissipation rate estimates. Table IX summarizes these parameters for both AASCAMP and MacSCAMP.

Table IX. Parameters for AASCAMP and MacSCAMP.

Parameter	AASCAMP	MacSCAMP
Segmentation	fixed	fixed
Segment Length	512	512
nfft	512	512
overlap	no	no
SNR limit	5	5
Velocity limit (m/s)	0.06	0.06

Figs. 38 , 39, 40, and 41 show plots of χ and ϵ estimates at stations 2, 8, 5, and 12 respectively using both AASCAMP and MacSCAMP. In general, a good agreement was found between the values of χ and ϵ estimated from AASCAMP and MacSCAMP. However, we can see that MacSCAMP estimates for χ and ϵ are slightly higher than those from AASCAMP near the thermoclinic region and in the BBL. To be on a safer side, estimates from AASCAMP are preferred simply because it is better

to underestimate rather than overestimating turbulence dissipation rates, especially near the thermocline which is a region of high intermittency.

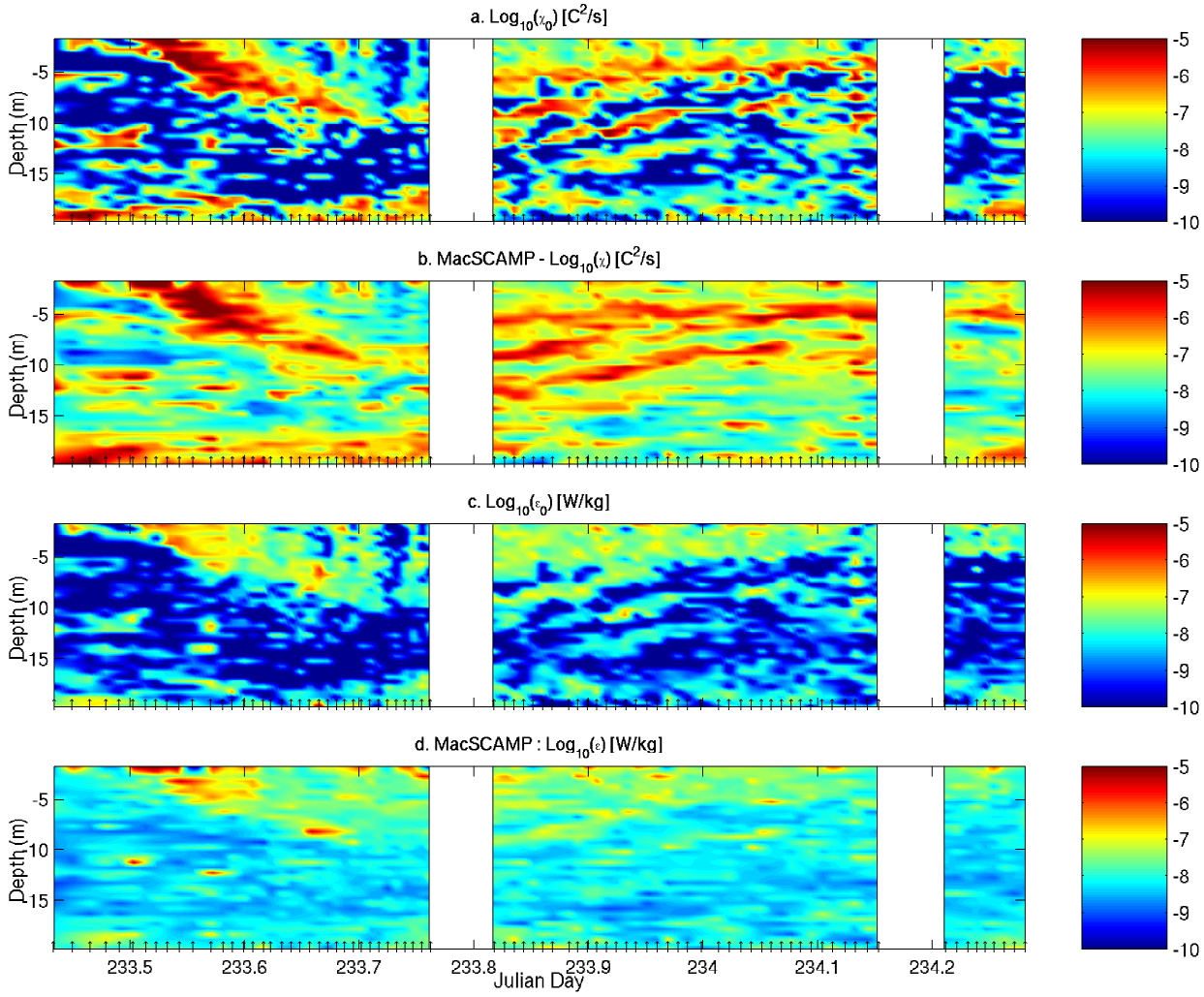

Fig. 38. Comparison of TKED estimates from AASCAMP and MacSCAMP at station 2; (a) χ from AASCAMP; (b) χ from MacSCAMP; (c) ϵ from AASCAMP; and (d) ϵ from MacSCAMP.

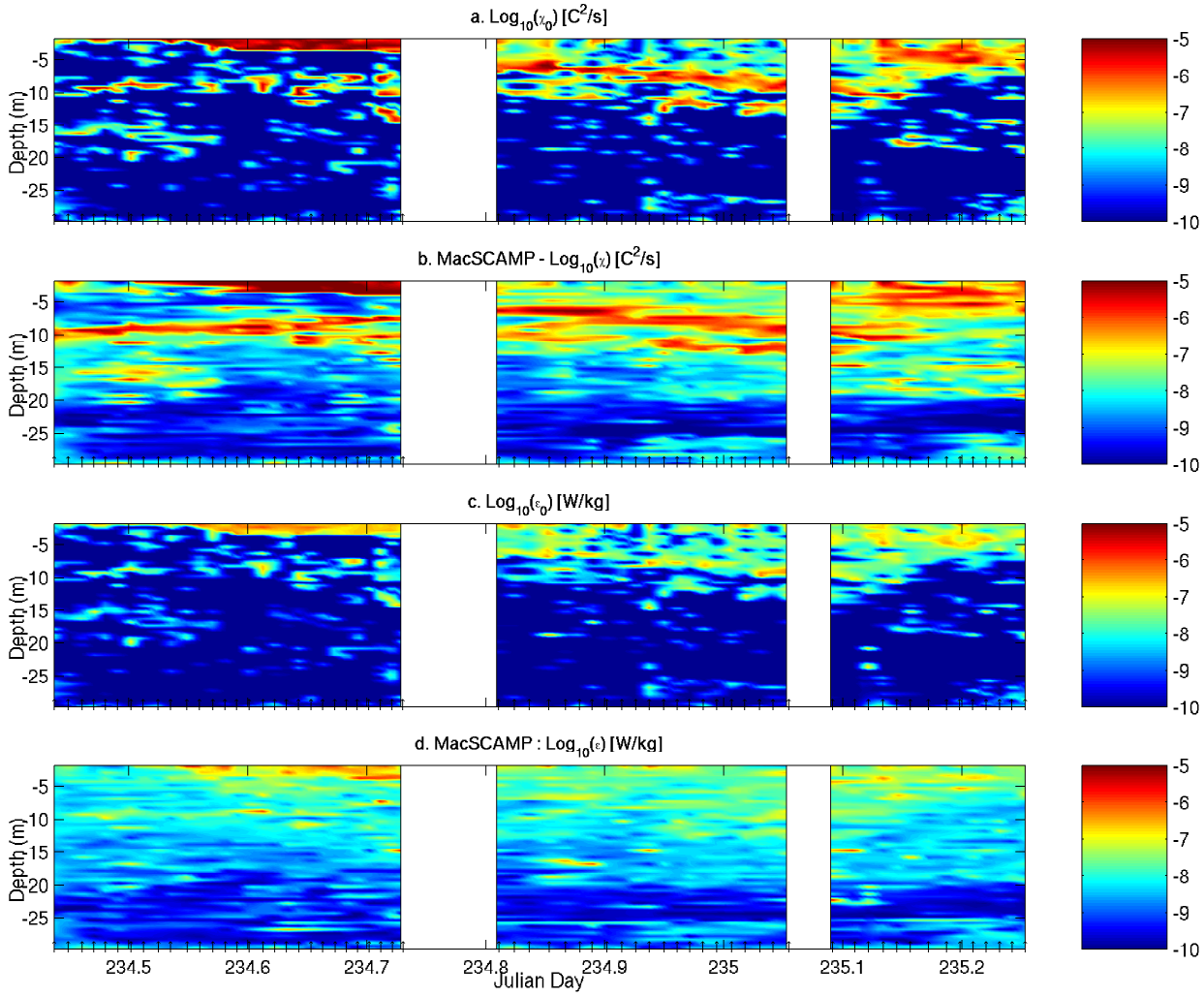

Fig. 39. Same as Fig. 38 but for station 8.

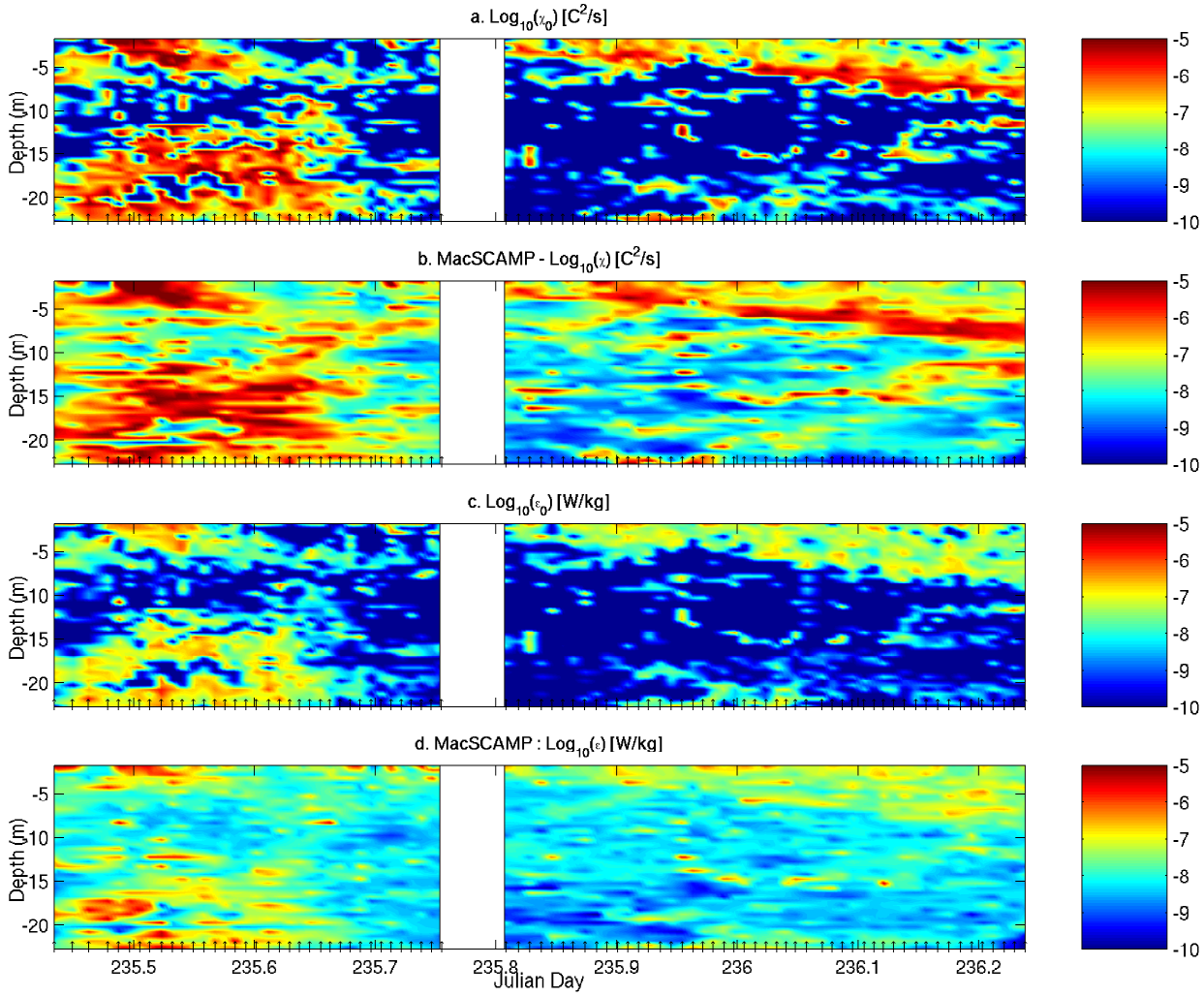

Fig. 40. Same as Fig. 38 but for station 5.

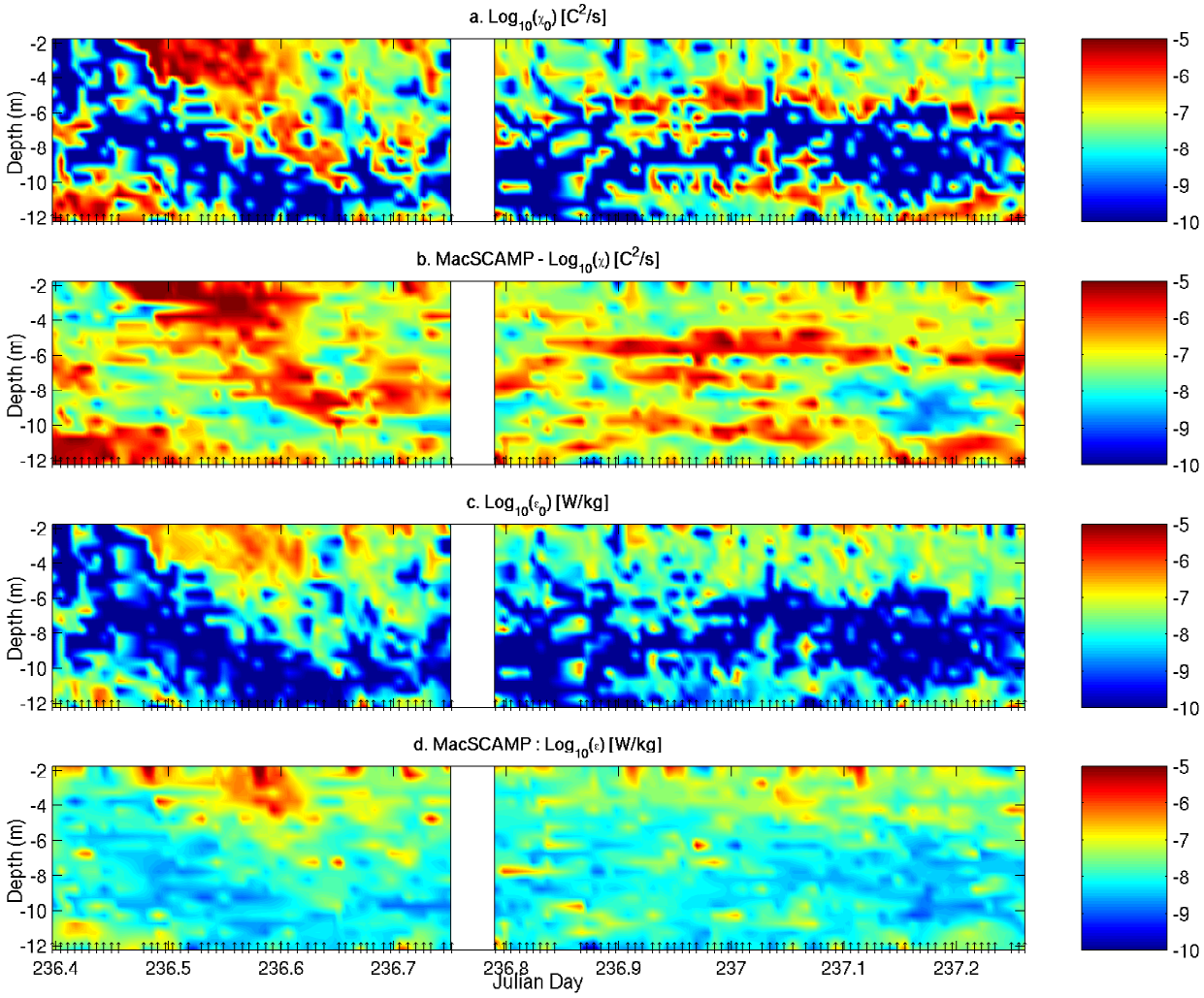

Fig. 41. Same as Fig. 38 but for station 12.

APPENDIX B

THE KOLMOGOROV SMIRNOV STATISTICAL TEST

Two-sample Kolmogorov Smirnov (KS2) test was performed for theoretical and empirical datasets of turbulence dissipation rates. It is a simple method comparing the empirical cumulative distribution function (cdf) with the theoretical cdf of a known distribution [74]. KS2 statistic measures the maximum distance, d_{max}, between the cdfs of theoretical and empirical data given by :

$$d_{max} = maximum(S_n(x) - F(x)) \tag{B.1}$$

where $S_n(x)$ is the empirical cdf and $F(x)$ is the theoretical cdf. For KS2 hypothesis to be accepted, d_{max} should be below the critical value, d_{crit}, for that dataset. If the null hypothesis is accepted, then the dataset follows the known distribution. If the sample size, N, is less than 100, then critical values can be obtained from statistical tables ([74], Table 1). If sample size is larger than 100, then the critical values of KS2 statistics can be calculated [75] from :

$$d_{crit} = c(\alpha)\sqrt{\frac{N_1 + N_2}{N_1 N_2}} \tag{B.2}$$

where N_1, N_2 are sample sizes of datasets ($S_n(x)$ and $F_n(x)$), α is the confidence level, and $c(\alpha)$ is defined in Table X [75].

Table X. Values of $c(\alpha)$ for different α levels.

α	0.1	0.05	0.025	0.01	0.005	0.001
$c(\alpha)$	1.22	1.36	1.48	1.63	1.73	1.95

APPENDIX C

INTERNAL WAVE DYNAMICS

This appendix highlights the main properties of internal wave dynamics in enclosed water bodies, such as VB, Mexico. Internal waves were observed at stations 2 and 12 (sections 3.D.1 and 3.D.4). Standing waves, so called seiches, can be distinguished into two types : a) Barotropic (surface); and b) Baroclinic (internal) [65]. Barotropic type generally have small vertical amplitudes (centimeters), large velocities and short periods (minutes to hours). In contrast, baroclinic seiches have large amplitudes (several meters), lower velocities and correspondingly longer periods (hours to days).

Internal wave dynamics are important for many physical processes in the water column. Part of the energy introduced at the surface by winds is transferred to internal seiches and can become available for mixing and redistribution of dissolved particles in the interior. Internal seiches also cause a periodic vertical displacement of suspended matter.

In the present study we are concerned in determining if internal waves existed during the time of sampling, and if so what were the internal wave modes. Next we describe the estimation of mode periods of an internal wave in enclosed lakes based on a three-layer seiche model suggested by [65] and follow with a discussion of bottom slopes critical for internal wave breaking.

Internal Wave Modes

The model equations given by [65] are summarized in the following discussion. The period $T_{n,m}$ (n represents vertical and m represents horizontal mode) of an internal wave is given by:

$$T_{n,m} = \frac{2L}{\sqrt{g\lambda_n^{1/2}}m} \tag{C.1}$$

where $n = 1, 2$; $m = 1, 2, 3...$; and L is the length of the lake in meters.

Eigen values, λ_n, for baroclinic modes are given as

$$\lambda_{1,2} = \frac{1}{2Z}(\gamma \pm [\gamma^2 - 4\alpha Z]^{1/2}) \tag{C.2}$$

where Z is the mean depth of the lake; α and γ are defined as

$$\gamma = \varepsilon_{12}z_1z_2 + \varepsilon_{23}z_2z_3 + \varepsilon_{13}z_1z_3, \quad \alpha = z_1z_2z_3\varepsilon_{12}\varepsilon_{23} \tag{C.3}$$

where z_1,z_2,z_3 are the depths of the epilimnion, metalimnion and hypolimnion, respectively, and ε_{jk} is the relative density difference between the layers, given as :

$$\varepsilon_{jk} = 1 - \frac{\rho_j}{\rho_k} \tag{C.4}$$

where ρ_j, ρ_k are the densities of the layers j and k, respectively in kg/m^3.

For VB, we assumed a three-layered structure with the length of the lake taken as the length along the main axis of the reservoir ($\sim$ 4000m). Average depths at stations 2 and 12 were $\sim$ 20 m and 15 m, respectively. Tables XI and XII summarize the estimation of mode periods at these stations.

Periods of V1H1 and V1H2 at station 2 are on the order of $\sim$ 15 hours (Table XI), close to the observed value of $\sim$ 15 hours (Fig. 19). Hence, the internal wave we noticed at station 2 might be a combination of V1H1 and V1H2 types.

Periods of V1H1 at station 12 are on the order of $\sim$ 20 hours (Table XII), which is close to our observations $\sim$ 18 hours (Fig. 25), suggesting a V1H1 mode for station 12 as well.

Table XI. Periods of the V1H1, V1H2 and V2H1 seiche modes calculated for station 2 using a simple three-layer model and three different cases for stratification. z is the layer thickness in m and ρ is the average density of the layer in kg/m^3. The length of the lake was set to 4000 m.

	Epilimnion		Metalimnion		Hypolimnion		Period (hours)		
	z	ρ	z	ρ	z	ρ	V1H1	V1H2	V2H1
1.	5	997.65	7	997.9	8	998.2	16.75	14.64	29.2
2.	9	997.65	5	997.9	6	998.2	15.9	15.7	31.4
3.	6	997.65	5	997.9	9	998.2	15.7	15.9	31.8

Table XII. Same as Table XI but for station 12.

	Epilimnion		Metalimnion		Hypolimnion		Period (hours)		
	z	ρ	z	ρ	z	ρ	V1H1	V1H2	V2H1
1.	6	997.65	2	997.8	4	998.2	19.3	26.5	52.9
2.	5	997.65	3	997.8	4	998.2	19.9	23.03	46.1
3.	4	997.65	4	997.8	4	998.2	20.4	21.7	43.4

Breaking Internal Waves on Sloping Bottoms

In lakes and estuaries, BBL mixing due to breaking internal waves at sloping beds may provide a significant contribution to the transport of matter through the benthic layer [40]. This redistribution of matter supplies the biological ecosystem with necessary nutrients, as the nutrient-rich bottom waters are mixed into the water column.

Recent field and laboratory experiments have suggested that the internal wave field can provide a sufficient source of energy to activate strong mixing near sloping boundaries and account for a significant portion of the overall oceanic vertical mixing (e.g. [69]; [70]; [76]; [77]). The angle of propagation of energy of an internal

wave depends on the wave frequency, ω, and the background density stratification. According to the dispersion relation, $\omega = Nsin\theta$, where N is the buoyancy frequency defined by $N^2 = (-g/\rho_0)(\partial\rho/\partial z)$, and θ is the angle between the group velocity vector and the horizontal. A critical condition for internal wave breaking is for the angle of propagation of the internal wave (θ) to be equal to the slope of the bed [69],

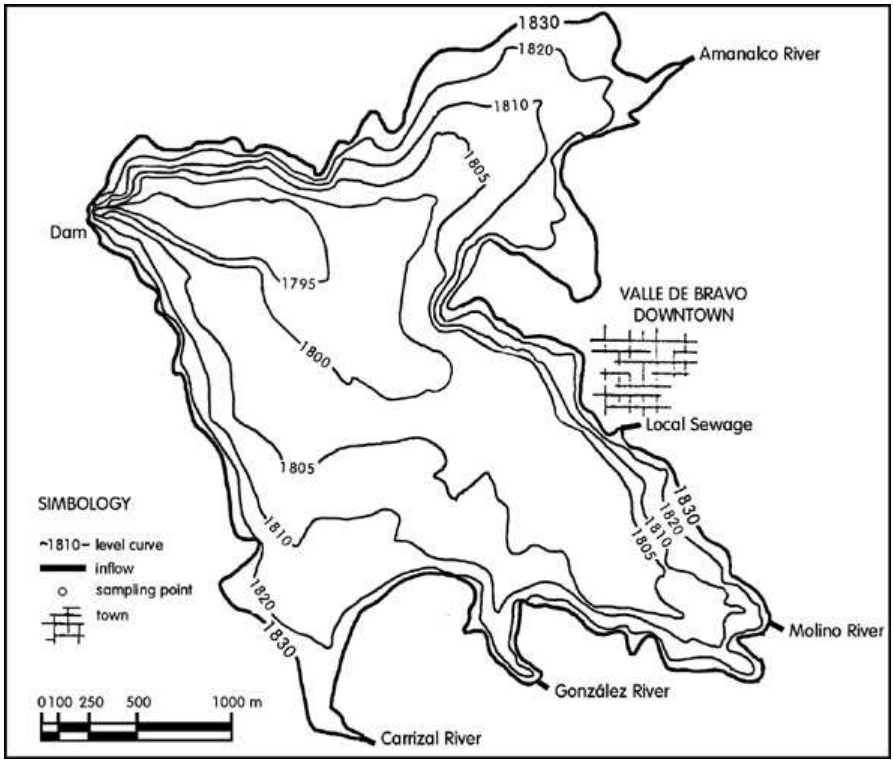

Fig. 42. Bathymertic chart of VB reservoir.

We used average density stratification, N, measured from microstructure data within the thermocline. θ values were estimated from the bathymetric chart (Fig.41). From N and θ, we estimated ω using the relation above and from the relation, $T = 2\pi/\omega$, we then estimated the periods of the internal wave.

Our computations yielded periods of $\sim$ 15 hours and $\sim$ 18 hours for stations 5 and 12, respectively (Table XIII). These results are in close proximity to those obtained from both the simple three-layer model and our observations, however, the procedure mentioned above should be considered only as a first approximation.

Table XIII. Periods of internal waves from bathymetric data. N is the buoyancy frequency; θ is the slope of the bed; and T is the mode period of an internal wave.

	Station 5	Station 12
N^2 $[rad/s^2]$	1x10^{-4}	1x10^{-5}
$sin\theta$	0.012	0.03
$Nsin\theta$	1.2x10^{-4}	9.5x10^{-5}
$T(= 2\pi/Nsin\theta)$ $[h]$	14.53	18.4

VITA

Gaurav Singhal was born in Jaipur, India in May, 1981. He received his baccalaureate degree in ocean engineering and naval architecture, with honors, from the Indian Institude of Technology, Kharagpur, India in July, 2003. After his master's degree, he will continue doctoral studies in oceanography at Texas A&M University.

He can be reached at the Department of Oceanography, Texas A&M University, College Station, TX 77843-3123

This document was typeset in LaTeX by Gaurav Singhal.